XFEM based Multiscale Approach for the Analysis of Masonry Walls

Khaled Abdelhalim

A Thesis

in

The Department

of

Building, Civil and Environmental Engineering

Presented in Partial Fulfillment of the Requirements

for the Degree of

Master of Applied Science (Civil Engineering) at

Concordia University

Montréal, Québec, Canada

March 2025

CONCORDIA UNIVERSITY

School of Graduate Studies

This is to certify that the thesis prepared

By: **Khaled Abdelhalim**

Entitled: **XFEM based Multiscale Approach for the Analysis of Masonry Walls**

and submitted in partial fulfillment of the requirements for the degree of

Master of Applied Science (Civil Engineering)

complies with the regulations of this University and meets the accepted standards with respect to originality and quality.

Signed by the Final Examining Committee:

_____ Chair
Dr. Khaled Galal

_____ Examiner
Dr. Khaled Galal

_____ Examiner
Dr. Biao Li

_____ Supervisor
Dr. Emre Erkmen

Approved by _____
S. Samuel Li, Chair
Department of Building, Civil and Environmental Engineering

_____ 2025

_____
MOURAD DEBBABI, Dean
Faculty of Engineering and Computer Science

Abstract

XFEM based Multiscale Approach for the Analysis of Masonry Walls

Khaled Abdelhalim

The increasing global emphasis on sustainable development has underscored the importance of understanding the mechanical behaviour of masonry materials in the context of modern construction practices. This thesis presents an X-FEM-based computational homogenization framework tailored for analysing heterogeneous masonry structures. The methodology leverages the advantages of the eXtended Finite Element Method (X-FEM) in introducing phased changes and capture interface behaviour within the representative volume element (RVEs) to represent the material behaviour of masonry structures.

The proposed framework introduces techniques for calculating effective material properties, incorporating periodicity of the masonry wall structure, and addressing interface damage effects. A detailed derivation of the governing equations is presented, along with rigorous validation against benchmark studies and experimental results from the literature. The analysis encompasses multiple case studies, including parametric studies on RVE size, assumed boundary condition effects, and the impact of interface damage on homogenized properties. Results reveal the accuracy and robustness of the X-FEM based approach in capturing the homogenized behaviour masonry walls.

This study not only bridges gaps in existing computational techniques but also provides insights into optimizing modelling strategies for masonry homogenization. The developed framework holds significant potential for applications in structural analysis and the sustainable design of masonry structures, offering a reliable tool for engineers and researchers in the field of computational mechanics.

Acknowledgments

I would like to express my deepest gratitude to my supervisor, Dr. Emre Erkmen, for his invaluable guidance, patience, and continuous support throughout this research. His expertise and insightful feedback have been instrumental in shaping this work, and I am sincerely grateful for the opportunity to learn under his supervision.

I extend my appreciation to my committee members, Dr. Khaled Galal and Dr. Biao Li, for their time, constructive feedback, and valuable contributions to my research. Their insights have greatly enriched the quality of this work.

A special thanks to my mother, Esmat Haikal, whose unwavering support and care have been my greatest source of strength throughout this journey. I am also profoundly grateful to my father, Attia Abdelhalim, whose encouragement and belief in me have been a constant motivation. Lastly, my deepest appreciation goes to my little brother, Youssef Abdelhalim, whose kindness and support have meant more to me than words can express.

This thesis is dedicated to them, with heartfelt gratitude.

Contents

List of Figures

List of Tables

Chapter 1

Introduction

1.1 Background and Motivation

Masonry structures have been an integral part of human civilization for thousands of years, serving as fundamental components in buildings, bridges, and monuments. From the ancient pyramids of Egypt to modern urban architecture, masonry's enduring presence highlights its significance in construction. This widespread use is attributed to masonry's durability, aesthetic appeal, and the abundance of raw materials like stone, brick, and mortar. As societies continue to rely on masonry for both historical preservation and new construction, understanding its mechanical behaviour becomes increasingly important.

Despite its long-standing prominence, masonry remains a complex material to analyse due to its heterogeneous composition. Unlike monolithic materials, masonry consists of discrete units (bricks or stones) bonded together by mortar joints. This composite nature introduces variability in material properties and creates discontinuities at the interfaces between units and mortar. These discontinuities can significantly influence the structural performance of masonry, particularly under mechanical loading conditions. Accurately predicting the behaviour of masonry structures is essential for ensuring their safety, longevity, and resilience.

Advancements in computational mechanics have provided powerful tools for simulating and analysing complex materials such as masonry. The Finite Element Method (FEM), in particular, has

been widely adopted for structural analysis due to its versatility and robustness. FEM allows engineers to model structures at various scales, providing insights into stress distributions, deformation patterns, and potential failure mechanisms. However, traditional FEM approaches face challenges when applied to masonry structures, as the inherent discontinuities and heterogeneities in masonry require highly refined meshes to capture the local interactions accurately, leading to increased computational costs and complexity.

In response to these challenges, researchers have explored enhanced computational methods that can more effectively model discontinuities without the need for excessive mesh refinement. The Extended Finite Element Method (XFEM) has emerged as a promising technique in this regard. XFEM extends the capabilities of FEM by incorporating enrichment functions that represent discontinuities such as cracks and material interfaces within the elements themselves. This allows for the modelling of complex behaviours without altering the underlying mesh, improving computational efficiency while maintaining accuracy.

Furthermore, computational homogenization techniques offer a means to bridge the gap between the micro-level behaviour of individual masonry components and the macro-level structural response. By averaging the mechanical properties over a representative volume element (RVE), homogenization provides effective material properties that account for the heterogeneity of masonry. Combining XFEM with computational homogenization presents an opportunity to develop a robust framework for analysing masonry structures, capturing both the local discontinuities and the global structural behaviour.

Recent advancements have extended these approaches to nonlinear analysis, which is crucial for understanding the mechanical response of masonry under higher loads and progressive damage. A nonlinear computational framework enables the accurate modelling of traction-separation laws at interfaces, the evolution of stress and traction fields, and the iterative solution of equilibrium equations. This capability significantly enhances the predictive power of computational models, facilitating more reliable assessments of masonry structures under complex loading conditions.

1.2 Problem Statement

Despite the potential of XFEM and computational homogenization, their application to masonry structures remains limited. Traditional modelling approaches either oversimplify the material by treating it as homogeneous or become computationally impractical when attempting to model every discontinuity explicitly. The lack of a comprehensive framework that integrates XFEM with homogenization techniques for masonry analysis leads to gaps in accurately predicting structural responses, particularly in both linear and nonlinear regimes.

Masonry structures are susceptible to stress concentrations and crack formations due to their discontinuous nature. These phenomena are critical in the early stages of loading and evolve further under increased stress, affecting the structural integrity over time. Existing methods struggle to capture the initiation and propagation of cracks within masonry without resorting to fine meshes or complex remeshing algorithms. Moreover, the absence of robust iterative solution procedures for nonlinear problems limits the ability to simulate damage evolution, cohesive interactions, and progressive failure mechanisms.

Therefore, there is a need for a computational framework that can effectively model the mechanical behaviour of masonry structures by accounting for their heterogeneous composition and discontinuities. Such a framework should leverage the strengths of XFEM in handling discontinuities, employ homogenization techniques to represent the effective material properties at the macro scale, and incorporate nonlinear solution strategies to capture the progressive response of masonry under complex loading conditions. Addressing this need will enhance the predictive capabilities of computational models for masonry structures, leading to better-informed engineering decisions.

1.3 Research Objectives

The primary objective of this thesis is to develop a computational homogenization framework based on the Extended Finite Element Method (XFEM) for the analysis of masonry structures within both the linear elastic and nonlinear regimes. The specific goals are:

- **To formulate a theoretical framework** that integrates XFEM with computational homogenization techniques to model the mechanical behaviour of masonry structures, capturing both the micro-level discontinuities and macro-level responses.
- **To implement the framework numerically**, developing algorithms and computational procedures that efficiently handle discontinuities without the need for remeshing or excessive mesh refinement.
- **To extend the framework to nonlinear analysis**, incorporating iterative solution methods such as the Newton-Raphson procedure, traction-separation laws, and cohesive interaction models to simulate the progressive response of masonry structures.
- **To validate the framework** through numerical experiments and comparisons with existing analytical solutions and traditional FEM models, assessing its accuracy and computational efficiency.
- **To analyse the influence of microstructural features** on the effective material properties of masonry, investigating how variations in brick and mortar configurations affect the overall structural response.

1.4 Scope of the Study

This thesis focuses on both the linear elastic and nonlinear analysis of masonry structures, emphasizing the response under mechanical loading conditions. The scope is defined as follows:

- **Linear and Nonlinear Regimes**: The study extends beyond the linear elastic assumption to incorporate nonlinear traction-separation laws, residual update procedures, and iterative correction techniques.
- **Two-Dimensional modelling**: The analysis is conducted in a two-dimensional context, which is appropriate for masonry wall structural components where one dimension is significantly smaller than the others, or where plane stress conditions apply.

- **Representative Volume Elements (RVEs)**: The microstructural analysis utilizes RVEs to capture the heterogeneity of masonry. The size and configuration of RVEs are selected to be representative of the overall material behaviour.

- **Computational Implementation**: The numerical implementation is developed within the framework of XFEM, focusing on the integration with homogenization and nonlinear solution techniques.

- **Validation**: The framework is validated through comparisons with alternative modelling approaches, analytical solutions and existing results from literature. Experimental validation is beyond the scope of this thesis but is acknowledged as an important aspect for future research.

1.5 Significance of the Study

The development of an XFEM-based computational homogenization framework for masonry structures offers several significant contributions:

- **Enhanced modelling Accuracy**: By accurately capturing the discontinuities inherent in masonry, the framework improves the precision of simulations, leading to better predictions of structural behaviour under various loading conditions.

- **Computational Efficiency**: The use of XFEM eliminates the need for mesh refinement around discontinuities, reducing computational resources and time required for simulations. This efficiency is crucial for practical engineering applications and large-scale analyses.

- **Insight into Micro-Macro Relationships**: The homogenization approach provides a deeper understanding of how microstructural features influence the macro-level properties of masonry. This insight can inform material selection, design strategies, and preservation techniques.

- **Contribution to Structural Engineering Practices**: The findings and methodologies presented in this thesis have the potential to enhance structural assessment and design practices for masonry structures, contributing to safer and more reliable constructions.

1.6 Thesis Outline

The thesis is organized into six sections, each building upon the previous to develop and validate the proposed computational framework.

- **Chapter 1: Introduction** provides an overview of the research background, identifies the problem, outlines the research objectives, defines the scope, and highlights the significance of the study.

- **Chapter 2: Literature Review** surveys existing research on masonry modelling, the Finite Element Method, the Extended Finite Element Method, and computational homogenization techniques, including nonlinear approaches. The chapter identifies gaps in the current knowledge and positions the thesis within the broader context of structural engineering research.

- **Chapter 3: Theoretical Framework and Numerical Implementation** presents the mathematical formulations underlying the XFEM and homogenization methods. It details the derivation of governing equations, the treatment of discontinuities, and the principles of scale separation essential for homogenization. It discusses the practical aspects of implementing the theoretical framework. It covers the discretization strategies, interpolation functions, enrichment schemes for XFEM, and the handling of boundary conditions in the context of RVEs, including the developed nonlinear iterative solution procedures and traction-separation models.

- **Chapter 4: Results and Validation** showcases the application of the developed framework to various numerical examples. The results are analysed and compared with analytical solutions and traditional FEM models to validate the accuracy and efficiency of the approach.

- **Chapter 5: Conclusions and Future Work** summarizes the key findings, reflects on the implications of the research, and suggests directions for future studies, including potential extensions to nonlinear analysis and experimental validation.

Chapter 2

Literature Review

Masonry, as a composite material consisting of bricks bonded by mortar, exhibits complex mechanical behaviour due to its heterogeneous nature. The response of masonry structures is inherently governed by the properties of these components and the interactions at their interfaces. Over the years, various methodologies have been proposed to model and predict the mechanical properties of masonry, both at the material and structural levels. The evolution of these methodologies reflects the ongoing effort to achieve greater accuracy in the analysis and design of masonry structures.

As research on masonry modelling evolved, homogenization techniques emerged as a practical approach to representing its mechanical behaviour at the structural level. These methods approximate masonry's elastic response by treating it as a continuum, enabling efficient structural analysis while preserving essential material characteristics. Calderini et al. [1], Beyer and Mangalathu [2], and Messali et al. [3] introduced equivalent material formulations that estimate masonry's overall stiffness and strength based on experimental calibration. While these approaches facilitated engineering applications, they relied on idealized assumptions that simplified the inherent heterogeneities of masonry. In seismic design, masonry walls are frequently modelled as shear walls, where flexural failure mechanisms are preferable for ensuring ductility and mitigating damage under lateral loading [4]. The refinement of homogenization models remains a central focus in masonry research, as the accuracy of these models directly impacts the reliability of seismic performance assessments and structural safety evaluations.

The initial attempts to model masonry's mechanical behaviour focused on simplifying assumptions to make the problem more tractable. Pande et al. [5] introduced an equivalent elastic modulus for brick masonry by modelling the material as a system of parallel layers. This method was among the earliest to provide a practical approach for estimating masonry's mechanical properties. However, it relied heavily on the assumption of perfect bonding between the brick and mortar, which oversimplified the complex interactions that actually occur within masonry structures.

As homogenization techniques advanced, researchers sought to enhance the accuracy of equivalent formulations by incorporating more detailed representations of masonry's heterogeneous structure. Briccoli Bati et al. [6] introduced a micromechanical approach by applying Eshelby's analytical solution for elliptical inclusions to derive homogenized elastic properties, offering a more rigorous perspective on material behaviour. This approach provided greater accuracy than earlier models, particularly in capturing the geometric aspects of masonry constituents. However, it relied on the assumption of perfect bonding between the components, which limited its ability to model debonding and other interface-related failures. Around the same time, Anthoine [7] developed periodic homogenization principles, leveraging the concept of a repeating unit cell to estimate effective stiffness, while Pietruszczak and Niu [8] proposed a three-dimensional averaging approach to improve the prediction of macroscopic properties by incorporating geometric and material variations. More recently, Drougkas et al. [9] extended Eshelby's solution to assess the mechanical response of damaged masonry, validating its effectiveness through experimental comparisons. The progression of these studies illustrates the shift from early simplified models to more advanced formulations capable of capturing masonry's anisotropic and damage-dependent behaviour, reflecting the ongoing effort to achieve greater accuracy in computational modelling.

Luciano and Sacco [10] advanced the field by incorporating damage mechanics into the homogenization framework. Their work allowed for the evaluation of the mechanical properties of damaged masonry, marking a significant step forward in capturing the degradation effects within masonry materials. Despite this progress, the model struggled to accurately represent the discontinuities and weak interfaces that are characteristic of masonry, particularly under conditions that lead to cracking.

As researchers sought to improve the realism of these models, Guedes and Kikuchi [11] introduced adaptive finite element methods (AFEM). Their approach allowed for mesh refinement based on error estimates, which enhanced the accuracy of simulations for complex microstructures like those found in masonry. However, this method also highlighted the significant computational challenges associated with such detailed modelling, particularly when dealing with discontinuities like cracks, which required complex remeshing strategies.

Fish and Wagiman [12] further extended the capabilities of finite element modelling by developing a multiscale finite element method (MSFEM) capable of analysing nonperiodic microstructures. This was particularly relevant for masonry, where the arrangement of bricks and mortar does not always follow a regular pattern. Their method expanded the mathematical homogenization theory to accommodate nonperiodic structures, though it still faced difficulties in accurately modelling the discontinuities that are prevalent in masonry, such as cracks and voids.

The limitations of traditional finite element methods in handling discontinuities were further addressed by Melenk and Babuška [13], who introduced the Partition of Unity Finite Element Method (PUFEM). This method was designed to address problems with rough or highly oscillatory solutions, where classical polynomial-based FEM failed unless the mesh size was very small or the polynomial degree was very high. PUFEM allowed for the inclusion of local behaviour into the global approximation space, thereby improving the robustness of simulations. However, the difficulty in efficiently integrating shape functions against each other complicated the construction of the stiffness matrix, which remained a challenge in its practical implementation.

To address mesh dependency issues in fracture modelling, researchers introduced Cohesive Zone Models (CZM) as a viable alternative, providing a more localized approach to crack evolution. These models localize softening effects within an interface region, where damage progression is governed by traction-separation laws rather than distributed strain softening. Potential-based cohesive models [14]–[18] introduced a thermodynamically consistent framework, deriving interface tractions from an energy potential to ensure robust predictions under mixed-mode loading. In contrast, plasticity-based cohesive models [19]–[22] incorporated yield or interaction surfaces to regulate softening, providing greater control over failure evolution. These formulations have been widely implemented in masonry modelling, offering a more accurate representation of progressive

bond degradation and interface cohesion loss under mechanical loading. However, CZM approaches typically require predefined crack paths or cohesive interfaces, limiting their adaptability in cases where cracks develop in arbitrary directions. To overcome this limitation, the Extended Finite Element Method (X-FEM) was introduced, allowing discontinuities to be incorporated independently of the finite element mesh, thereby enhancing computational efficiency and flexibility in fracture modelling.

In the next phase of development, Belytschko and Black [23] introduced the Extended Finite Element Method (X-FEM) to overcome the limitations of traditional FEM in handling discontinuities such as cracks. The X-FEM method enriched the solution space with discontinuous functions, allowing for the modelling of cracks and inclusions without requiring remeshing. This approach was particularly beneficial for masonry structures, where the presence of cracks and heterogeneous materials significantly affects mechanical behaviour. The motivation behind X-FEM was to address the computational challenges posed by remeshing in traditional FEM, although issues with numerical integration near discontinuities persisted.

Following the introduction of X-FEM by Belytschko and Black [23], significant advancements were made to enhance the method's applicability and accuracy, particularly for complex materials like masonry. Moës et al. [24] extended the X-FEM framework to handle crack growth without the need for remeshing. This was a critical development for dynamic scenarios typical in masonry structures, where cracks can propagate in unpredictable patterns. While this method addressed some geometric challenges, issues related to numerical stability and mesh refinement remained, particularly in cases involving complex crack paths.

Building on this, Sukumar et al. [25] integrated level set methods into X-FEM, which allowed for the accurate modelling of internal boundaries such as holes and inclusions within materials. This was particularly relevant for masonry, where voids and inclusions can significantly influence mechanical behaviour. The level set method provided a robust numerical technique for tracking interfaces and shapes, making it a powerful tool for representing the internal complexities of masonry. However, the method's high computational demands limited its practicality for large-scale applications, especially in engineering contexts where computational efficiency is paramount.

Miehe and Koch [26] proposed a computational micro-to-macro transition method, which was

essential for linking detailed microstructural characteristics to macroscopic behaviour. This approach provided a means to predict the overall mechanical properties of materials like masonry, which are influenced by their heterogeneous microstructures. The method focused on deriving macroscopic stress-strain responses from microstructural analyses, ensuring that the influence of microstructural heterogeneities was accurately captured. While homogenization techniques provide efficient estimates of effective material properties, they inherently assume a continuous medium, making them inadequate for capturing localized failure mechanisms such as interface debonding and crack propagation. This limitation is particularly significant in masonry, where weak mortar joints and interfacial discontinuities dictate structural behaviour. To address these challenges, advanced numerical techniques such as the Extended Finite Element Method (X-FEM) have been developed, offering an enriched formulation capable of incorporating discontinuities independently of the mesh.

Stroeven et al. [27] addressed the challenge of determining the appropriate size for Representative Volume Elements (RVEs) in heterogeneous materials. They introduced a statistical approach to quantify RVE size, ensuring that the simulations reflected the material's behaviour on a larger scale. This was particularly important for masonry, where material properties can vary significantly due to its heterogeneous nature. The method relied on generating various random particle distributions and conducting finite element simulations to evaluate how material properties varied with changes in particle configuration. Despite its effectiveness, handling complex geometries and material heterogeneities remained a challenge, particularly in accurately capturing localized phenomena such as stress concentrations and crack propagation.

In an effort to improve the micro-macro modelling of heterogeneous materials, Kouznetsova et al. [28] introduced a strategy that derived macroscopic behaviour from detailed microstructural modelling without relying on predefined constitutive models. This method was particularly effective for materials undergoing large deformations and exhibiting history-dependent material behaviour, such as masonry. By coupling micro-level (RVE) analysis with macro-level (structural) analysis, this approach ensured that the influence of microstructural heterogeneities was accurately accounted for in the overall structural response. However, simplifying the analysis to two-dimensional RVEs

sometimes led to inaccuracies for materials with complex three-dimensional microstructures, a limitation that needed to be addressed in further developments.

The work of Fernandes et al. [29] used the boundary element method (BEM) to model phase debonding and interface behaviours in heterogeneous materials. This approach was highly relevant to masonry, where phase interactions between bricks and mortar significantly influence mechanical behaviour. The BEM formulation efficiently handled the computational cost and complexity associated with analysing phase debonding, particularly in large-scale problems. However, BEM can be computationally intensive and may not fully capture discontinuities without mesh modifications, indicating a need for more efficient methods like X-FEM to address these challenges.

Zhou et al. [30] explored the impact of crack density and connectivity on the permeability of microcracked solids, modelling cracks as isolated or connected inclusions. Their work was critical in understanding the durability and serviceability of materials like masonry, where crack networks significantly affect permeability. The study extended the Interaction Direct Derivative (IDD) method to account for cracks with finite connectivity, recognizing that cracks in real materials are not isolated but tend to cluster and interconnect. While this method provided valuable insights into how crack connectivity impacts material properties, it may not fully capture the complexities of real-world crack networks, which are often more intricate than the simplified models used in the study.

As the development of numerical methods continued, researchers began to address specific challenges in the modelling of masonry structures, particularly those related to the accurate representation of complex geometries and material interfaces. The Extended Finite Element Method (X-FEM) played a crucial role in these advancements, offering a framework that could handle discontinuities more effectively than traditional finite element methods.

One significant contribution to the advancement of X-FEM was made by Zi and Belytschko [31], who introduced new crack-tip elements specifically designed to model cohesive cracks. This development allowed for the simulation of arbitrary crack paths, including complex geometries such as curved and intersecting cracks, which are common in masonry structures. By enriching the finite element space with special functions, their method provided a robust framework for accurately simulating crack growth without the need for remeshing. However, the method was primarily focused on homogeneous materials and did not fully address the multi-scale nature of materials like

masonry, where different phases interact at various scales.

Song et al. [32] further extended the capabilities of X-FEM by developing a method for dynamic crack and shear band propagation using phantom nodes. This approach allowed for the representation of discontinuities within elements without requiring mesh alignment, reducing computational costs and improving accuracy in dynamic simulations. The phantom node method was particularly useful for modelling cracks and shear bands in dynamic environments, which are relevant to masonry structures subjected to seismic loading. However, the method's assumptions of material homogeneity limited its applicability to heterogeneous materials like masonry, where the interaction between different phases is critical.

Laborde et al. [33] introduced a high-order X-FEM that incorporated polynomial basis functions and tailored enrichment functions to improve the accuracy of simulations in cracked domains. Their method addressed some of the convergence issues observed in earlier X-FEM approaches, particularly near crack tips where singularities can lead to suboptimal convergence rates. By enriching the finite element space with higher-order polynomial functions, their method provided a more accurate representation of displacement fields around crack tips. Despite these advancements, the method still faced challenges in handling complex microstructures like those found in masonry, particularly in maintaining accuracy and computational efficiency in large-scale problems.

Moës et al. [34] tackled the challenge of handling complex microstructure geometries by decoupling the mesh from the physical geometry of the problem. Their approach used level set functions to represent material interfaces, allowing for the accurate modelling of non-conforming meshes, which are often necessary in masonry structures. This method significantly reduced the computational burden associated with meshing complex geometries, making it more feasible to analyse masonry structures with intricate internal boundaries. However, while the method improved the handling of complex geometries, issues related to mesh conformity and convergence rates remained, particularly in non-conforming meshes.

As researchers sought to overcome the limitations of rigid interface assumptions, three-phase modelling approaches emerged to explicitly capture the interactions between bricks, mortar, and

their interfaces. These models introduced zero-thickness interface elements, enabling the simulation of bond degradation and progressive cracking under mechanical loading [35]–[39]. By incorporating an independent interface phase, these approaches offered a more refined representation of masonry's nonlinear response, particularly in modelling failure mechanisms driven by interface debonding. However, their accuracy came at the cost of increased computational demand, as fine discretization within mortar joints was often required to ensure numerical stability. A detailed review by D'Altri et al. [40] provides a comprehensive assessment of three-phase modelling strategies, discussing the balance between predictive accuracy and computational efficiency in masonry analysis.

The need for accurate modelling of crack propagation in materials with frictional forces was addressed by Liu and Borja [41], who introduced a robust contact algorithm within the X-FEM framework. Their method incorporated special enrichment functions to simulate discontinuities such as cracks within the material, allowing for the decoupling of crack growth from the underlying mesh. This approach was particularly advantageous for simulating frictional cracks in materials like masonry, where internal discontinuities significantly influence mechanical behaviour. The method proved useful in accurately modelling contact mechanics, but its focus on homogeneous materials limited its application to more complex, heterogeneous structures like masonry.

Fries and Baydoun [42] introduced a hybrid explicit-implicit crack description method within X-FEM, which combined the geometric accuracy of explicit crack descriptions with the computational efficiency of implicit methods. This approach was designed to handle complex crack geometries, making it particularly relevant for masonry structures with arbitrary crack growth directions. While the hybrid method offered a robust solution for crack propagation in brittle materials, it did not incorporate the multi-scale nature of masonry, where interactions between different phases must be accurately modelled to predict the material's overall behaviour.

Chessa et al. [43] made significant advancements in the construction of blending elements within the Partition of Unity Finite Element Method (PUFEM), which was essential for ensuring smooth transitions between enriched and unenriched regions in finite element meshes. Their method addressed the errors and convergence issues that often arose in traditional blending elements, particularly in regions where the mesh transitioned between different levels of enrichment. By proposing

an enhanced strain formulation based on the Hu-Washizu variational principle, they improved the accuracy and convergence of enriched finite element solutions. However, their approach was general and not specifically tailored to the unique challenges posed by heterogeneous materials like masonry, where phase interactions play a critical role in determining overall behaviour.

As the modelling of masonry structures continued to evolve, attention shifted towards improving the accuracy and efficiency of computational methods, particularly for materials with complex microstructures like masonry. The developments in X-FEM and related techniques were instrumental in addressing the challenges posed by the heterogeneity and discontinuities inherent in masonry.

One of the key challenges in the homogenization of masonry was accurately determining the Representative Volume Element (RVE) size, which is crucial for capturing the material's effective properties. Kanit et al. [44] conducted a study to establish a method for determining the appropriate RVE size for random heterogeneous materials. Their approach combined statistical analysis with numerical simulations to estimate the effective properties of materials like masonry, where variability in microstructure can significantly influence overall behaviour. This study was particularly relevant to computational homogenization, as it provided a framework for ensuring that the selected RVE is representative of the material's macroscopic properties. However, their methodology faced challenges in fully capturing the anisotropic behaviour typical of masonry structures.

Geers et al. [45] advanced the field of computational homogenization by developing methods that incorporated higher-order terms to account for microstructural characteristics in the macroscopic response. Their work was particularly relevant to the analysis of nonlinear solids, where traditional first-order homogenization approaches often failed to capture critical behaviours like localization and failure processes. This approach was essential for modelling masonry, where the interaction between different phases—such as bricks and mortar—can significantly affect the material's response under stress. However, the complexity of implementing these higher-order terms, especially in large-scale simulations, remained a significant challenge.

The application of computational homogenization to masonry was further explored by Hollister and Kikuchi [46], who compared homogenization theory with standard mechanics analyses for periodic porous composites. Their study highlighted the limitations of traditional mechanics approaches in capturing the local strain energy distributions and effective stiffness in materials like

masonry, where the microstructure plays a critical role. By emphasizing the need for accurate boundary conditions and RVE configurations, this work laid the groundwork for the application of homogenization techniques in materials with complex microstructures, such as masonry.

Wriggers and Moftah [47] introduced mesoscale models that aimed to bridge the gap between microscale and macroscale analyses by incorporating damage behaviour into the homogenization process. Their work was particularly significant for masonry, where the damage typically initiates at the microstructural level before propagating to the macroscopic scale. The mesoscale approach allowed for a more detailed analysis of how microstructural damage influences the overall mechanical properties of masonry. However, their models tended to overestimate the material's behaviour due to the exclusion of the Interfacial Transition Zone (ITZ), highlighting the need for more comprehensive models that account for this critical aspect of masonry.

Larsson et al. [48] proposed a computational homogenization method based on a weak format of micro-periodicity, which offered greater flexibility in handling unstructured meshes and complex microstructures. This approach was particularly advantageous for masonry, where the microstructure often lacks the periodicity assumed in traditional homogenization techniques. By allowing for independent finite element discretization of boundary tractions, their method improved the robustness and accuracy of homogenization analyses. However, the method's effectiveness was somewhat limited by its reliance on the Ladyzhenskaya–Babuška–Brezzi (LBB) condition, which could complicate the analysis of materials with highly irregular microstructures, such as masonry.

As the field of computational mechanics advanced, the focus increasingly shifted toward integrating these methods into a cohesive framework that could accurately model the complex behaviour of masonry structures. The development of the Extended Finite Element Method (X-FEM) provided the necessary tools to handle the discontinuities and heterogeneities inherent in masonry, while computational homogenization offered a way to link microstructural characteristics with macroscopic behaviour.

The study by Sukumar et al. [49] marked a significant step forward in the application of X-FEM to quasi-static crack growth, providing a robust computational implementation that could handle complex crack paths without requiring frequent remeshing. This was particularly relevant for masonry, where the interaction between cracks and the microstructure can significantly influence

the material's overall behaviour. However, while the method effectively captured the behaviour of cracks in homogeneous materials, it was not specifically tailored for the multi-phase nature of masonry, where different materials (e.g., bricks and mortar) exhibit distinct mechanical properties.

Rethore et al. [50] introduced a stable numerical scheme for dynamic crack propagation with remeshing, addressing the challenges of maintaining numerical stability and energy balance during the simulation of evolving crack paths. Their method was particularly important for modelling masonry structures under dynamic loading conditions, such as earthquakes, where cracks can propagate unpredictably. The balance recovery method they developed ensured that energy conservation laws were upheld, improving the physical accuracy of the simulations. However, the method's reliance on remeshing could be computationally expensive, particularly for large-scale masonry structures where multiple cracks may need to be simulated simultaneously.

This study presents a novel X-FEM-based computational homogenization framework for masonry, overcoming the limitations of traditional FEM-based approaches by incorporating phase transitions and interface discontinuities within a structured finite element mesh. Unlike standard computational homogenization methods, which rely on predefined interface conditions, the proposed approach seamlessly integrates a Coulomb-based traction-separation law to model progressive bond degradation.

To ensure robustness, the framework systematically evaluates the impact of alternative RVE boundary conditions on homogenized properties. Validation against literature benchmarks and parametric studies confirms its ability to capture masonry's nonlinear response accurately. Unlike conventional finite element techniques, X-FEM eliminates the need for complex remeshing strategies, enabling a more flexible and computationally efficient representation of heterogeneous materials. By leveraging advanced crack propagation models and improved interface characterization, this framework provides a powerful tool for bridging the gap between microstructural details and macroscopic performance in masonry structures.

Chapter 3

Theoretical Framework and Numerical Implementation

3.1 Introduction to Homogenization Techniques

Homogenization is a mathematical method used to derive effective macroscopic properties of a heterogeneous material by averaging its microscale behaviour. It simplifies complex microstructures into an equivalent homogeneous medium, facilitating analysis and computation.

In materials like masonry, which consist of units (bricks or stones) and mortar joints, directly modelling every microstructural detail is computationally expensive and often impractical. Homogenization allows engineers to capture the essential mechanical behaviour of such materials without resolving every micro-feature, enabling efficient analysis of large-scale structures.

Consider a composite material with alternating layers of two different materials. Homogenization techniques can compute an effective stiffness that represents the combined response of these layers under load. This effective property can then be used in structural analyses without explicitly modelling each layer.

3.2 Displacement and Stress Fields in Heterogeneous Media

In heterogeneous materials, such as masonry structures, the presence of different materials and interfaces leads to complexities in displacement and stress fields. This section introduces the essential equations governing these fields and discusses how discontinuities are handled.

3.2.1 Nature of Displacement Discontinuities

Displacement discontinuities occur in heterogeneous media due to the presence of material interfaces, cracks, or other discontinuities. In masonry structures, the interfaces between masonry units and mortar joints can cause abrupt changes in displacement. These discontinuities arise for several physical reasons.

Firstly, material interfaces between different constituents, such as bricks and mortar, may have different mechanical properties, leading to variations in deformation responses under the same load. The mismatch in stiffness or thermal expansion coefficients can cause discontinuities at the interfaces.

Secondly, the presence of cracks and defects within the material introduces displacement jumps across the faces of the cracks. These defects can be due to manufacturing imperfections, environmental degradation, or mechanical loading beyond the material's strength.

Lastly, geometric irregularities in the structure, such as voids or inclusions, can result in non-uniform deformation. Variations in the geometry can concentrate stresses and strains in certain regions, causing localized displacement discontinuities.

Handling Discontinuities with XFEM

The Extended Finite Element Method (XFEM) extends the classical FEM by enriching the displacement approximation to capture discontinuities within elements. XFEM introduces additional functions, known as enrichment functions, to model the discontinuous behaviour without the need to remesh around discontinuities.

By incorporating these enrichment functions, XFEM can accurately represent discontinuities

within elements, enhancing the capability of FEM in modelling heterogeneous materials with displacement discontinuities.

3.3 Derivation of Governing Equations

This section provides a detailed derivation of the governing equations for elastic and nonlinear materials, starting from first principles and leading to the weak formulation suitable for numerical methods.

3.3.1 Equilibrium Equations

Basic Principles

The equilibrium of forces in a deformable body requires that the sum of internal and external forces be zero. Considering an infinitesimal volume element within the material, the balance of linear momentum in the absence of inertial effects is expressed as:

$$\frac{\partial \sigma_{ij}}{\partial x_j} + p_i = 0 \tag{1}$$

In this equation, σ_{ij} is the Cauchy stress tensor, representing internal stresses, and p_i is the body force per unit volume acting in the i-th direction, representing external forces such as gravity.

At any internal surface within the material, stress continuity must be maintained to ensure equilibrium. This condition is mathematically expressed by:

$$\sigma_{ij} n_j = t_i \tag{2}$$

Here, n_j is the outward unit normal to the surface, and t_i is the traction vector acting on the surface. This equation ensures that the internal stresses result in tractions that balance any applied forces across internal surfaces.

3.3.2 Boundary Conditions

To solve the equilibrium equations, appropriate boundary conditions must be specified. These conditions define how the material interacts with its surroundings and are essential for obtaining a unique solution.

Dirichlet boundary conditions, also known as displacement boundary conditions, prescribe the displacement on a portion of the boundary Γ_D of the domain Ω. They are expressed as:

$$\mathbf{u} = \mathbf{r} \quad \text{on} \quad \Gamma_D \tag{3}$$

In this expression, $\mathbf{u}$ is the displacement vector, and $\mathbf{r}$ is the specified displacement function on the boundary Γ_D. These conditions are applied to boundaries where the displacement is controlled, such as fixed supports.

Neumann boundary conditions, also known as traction boundary conditions, prescribe the traction on a portion of the boundary Γ_N. They are given by:

$$\sigma_{ij} n_j = -s_i \quad \text{on} \quad \Gamma_N \tag{4}$$

Here, s_i is the specified traction vector on the boundary Γ_N. These conditions are applied to boundaries where forces or stresses are applied, such as external loads.

The boundary of the domain $\partial\Omega$ is partitioned such that:

$$\partial\Omega = \Gamma = \Gamma_D \cup \Gamma_N \quad \text{and} \quad \Gamma_D \cap \Gamma_N = \emptyset \tag{5}$$

This ensures that the entire boundary is covered by either Dirichlet or Neumann conditions without overlap.

3.3.3 Conversion to Weak Formulation

The weak form of the equilibrium equations is derived to facilitate numerical solution methods like the finite element method (FEM). The process involves multiplying the equilibrium equations by a virtual displacement δu_i and integrating over the domain Ω.

Starting from the equilibrium equation:

$$\frac{\partial \sigma_{ij}}{\partial x_j} + p_i = 0 \tag{6}$$

Multiplying both sides by the virtual displacement δu_i yields:

$$\delta u_i \left(\frac{\partial \sigma_{ij}}{\partial x_j} + p_i \right) = 0 \tag{7}$$

Integrating over the domain Ω, we have:

$$\int_\Omega \delta u_i \frac{\partial \sigma_{ij}}{\partial x_j} d\Omega + \int_\Omega \delta u_i p_i d\Omega = 0 \tag{8}$$

Applying the divergence theorem (also known as integration by parts) to the first term:

$$\int_\Omega \delta u_i \frac{\partial \sigma_{ij}}{\partial x_j} d\Omega = -\int_\Omega \sigma_{ij} \frac{\partial \delta u_i}{\partial x_j} d\Omega + \int_\Gamma \delta u_i \sigma_{ij} n_j d\Gamma \tag{9}$$

Substituting back into Equation (8), we obtain:

$$-\int_\Omega \sigma_{ij} \frac{\partial \delta u_i}{\partial x_j} d\Omega + \int_\Gamma \delta u_i \sigma_{ij} n_j d\Gamma + \int_\Omega \delta u_i p_i d\Omega = 0 \tag{10}$$

The boundary integral involves the traction, which is specified on Γ_N. Since the virtual displacement δu_i is zero on Γ_D (due to the prescribed displacement), from Eq (4) we have:

$$\int_\Gamma \delta u_i \sigma_{ij} n_j d\Gamma = -\int_{\Gamma_N} \delta u_i s_i d\Gamma \tag{11}$$

Substituting this into the equation, the weak form becomes:

$$\int_\Omega \sigma_{ij} \frac{\partial \delta u_i}{\partial x_j} d\Omega + \int_{\Gamma_N} \delta u_i s_i d\Gamma + \int_\Omega \delta u_i p_i d\Omega = 0 \tag{12}$$

3.4 Multiscale modelling and Scale Separation

Multiscale modelling addresses the behaviour of materials with features at multiple length scales. This section explains the concepts of scale separation and the methods used to link micro-scale phenomena to macro-scale responses in the context of computational homogenization.

3.4.1 Concept of Scale Separation

In heterogeneous materials, two distinct spatial scales are considered. The macro-scale, denoted by coordinates x_i, represents the overall structure where the material is treated as effectively homogeneous. At this scale, the detailed microstructural features are not individually resolved. The micro-scale, denoted by coordinates y_i, represents the fine-scale structure where the heterogeneities, such as inclusions, voids, or grains, are explicitly considered. The micro-scale coordinates are related to the macro-scale coordinates by a small parameter η representing the ratio of the microstructural length scale to the macrostructural length scale [51] (see Figure. 3.1):

$$y_i = \frac{x_i}{\eta} \tag{13}$$

Scale separation is crucial because it allows us to model complex materials by decoupling the analysis at different scales. This separation is based on the assumption that the microstructural features are small compared to the dimensions of the structure ($\eta \ll 1$), enabling the use of homogenization techniques to compute effective properties that capture the influence of the microstructure on the macro-scale behaviour.

3.4.2 Asymptotic Expansion Techniques

To link the micro and macro scales, asymptotic expansions are employed for the displacement field and other quantities of interest.

The displacement field $u_i(x_i, y_i)$ is expanded as a series in terms of the small parameter η:

$$u_i(x_i, y_i) = \bar{u}_i(x_i) + \eta\bar{\bar{u}}_i(x_i, y_i) + \eta^2\bar{\bar{\bar{u}}}_i(x_i, y_i) + \dots \tag{14}$$

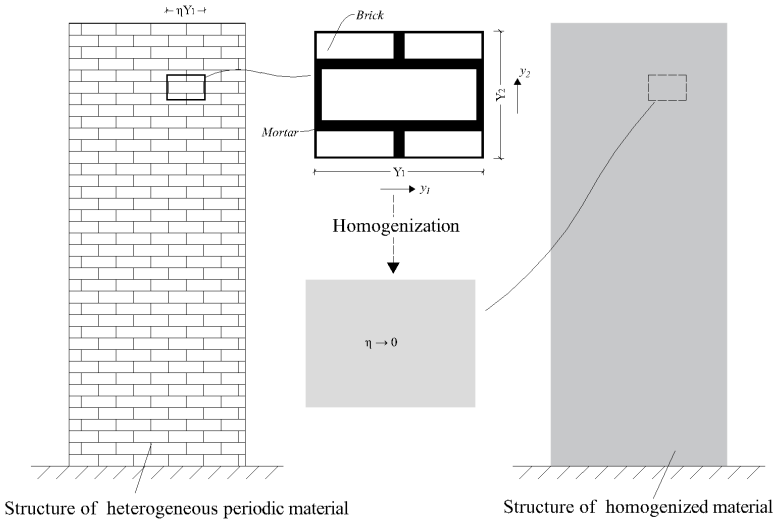

Figure 3.1: Homogenized material as a special case when inclusions are infinitesimally small, i.e.,$\eta \to 0$

In this expansion, $\bar{u}_i(x_i)$ represents the macro-scale displacement field, which characterizes the average behaviour of the material over the microstructure. The term $\bar{\bar{u}}_i(x_i, y_i)$ accounts for the first-order micro-scale fluctuations arising from material heterogeneity, capturing local deviations from the homogenized response. Higher-order terms, which describe finer-scale effects, are typically neglected in first-order homogenization due to their relatively minor contribution to the overall displacement field.

The leading term $\bar{u}_i(x_i)$ represents the smooth, slowly varying displacement field at the macro-scale, unaffected by microstructural variations. However, to accurately capture the effects of heterogeneity, the term $\eta\bar{\bar{u}}_i(x_i, y_i)$ introduces corrections that account for the influence of the microstructure, effectively capturing the rapid variations in displacement at the micro-scale.

When dealing with functions of both x_i and y_i, derivatives must account for variations at both scales. Using the chain rule, the derivative with respect to x_i transforms as (see [51]):

$$\frac{\partial}{\partial x_i} = \frac{\partial}{\partial x_i} + \frac{\partial y_j}{\partial x_i}\frac{\partial}{\partial y_j} \tag{15}$$

Since $y_j = x_j/\eta$, the derivative of y_j with respect to x_i is:

$$\frac{\partial y_j}{\partial x_i} = \frac{1}{\eta}\delta_{ij} \tag{16}$$

Thus, the total derivative becomes:

$$\frac{\partial}{\partial x_i} = \frac{\partial}{\partial x_i} + \frac{1}{\eta}\frac{\partial}{\partial y_i} \tag{17}$$

This expression reflects the contributions of both macro-scale and micro-scale variations to the total derivative.

3.4.3 First-Order Homogenization

Computation of the Displacement Gradient

Using the transformed derivative from Equation (17), the gradient of the displacement field is computed as:

$$\begin{aligned}\frac{\partial u_k}{\partial x_l} &= \left(\frac{\partial}{\partial x_l} + \frac{1}{\eta}\frac{\partial}{\partial y_l}\right)\left(\bar{u}_k + \eta\bar{\bar{u}}_k + \eta^2\bar{\bar{\bar{u}}}_k + \dots\right) \\ &= \frac{\partial \bar{u}_k}{\partial x_l} + \frac{1}{\eta}\frac{\partial \bar{\bar{u}}_k}{\partial y_l} + \frac{\partial \bar{\bar{u}}_k}{\partial y_l} + \eta\left(\frac{\partial \bar{\bar{u}}_k}{\partial x_l} + \frac{\partial \bar{\bar{\bar{u}}}_k}{\partial y_l}\right) + \dots .\end{aligned} \tag{18}$$

In deriving this expression, we have used the fact that $\bar{u}_k$ depends only on the macro-scale coordinates x_j, so $\dfrac{\partial \bar{u}_k}{\partial y_l} = 0$.

Expansion of the Strain Tensor

The strain tensor ϵ_{kl} is defined by:

$$\epsilon_{kl} = \frac{1}{2}\left(\frac{\partial u_k}{\partial x_l} + \frac{\partial u_l}{\partial x_k}\right). \tag{19}$$

Substituting the expanded displacement gradients from Equation (18), we obtain:

$$\epsilon_{kl} = \frac{1}{2}\left(\frac{1}{\eta}\left(\frac{\partial \bar{\bar{u}}_k}{\partial y_l} + \frac{\partial \bar{\bar{u}}_l}{\partial y_k}\right) + \left(\frac{\partial \bar{u}_k}{\partial x_l} + \frac{\partial \bar{u}_l}{\partial x_k}\right) + \left(\frac{\partial \bar{\bar{u}}_k}{\partial y_l} + \frac{\partial \bar{\bar{u}}_l}{\partial y_k}\right) + \dots\right). \tag{20}$$

Grouping terms according to their order in η, the strain tensor can be expressed as:

$$\epsilon_{kl} = \frac{1}{\eta}\epsilon_{kl}^{(-1)} + \epsilon_{kl}^{(0)} + \eta\epsilon_{kl}^{(1)} + \dots, \tag{21}$$

where:

$$\epsilon_{kl}^{(-1)} = \frac{1}{2}\left(\frac{\partial \bar{\bar{u}}_k}{\partial y_l} + \frac{\partial \bar{\bar{u}}_l}{\partial y_k}\right), \tag{22}$$

$$\epsilon_{kl}^{(0)} = \frac{1}{2}\left(\frac{\partial \bar{u}_k}{\partial x_l} + \frac{\partial \bar{u}_l}{\partial x_k}\right) + \frac{1}{2}\left(\frac{\partial \bar{\bar{u}}_k}{\partial y_l} + \frac{\partial \bar{\bar{u}}_l}{\partial y_k}\right). \tag{23}$$

Expansion of the Stress Tensor

Using the constitutive relation for linear elasticity:

$$\sigma_{ij} = D_{ijkl}\epsilon_{kl}, \tag{24}$$

where D_{ijkl} is the stiffness tensor, which may vary with the micro-scale coordinates y_j in heterogeneous materials. Substituting the expanded strain tensor from Equation (21) into the constitutive relation, we obtain:

$$\sigma_{ij} = D_{ijkl}\left(\frac{1}{\eta}\epsilon_{kl}^{(-1)} + \epsilon_{kl}^{(0)} + \eta\epsilon_{kl}^{(1)} + \dots\right). \tag{25}$$

This expansion leads to:

$$\sigma_{ij} = \frac{1}{\eta}\sigma_{ij}^{(-1)} + \sigma_{ij}^{(0)} + \eta\sigma_{ij}^{(1)} + \dots, \tag{26}$$

where:

$$\sigma_{ij}^{(-1)} = D_{ijkl}\epsilon_{kl}^{(-1)}, \tag{27}$$

$$\sigma_{ij}^{(0)} = D_{ijkl}\epsilon_{kl}^{(0)}. \tag{28}$$

Substitution into the Equilibrium Equation

The equilibrium equation in the absence of body forces is:

$$\frac{\partial \sigma_{ij}}{\partial x_j} = 0. \tag{29}$$

Substituting the transformed derivative from Equation (17) and the expanded stress tensor from Equation (26), we have:

$$\left(\frac{\partial}{\partial x_j} + \frac{1}{\eta}\frac{\partial}{\partial y_j}\right)\left(\frac{1}{\eta}\sigma_{ij}^{(-1)} + \sigma_{ij}^{(0)} + \eta\sigma_{ij}^{(1)} + \dots\right) = 0. \tag{30}$$

Expanding the derivatives, we obtain:

$$\frac{1}{\eta^2}\frac{\partial \sigma_{ij}^{(-1)}}{\partial y_j} + \frac{1}{\eta}\left(\frac{\partial \sigma_{ij}^{(-1)}}{\partial x_j} + \frac{\partial \sigma_{ij}^{(0)}}{\partial y_j}\right) + \left(\frac{\partial \sigma_{ij}^{(0)}}{\partial x_j} + \frac{\partial \sigma_{ij}^{(1)}}{\partial y_j}\right) + \dots = 0. \tag{31}$$

Equating Terms of the Same Order

To satisfy the equilibrium equation at all scales, the coefficients of each power of η must individually equal zero.

At order η^{-2}:

$$\frac{\partial \sigma_{ij}^{(-1)}}{\partial y_j} = 0. \tag{32}$$

This equation represents the micro-scale equilibrium equation within the representative volume element (RVE).

At order η^{-1}:

$$\frac{\partial \sigma_{ij}^{(-1)}}{\partial x_j} + \frac{\partial \sigma_{ij}^{(0)}}{\partial y_j} = 0. \tag{33}$$

However, since $\sigma_{ij}^{(-1)}$ depends only on the micro-scale coordinates y_j, its derivative with respect to x_j is zero, i.e., $\dfrac{\partial \sigma_{ij}^{(-1)}}{\partial x_j} = 0$. Therefore, Equation (33) simplifies to:

$$\frac{\partial \sigma_{ij}^{(0)}}{\partial y_j} = 0. \tag{34}$$

This equation implies that the macro-scale stress $\sigma_{ij}^{(0)}$ is in equilibrium with respect to the micro-scale coordinates, which is consistent with the assumption that macro-scale stresses vary slowly and are independent of y_j.

Micro-Scale Equilibrium Equation

Returning to the micro-scale equilibrium equation at order η^{-2} given by Equation (37), and substituting $\sigma_{ij}^{(-1)}$ from Equation (27), we have:

$$\frac{\partial}{\partial y_j}\left[D_{ijkl}\epsilon_{kl}^{(-1)}\right] = 0. \tag{35}$$

Substituting $\epsilon_{kl}^{(-1)}$ from Equation (22), the micro-scale equilibrium equation becomes:

$$\frac{\partial}{\partial y_j}\left[D_{ijkl}\frac{1}{2}\left(\frac{\partial \bar{\bar{u}}_k}{\partial y_l} + \frac{\partial \bar{\bar{u}}_l}{\partial y_k}\right)\right] = 0. \tag{36}$$

This equation governs the equilibrium of the micro-scale displacement fluctuations $\bar{\bar{u}}_i$ within the RVE. It is essential for determining the microstructural response and computing the effective material properties in the homogenization process.

By substituting the asymptotic expansions into the governing equations and systematically collecting terms of the same order in η, we have derived the micro-scale equilibrium equation at order η^{-2}. This equation is fundamental in first-order homogenization, as it allows us to solve for the micro-scale fluctuations and, consequently, to determine the effective behaviour of the heterogeneous material at the macro-scale.

For the equilibrium equation, after substituting the expanded displacement field and applying

Equation (17), the terms of order η^{-1} lead to the micro-scale equilibrium equation:

$$\frac{\partial \tilde{\sigma}_{ij}}{\partial y_j} = 0 \tag{37}$$

Here, $\tilde{\sigma}_{ij}$ is the stress tensor associated with the first-order micro-scale displacement $\bar{\bar{u}}_i$. This equation represents the equilibrium at the micro-scale within the representative volume element (RVE).

At order η^0, the macro-scale equilibrium equation coupled with micro-scale fluctuations is obtained:

$$\frac{\partial \bar{\sigma}_{ij}}{\partial x_j} + \frac{\partial \tilde{\sigma}_{ij}}{\partial y_j} + p_i = 0 \tag{38}$$

Here, $\bar{\sigma}_{ij}$ is the macro-scale stress tensor related to the macro-scale displacement $\bar{u}_i$.

Equation (37) governs the equilibrium at the micro-scale and must be satisfied within the RVE for any point y_j. Equation (38) couples the macro and micro scales, indicating that the divergence of the macro-scale stress and the micro-scale stress fluctuations, along with body forces, must balance.

By solving the micro-scale problem defined by Equation (37), we can determine the microstructural response and compute effective material properties. These properties are then used in the macro-scale equations to predict the overall behaviour of the heterogeneous material.

3.5 Variational Principles in Homogenization

Variational principles provide a powerful framework for deriving governing equations and understanding the behaviour of materials. In homogenization, the Hill-Mandel macro-homogeneity condition is fundamental for ensuring energy consistency between scales.

3.5.1 Formulation of the Micro-Scale Problem

The formulation of the micro-scale problem involves deriving the equilibrium equations within the representative volume element (RVE) and establishing the constitutive relations that govern the micro-scale material behaviour.

To ensure equilibrium within the RVE, we start by considering the divergence of the micro-scale stress tensor. The equilibrium equation, which must hold at all points within the RVE domain Y, is expressed as follows:

$$\frac{\partial \sigma_{ij}}{\partial y_j} = 0 \quad \text{in} \quad Y \tag{39}$$

This equation ensures that the internal stresses are balanced at the micro-scale, aligning with the overall equilibrium requirements of the heterogeneous material.

Next, the local constitutive relations at the micro-scale are defined to describe the material's response. The stress-strain relationship at this scale is given by:

$$\sigma_{ij} = D_{ijkl}(y_k) \left(\frac{\partial \bar{u}_k}{\partial x_l} + \frac{\partial \bar{\bar{u}}_k}{\partial y_l} \right) \tag{40}$$

Here, $D_{ijkl}(y_k)$ represents the position-dependent stiffness tensor at the micro-scale, capturing the material's heterogeneity. The total strain is decomposed into two components: the macro-scale strain $\frac{\partial \bar{u}_k}{\partial x_l}$, representing the average deformation over the RVE, and the micro-scale fluctuation strain $\frac{\partial \bar{\bar{u}}_k}{\partial y_l}$, which accounts for local variations within the microstructure. This decomposition allows for a more accurate representation of the material response by separating global deformation effects from microstructural fluctuations.

3.5.2 Representative Volume Element (RVE) Analysis

The Representative Volume Element (RVE) is a critical component in homogenization analysis. It serves as a statistical sample of the material's microstructure, embodying all essential features required to derive effective properties that represent the larger material body. To ensure accurate results, the RVE must be large enough to capture the material's heterogeneity adequately, including features like inclusions, voids, and grains, while remaining small relative to the macrostructural dimensions. This balance allows the RVE to satisfy the scale separation assumption, which is fundamental to homogenization.

Choosing an appropriate RVE is pivotal, as it directly affects the reliability of the homogenized

properties. An RVE that accurately reflects the microstructural characteristics ensures that the derived properties are representative of the material as a whole, thus enhancing the applicability of the homogenized model in macro-scale simulations.

3.5.3 Boundary Value Problems for the Representative Volume Element (RVE)

In the context of first-order homogenization, the solution of the micro-scale equilibrium equations requires the introduction of a Representative Volume Element (RVE). The RVE serves as a fundamental building block that captures the essential features of the material's microstructure. This section discusses the significance of boundary conditions applied to the RVE and derives the corresponding equations necessary for computational homogenization.

The choice of boundary conditions imposed on the RVE significantly affects the calculated effective material properties [44]. Since the RVE is of finite size due to a non-zero scale parameter η, homogenization becomes approximate unless exact boundary conditions are applied. However, the exact boundary conditions are generally unknown *a priori*. Therefore, suitable assumptions must be made to render the problem tractable.

Three common types of boundary conditions are considered in homogenization:

Periodic Boundary Conditions Periodic boundary conditions assume that the displacement and traction fields are periodic across opposite faces of the RVE. This approach is suitable for materials with a periodic microstructure, where the RVE is representative of the repeating unit cell. Mathematically, the periodicity conditions can be expressed as:

$$u_i(\psi_i + L_j) = u_i(\psi_i), \tag{41}$$

$$\sigma_{ij}(\psi_i + L_j)n_j = \sigma_{ij}(\psi_i)n_j, \tag{42}$$

where L_j is the length of the RVE in the j-th direction, and n_j is the outward normal vector on the boundary surface Ψ of the RVE.

Dirichlet Boundary Conditions Dirichlet boundary conditions prescribe the displacement on the boundary of the RVE, corresponding to the application of a macroscopic strain. The displacement field on the boundary Ψ is specified as:

$$u_i(\psi_i) = g_{i,j}\psi_j, \tag{43}$$

where $g_{i,j} = \dfrac{\partial \bar{u}_i}{\partial x_j}$ is the specified average displacement gradient field obtained from the macro-scale problem.

Neumann Boundary Conditions Neumann boundary conditions prescribe the traction on the boundary of the RVE, corresponding to the application of a macroscopic stress. The traction vector on the boundary is given by:

$$\sigma_{ij}(\psi_i)n_j = \bar{\sigma}_{ij}n_j, \tag{44}$$

where $\bar{\sigma}_{ij}$ is the macroscopic stress tensor.

The selection of boundary conditions influences the micro-scale fluctuations and, consequently, the effective properties obtained from the homogenization process. As shown by [44], both the choice of boundary conditions and the size of the RVE affect the homogenized mechanical properties. Therefore, it is critical to predict and implement appropriate boundary conditions to accurately capture the material behaviour.

To solve the micro-scale equilibrium problem within the RVE, we consider the equilibrium equation derived from the first-order homogenization process:

$$\frac{\partial}{\partial y_j}\left[D_{ijkl}(y_k)\left(g_{k,j} + \frac{\partial \bar{\bar{u}}_k}{\partial y_j}\right)\right] = 0 \quad \text{in} \quad V_{RVE}, \tag{45}$$

where:

- $D_{ijkl}(y_k)$ is the local stiffness tensor that varies with the micro-scale coordinates y_k.
- $g_{k,j} = \dfrac{\partial \bar{u}_k}{\partial x_j}$ is the macroscopic displacement gradient.
- $\bar{\bar{u}}_k$ represents the micro-scale displacement fluctuation.

Since the exact boundary conditions are not known, we express the displacement field on the RVE boundary Ψ by incorporating the micro-scale fluctuations. The displacement at a boundary point $\psi_i \in \Psi$ is given by:

$$u_i(\psi_i) = \bar{u}_i(\bar{y}_i) + (\psi_j - \bar{y}_j)g_{i,j} + \eta\bar{\bar{u}}_i(\psi_i), \tag{46}$$

where:

- $\bar{y}_i = \dfrac{1}{|V_{RVE}|}\int_{V_{RVE}} y_i \, dY$ refers to the centroid of the RVE.
- $\eta\bar{\bar{u}}_i(\psi_i)$ is the contribution of the micro-fluctuations at the boundary, which is generally unknown.

For convenience and without loss of generality, we can choose the origin of the RVE coordinates at the centroid, i.e., $\bar{y}_i = 0$, and assume that the average displacement at the centroid is zero, $\bar{u}_i(\bar{y}_i) = 0$. This simplifies Equation (46) to:

$$u_i(\psi_i) = \psi_j g_{i,j} + \eta\bar{\bar{u}}_i(\psi_i). \tag{47}$$

The micro-fluctuations $\eta\bar{\bar{u}}_i(\psi_i)$ are influenced by the microstructural heterogeneities and the finite size of the RVE. Since these fluctuations are generally unknown, their effect on the effective properties must be carefully considered.

To enforce the macroscopic deformation on the RVE, we consider that the forcing term for the deformation of the RVE is the constant average displacement gradient. The following relation must be satisfied:

$$\frac{1}{2}\int_{S_{RVE}} (u_i n_j + u_j n_i) \, d\Psi = g_{i,j}\int_{V_{RVE}} dY, \tag{48}$$

where n_i is the outward normal vector on the RVE boundary S_{RVE}, and $d\Psi$ is the differential surface area element.

By introducing $\lambda_i = n_j\sigma_{ij}$ as the Lagrange multiplier vector to enforce the constraint in Equation (48) [52], As [26] formulated the weak form of the boundary value problem. The virtual work

principle leads to:

$$\int_{V_{RVE}} \delta \frac{\partial \bar{\bar{u}}_i}{\partial y_j} \bar{g}_{i,j} \mathrm{dY} - \int_{S_{RVE}} \delta \bar{\bar{u}}_i \lambda_i \mathrm{d}\Psi - \int_{S_{RVE}} \delta \lambda_i \left(u_i - \psi_j \bar{g}_{ij} \right) \mathrm{d}\Psi = 0 \tag{49}$$

In this formulation, the first term represents the internal virtual work within the RVE due to micro-scale fluctuations. The second term enforces the boundary conditions through the Lagrange multiplier λ_i, which serves as the traction vector on the boundary. Finally, the third term ensures the compatibility of displacements along the RVE boundary, maintaining continuity and consistency in the homogenization framework.

By solving Equation (49), subject to the appropriate boundary conditions, the micro-scale displacement fluctuations $\bar{\bar{u}}_i$ can be determined. The Lagrange multipliers λ_i provide the necessary tractions to satisfy equilibrium and compatibility conditions.

The choice of boundary conditions directly affects the micro-scale stress and strain fields within the RVE. For instance, imposing uniform displacement boundary conditions (Dirichlet type) may underestimate the stiffness, while uniform traction boundary conditions (Neumann type) may overestimate it. Periodic boundary conditions often provide a balance by allowing the microstructure to deform more naturally.

As the size of the RVE increases, the influence of the boundary conditions diminishes, and the effective properties converge to intrinsic material properties. However, computational limitations often restrict the size of the RVE, making the appropriate selection of boundary conditions even more critical.

Importance of RVE Size and Boundary Conditions

The RVE must be sufficiently large to be statistically representative of the material's microstructure. A too-small RVE may not capture the variability and interactions of the microstructural features, leading to inaccurate effective properties. On the other hand, a larger RVE increases computational cost.

Moreover, due to the finite size of the RVE (i.e., $\eta \neq 0$), the homogenization is approximate unless exact boundary conditions are imposed. The Hill-Mandel macro-homogeneity condition

assumes scale separation, which may not hold precisely for finite RVEs. Consequently, the boundary conditions influence the effective modulus by affecting the stress and strain distributions within the RVE.

Studies such as [44] have demonstrated the effects of both the chosen boundary conditions and the RVE size on the homogenized mechanical properties. They showed that periodic boundary conditions often yield the best approximation of the effective properties for materials with periodic or statistically homogeneous microstructures.

Implementation in Computational Homogenization

In computational homogenization, the RVE problem is solved numerically using finite element methods. The implementation involves discretizing the RVE domain and applying the chosen boundary conditions to the finite element model.

For periodic boundary conditions, special care is taken to ensure that nodes on opposite faces of the RVE are coupled to enforce displacement continuity and traction periodicity. Dirichlet and Neumann boundary conditions are applied by specifying displacements or tractions on the boundary nodes, respectively.

The computed micro-scale fields are then used to calculate the effective material properties. The homogenized stress $\bar{\sigma}_{ij}$ and strain $\bar{\epsilon}_{ij}$ tensors are obtained by averaging the micro-scale quantities over the RVE:

$$\bar{\sigma}_{ij} = \frac{1}{|V_{RVE}|} \int_{V_{RVE}} \sigma_{ij} \, dY, \tag{50}$$

$$\bar{\epsilon}_{ij} = \frac{1}{|V_{RVE}|} \int_{V_{RVE}} \epsilon_{ij} \, dY. \tag{51}$$

These homogenized quantities are then used in the macro-scale analysis to predict the overall behaviour of the heterogeneous material.

The boundary value problem for the RVE is a critical component in computational homogenization. The selection of appropriate boundary conditions and the consideration of the RVE size are essential for accurately determining the effective material properties. By thoroughly understanding

and correctly implementing these aspects, the multiscale modelling approach provides a powerful tool for analysing and designing complex heterogeneous materials such as masonry structures.

3.6 Numerical Methods for Homogenization

This section introduces the numerical methods employed to solve the homogenization problem for heterogeneous materials, focusing on the Finite Element Method (FEM) and the Extended Finite Element Method (XFEM). These methods are essential for implementing computational homogenization, particularly when dealing with materials that exhibit discontinuities, such as cracks or material interfaces in masonry structures. The framework is extended to account for nonlinear behaviours, including nonlinear traction-separation laws and nonlinear constitutive models.

3.6.1 Finite Element Method Overview

The Finite Element Method (FEM) is a numerical technique for finding approximate solutions to boundary value problems for partial differential equations (PDEs). It subdivides a large problem into smaller, simpler parts called finite elements. In the context of elasticity, FEM discretizes the domain Ω into smaller elements over which the unknown displacement field $\mathbf{u}$ is approximated using interpolation functions.

Discretization and Interpolation Functions

The domain Ω is divided into N_e finite elements. Within each element e, the displacement field $\mathbf{u}$ is approximated in terms of nodal displacement parameters $\mathbf{a}$ using shape functions $\mathbf{A}$:

$$\mathbf{u} = \mathbf{A}\mathbf{a}, \tag{52}$$

where:

- $\mathbf{A}$ is the matrix of shape functions for the element.
- $\mathbf{a}$ is the vector of nodal displacement parameters after discretization.

Additionally, the Lagrange multiplier field $\boldsymbol{\lambda}$ is approximated as:

$$\boldsymbol{\lambda} = \mathbf{G}\mathbf{h}, \tag{53}$$

where:

- $\mathbf{G}$ is the vector of selected approximation functions for $\boldsymbol{\lambda}$.
- $\mathbf{h}$ is the vector of unknown parameters after discretization.

The shape functions are chosen such that they interpolate the displacements at the nodes of the element.

Enrichment Functions and Displacement Field Approximation

In computational mechanics, particularly when modelling materials with discontinuities (like cracks), it is essential to represent the displacement field accurately. The Extended Finite Element Method (XFEM) allows us to model such discontinuities within finite elements by enriching the standard displacement approximation.

The displacement field within an element, denoted by $\mathbf{u}$, can be described by combining both continuous and discontinuous components. Following [13], it is expressed as:

$$\mathbf{u} = \mathbf{N}\mathbf{d} + \mathbf{H}\big|_{\Gamma_I}\mathbf{N}\boldsymbol{\beta} \tag{54}$$

In this equation, $\mathbf{u}$ represents the displacement vector at any point within the element. The matrix $\mathbf{N}$ contains the standard bilinear finite element shape functions,

$$\mathbf{N} = \begin{bmatrix} N_1 & 0 & N_2 & 0 & N_3 & 0 & N_4 & 0 \\ 0 & N_1 & 0 & N_2 & 0 & N_3 & 0 & N_4 \end{bmatrix} \tag{55}$$

and $\mathbf{d}$ is the column vector of nodal displacement values, also referred to as degrees of freedom (DOFs). The term $\mathbf{H}\big|_{\Gamma_I}$ represents the Heaviside function evaluated at the discontinuity interface Γ_I, while $\boldsymbol{\beta}$ is the vector of enriched degrees of freedom, which accounts for the displacement jump at the discontinuity. Essentially, the displacement field consists of two parts: a continuous

component, represented by $\mathbf{Nd}$, and a discontinuous component, captured by $\mathbf{H}\big|_{\Gamma_I}\mathbf{N}\boldsymbol{\beta}$, which addresses the jump in displacement across the discontinuity interface.

The nodal displacement vector $\mathbf{d}$ is defined for a 2D quadrilateral element with four nodes, each having two displacement components (one for each direction, x and y), resulting in eight degrees of freedom (DOFs), as follows:

$$\mathbf{d} = \begin{bmatrix} d_{11} & d_{12} & d_{21} & d_{22} & d_{31} & d_{32} & d_{41} & d_{42} \end{bmatrix}^T \tag{56}$$

Here, d_{ij} refers to the displacement component at node i in direction j.

Similarly, the enriched degrees of freedom $\boldsymbol{\beta}$ associated with the displacement jump at the discontinuity interface are defined as:

$$\boldsymbol{\beta} = \begin{bmatrix} \beta_{11} & \beta_{12} & \beta_{21} & \beta_{22} & \beta_{31} & \beta_{32} & \beta_{41} & \beta_{42} \end{bmatrix}^T \tag{57}$$

These enriched DOFs allow for the representation of the displacement discontinuity at each node, effectively capturing the behaviour of materials with cracks or other types of discontinuities.

The combined shape function matrix $\mathbf{A}$ and the combined DOF vector $\mathbf{a}$ are expressed as:

$$\mathbf{A} = \begin{bmatrix} \mathbf{N} & \mathbf{H}\big|_{\Gamma_I}\mathbf{N} \end{bmatrix} \tag{58}$$

$$\mathbf{a}^T = \begin{bmatrix} \mathbf{d}^T & \boldsymbol{\beta}^T \end{bmatrix} \tag{59}$$

It is important to note that boundary conditions are applied only to the standard nodal displacements $\mathbf{d}$, while the enriched DOFs $\boldsymbol{\beta}$, which represent the discontinuity, are not subjected to the same boundary constraints.

At the discontinuity interface, the displacement jump $[[\mathbf{u}]]$ is defined as:

$$[[\mathbf{u}]] = \mathbf{N}\big|_{\Gamma_I}\boldsymbol{\beta} \tag{60}$$

This jump is derived from the displacement field, where the Heaviside function $\mathbf{H}\big|_{\Gamma_I}$ changes sign at the interface Γ_I, introducing the discontinuity. The displacement jump depends solely on

the enriched DOFs $\boldsymbol{\beta}$ and the shape functions evaluated at the discontinuity interface.

The stress field $\boldsymbol{\sigma}$ in the bulk material is computed as:

$$\boldsymbol{\sigma} = \mathbf{D}\left(\mathbf{B}\mathbf{d} + \mathbf{H}\big|_{\Gamma_I}\mathbf{B}\boldsymbol{\beta}\right) \tag{61}$$

The traction vector $\mathbf{t}$ at the discontinuity interface is related to the displacement jump via the interface stiffness matrix $\mathbf{T}$ as follows:

$$\mathbf{t} = \mathbf{T}\boldsymbol{\delta}\big|_{\Gamma_I}\mathbf{N}\boldsymbol{\beta} \tag{62}$$

where $\boldsymbol{\delta}\big|_{\Gamma_I}$ is the Dirac delta function localized at the discontinuity interface Γ_I. The interface stiffness matrix $\mathbf{T}$ is defined as:

$$\mathbf{T} = k\mathbf{I} \tag{63}$$

In this equation, k is the interface stiffness coefficient, and $\mathbf{I}$ represents the 2×2 identity matrix. The traction vector $\mathbf{t}$ is energetically conjugate to the displacement jump $[[\mathbf{u}]]$ and consists of two components corresponding to the normal and tangential directions along the interface in 2D space.

Additionally, the Lagrange multiplier field is interpolated using the following matrix of shape functions:

$$\mathbf{G} = \begin{bmatrix} L_1 & 0 & L_2 & 0 \\ 0 & L_1 & 0 & L_2 \end{bmatrix} \tag{64}$$

where L_1 and L_2 are linear interpolation functions along the element edge. These functions are defined as:

$$L_1 = \frac{0.5l - z_b}{l}, \quad L_2 = \frac{0.5l + z_b}{l} \tag{65}$$

Through this methodology, we have developed a displacement interpolation scheme that accounts for discontinuities within finite elements using enrichment functions. We have defined both the standard and enriched degrees of freedom, organized into the vectors $\mathbf{d}$ and $\boldsymbol{\beta}$, respectively.

Expressions for the displacement jump across the discontinuity interface Γ_I and the stress field in terms of the displacement field have been derived, incorporating both continuous and discontinuous components. Additionally, the traction vector at the discontinuity interface has been related to the displacement jump via the interface stiffness matrix $\mathbf{T}$. Finally, we have interpolated the Lagrange multiplier field along the element edges using linear shape functions to enforce constraints effectively. This approach allows us to model complex material behaviour, such as crack initiation and propagation, within the finite element framework.

3.7 Advanced Iterative Framework for Nonlinear RVE Analysis

Nonlinear analysis of Representative Volume Elements (RVEs) demands a robust computational framework capable of addressing the coupling between macroscopic and microscopic responses under complex boundary conditions. This section introduces an iterative solution approach based on the Newton-Raphson method, designed to solve the nonlinear equilibrium equations governing RVE behaviour. The procedure incorporates residual corrections, incremental updates, and a detailed handling of boundary conditions.

3.7.1 Newton-Raphson Procedure for the Nonlinear Solution of the RVE Problem

The Newton-Raphson method is a widely used iterative technique for solving nonlinear systems of equations. In the context of the RVE problem, this method is employed to solve the nonlinear equilibrium equations involving displacements and Lagrange multipliers under complex boundary conditions. The nonlinearities arise primarily from cohesive traction-separation laws at the interfaces.

The governing system of equations at each iteration (j) can be expressed by substituting Eqs. (52) and (53) into Eq. (49) as:

$$\begin{bmatrix} \mathbf{K}^{(j)} & \mathbf{S}^{\mathrm{T}} \\ \mathbf{S} & \mathbf{0} \end{bmatrix} \begin{Bmatrix} \delta\mathbf{a}^{(j)} \\ \delta\mathbf{h}^{(j)} \end{Bmatrix} = \begin{Bmatrix} -\mathbf{r}_{\mathbf{a}}^{(j)} \\ \boldsymbol{\Theta}\Delta\bar{\mathbf{g}} - \mathbf{r}_{\mathbf{h}}^{(j)} \end{Bmatrix}, \tag{66}$$

where:

- $\mathbf{K}^{(j)}$: the tangent stiffness matrix at iteration (j),
- $\mathbf{S}$: the constraint matrix derived as $\mathbf{S} = \int_{S_{RVE}} \mathbf{G}^{\mathrm{T}}\mathbf{A}\,\mathrm{d}\Psi$,
- $\mathbf{\Theta}$: a coupling matrix defined as $\mathbf{\Theta} = \int_{S_{RVE}} \mathbf{G}^{\mathrm{T}}\mathbf{\Psi}^{\mathrm{T}}\,\mathrm{d}\Psi$,
- $\delta\mathbf{a}^{(j)}$: the iterative nodal displacement increment, including standard and enriched DOFs,
- $\delta\mathbf{h}^{(j)}$: the iterative increment of Lagrange multipliers,
- $\mathbf{r}_{\mathbf{a}}^{(j)}$: the residual of the equilibrium condition at the end of iteration (j), given as:

$$\mathbf{r}_{\mathbf{a}}^{(j)} = \int_{V_{RVE}} \frac{\partial \mathbf{A}^{\mathrm{T}}}{\partial \mathbf{y}} \boldsymbol{\sigma}^{(j)}\,\mathrm{dY} + \int_{\Gamma_{DI}} \mathbf{B}^{\mathrm{T}}\mathbf{H}_{\Gamma_{DI}}^{\mathrm{T}}\mathbf{t}^{(j)}\,\mathrm{d}\Gamma, \tag{67}$$

- $\mathbf{r}_{\mathbf{h}}^{(j)}$: the residual associated with the boundary constraints, given as:

$$\mathbf{r}_{\mathbf{h}}^{(j)} = \int_{S_{RVE}} \mathbf{G}^{\mathrm{T}}\boldsymbol{\lambda}^{(j)}\,\mathrm{d}\Psi. \tag{68}$$

The iterative solution proceeds as follows. First, the incremental displacements and Lagrange multipliers are updated at each iteration using:

$$\Delta\mathbf{a}^{(j)} = \Delta\mathbf{a}^{(j-1)} + \delta\mathbf{a}^{(j)}, \quad \Delta\mathbf{h}^{(j)} = \Delta\mathbf{h}^{(j-1)} + \delta\mathbf{h}^{(j)}. \tag{69}$$

The displacements are decomposed into:

$$\delta\mathbf{a}^{(j)} = \delta\mathbf{a}_{\mathbf{p}}^{(j)} + \delta\mathbf{a}_{\mathbf{r}}^{(j)}, \tag{70}$$

where:

$$\delta\mathbf{a}_{\mathbf{r}}^{(j)} = -\mathbf{K}^{-1}\mathbf{r}_{\mathbf{a}}^{(j)}, \quad \delta\mathbf{a}_{\mathbf{p}}^{(j)} = -\mathbf{K}^{-1}\mathbf{S}^{\mathrm{T}}\delta\mathbf{h}^{(j)}. \tag{71}$$

The increment of Lagrange multipliers, $\delta\mathbf{h}^{(j)}$, is determined from the second row of Eq. (66) as:

$$\delta\mathbf{h}^{(j)} = -\left[\mathbf{S}\mathbf{K}^{-1}\mathbf{S}^{\mathrm{T}}\right]^{-1}\left[\mathbf{\Theta}\Delta\bar{\mathbf{g}} - \mathbf{r}_{\mathbf{h}}^{(j)} - \mathbf{S}\delta\mathbf{a}_{\mathbf{r}}^{(j)}\right]. \tag{72}$$

Finally, the nonlinear traction-separation law governing the cohesive interfaces introduces the primary source of nonlinearity in the system. The traction, $\mathbf{t}^{(j)}$, depends on the displacement jump, $\boldsymbol{\beta}^{(j)}$, as:

$$\mathbf{t}^{(j)} = \mathbf{t}(\boldsymbol{\beta}^{(j)}), \tag{73}$$

and the detailed procedure for updating the traction is provided in Section 3.8.

The iterative procedure continues until the residuals satisfy the convergence criteria:

$$\|\mathbf{r}_{\mathbf{a}}^{(j)}\| \leq \epsilon, \quad \|\mathbf{r}_{\mathbf{h}}^{(j)}\| \leq \epsilon, \tag{74}$$

where ϵ is the prescribed tolerance for convergence.

This procedure ensures an accurate and systematic solution to the nonlinear RVE problem, accounting for the coupling between macroscopic strain and microscopic response.

3.7.2 Partitioning into Interior and Boundary Nodes

The partitioning of the global matrices and vectors into interior and boundary components is a critical step in the solution procedure. This decomposition simplifies the application of boundary conditions and allows for the efficient computation of the system's response.

The global stiffness matrix $\mathbf{K}^{(j)}$, constraint matrix $\mathbf{S}$, and residual vector $\mathbf{r}_{\mathbf{a}}^{(j)}$ are partitioned as follows:

$$\mathbf{K}^{(j)} = \begin{bmatrix} \mathbf{K}_{II} & \mathbf{K}_{IB} \\ \mathbf{K}_{IB}^{\mathrm{T}} & \mathbf{K}_{BB} \end{bmatrix}, \quad \mathbf{S} = \begin{bmatrix} \mathbf{S}_I & \mathbf{S}_B \end{bmatrix}, \quad \mathbf{r}_{\mathbf{a}}^{(j)} = \begin{Bmatrix} \mathbf{r}_{\mathbf{a}_I}^{(j)} \\ \mathbf{r}_{\mathbf{a}_B}^{(j)} \end{Bmatrix}, \tag{75}$$

So:

$$\mathbf{K}^{(j)}\delta\mathbf{a}^{(j)} = \begin{bmatrix} \mathbf{K}_{II} & \mathbf{K}_{IB} \\ {\mathbf{K}_{IB}}^{\mathrm{T}} & \mathbf{K}_{BB} \end{bmatrix} \begin{Bmatrix} {\delta\mathbf{a}_I}^{(j)} \\ {\delta\mathbf{a}_B}^{(j)} \end{Bmatrix} \tag{76}$$

and

$$\mathbf{S}\delta\mathbf{a}^{(j)} = \begin{bmatrix} \mathbf{S}_I & \mathbf{S}_B \end{bmatrix} \begin{Bmatrix} {\delta\mathbf{a}_I}^{(j)} \\ {\delta\mathbf{a}_B}^{(j)} \end{Bmatrix} \tag{77}$$

$$\mathbf{r_a}^{(j)} = \left\langle \begin{array}{cc} \mathbf{r_{a_I}}^{(j)} & \mathbf{r_{a_B}}^{(j)} \end{array} \right\rangle^{\mathrm{T}} \tag{78}$$

where:

- Subscript I denotes the components associated with the interior nodes, which are entirely within the RVE domain.
- Subscript B denotes the components associated with the boundary nodes, where the constraints are imposed.

Boundary Integral Contributions: The matrix $\mathbf{S}$, which enforces the boundary constraints, is defined solely through boundary integrals:

$$\mathbf{S} = \int_{S_{RVE}} \mathbf{G}^{\mathrm{T}} \mathbf{A} \, \mathrm{d}\Psi. \tag{79}$$

As a result, $\mathbf{S}_I = 0$, since $\mathbf{G}$ vanishes at interior nodes ($\mathbf{y} \in \bar{V}_{RVE} \setminus S_{RVE}$). This simplifies the application of boundary conditions, as interior nodes are not directly affected by $\mathbf{S}$.

Residual Partitioning: The residual vector $\mathbf{r}_{\mathbf{a}}^{(j)}$ is partitioned into:

$$\mathbf{r}_{\mathbf{a}}^{(j)} = \begin{Bmatrix} \mathbf{r}_{\mathbf{a}_I}^{(j)} \\ \mathbf{r}_{\mathbf{a}_B}^{(j)} \end{Bmatrix}, \tag{80}$$

where:

- $\mathbf{r}_{\mathbf{a}_I}^{(j)}$: Residual at the interior nodes, determined by equilibrium equations.
- $\mathbf{r}_{\mathbf{a}_B}^{(j)}$: Residual at the boundary nodes, influenced by boundary constraints.

Physical Significance: The partitioning distinguishes the roles of the interior and boundary nodes:

- Interior nodes respond to the equilibrium conditions within the RVE domain. Their displacements are updated based on the residual correction $\delta \mathbf{a}_{\mathbf{r}}^{(j)}$.

- Boundary nodes enforce the prescribed boundary conditions (e.g., displacement, traction, or periodic constraints) using Lagrange multipliers $\boldsymbol{\lambda}$. The constraint corrections $\delta \mathbf{a}_{\mathbf{p}}^{(j)}$ are applied to these nodes.

Simplification through Partitioning: By isolating the boundary contributions, the second row of the global system of equations explicitly handles the Lagrange multiplier increments, while the first row governs the equilibrium conditions at the interior nodes. This structured approach enables efficient computation and simplifies the iterative solution procedure.

In summary, the partitioning into interior and boundary nodes is a fundamental step in the Newton-Raphson framework, ensuring that equilibrium and boundary constraints are treated systematically. The distinction between $\mathbf{K}_{II}$, $\mathbf{K}_{IB}$, $\mathbf{K}_{BB}$, and $\mathbf{S}_B$ allows for the efficient imposition of boundary conditions while maintaining consistency within the RVE formulation.

3.7.3 Displacement Boundary Condition

In the case of uniform displacement gradient boundary conditions are applied to the RVE. The displacement gradient (strain) is uniform across the RVE boundaries. No micro-scale displacement fluctuations are assumed at the boundaries. Mathematically, this is expressed as:

$$\boldsymbol{u}'(\Psi) = \mathbf{0} \tag{81}$$

Where $\boldsymbol{u}'(\Psi)$ denotes the micro-scale displacement fluctuations at the boundary points Ψ. The displacement at any point on the RVE boundary is determined solely by the macroscopic displacement gradient. There are no additional micro-scale variations at the boundary.

The original displacement expression is:

$$\boldsymbol{u}(\Psi) = \boldsymbol{u}^*(\bar{y}) + (\Psi - \bar{y})\bar{\mathbf{g}} + \boldsymbol{u}'(\Psi) \tag{82}$$

Where:

- $\boldsymbol{u}(\Psi)$: Displacement at point Ψ on the boundary S_{RVE}.

- $\boldsymbol{u}^*(\bar{y})$: Average displacement at the center $\bar{y}$ of the RVE.
- $\Psi - \bar{y}$: Position vector from the RVE center to the boundary point.
- $\bar{\mathbf{g}} = \frac{\partial \boldsymbol{u}^*}{\partial \boldsymbol{x}}$: Specified average displacement gradient field (macroscopic strain).
- $\boldsymbol{u}'(\Psi)$: Contribution from micro-fluctuations at the boundary.

Making some assumptions for simplification: Set the RVE center at the origin: $\bar{y} = 0$. Assume zero average displacement at the RVE center: $\boldsymbol{u}^*(\bar{y}) = 0$. No micro-fluctuations at the boundary: $\boldsymbol{u}'(\Psi) = 0$.

With these assumptions, the displacement simplifies to:

$$\boldsymbol{u}(\Psi) = \Psi \bar{\mathbf{g}} \tag{83}$$

The displacement at each boundary point is given by the product of its position vector Ψ and the macroscopic displacement gradient $\bar{\mathbf{g}}$.

For determining the Nodal Displacements at the Boundary, the equation for boundary displacements is:

$$\boldsymbol{\Lambda}_B = \Psi^T \bar{\mathbf{g}} \tag{84}$$

Where:

- $\boldsymbol{\Lambda}_B$: Vector of nodal displacements at the boundary nodes B.
- Ψ^T: Transpose of the matrix of boundary node position vectors.
- $\bar{\mathbf{g}}$: Macroscopic displacement gradient tensor.

For each boundary node k, the displacement is:

$$\boldsymbol{\Lambda}_{B_k} = \Psi_k^T \boldsymbol{g} \tag{85}$$

Where Ψ_k is the position vector of the k-th boundary node, and $\boldsymbol{\Lambda}_{B_k}$ is the displacement vector at the k-th boundary node.

The vector of approximation functions $\boldsymbol{A}$ for the displacement field is assumed to have the interpolatory property.

Interpolatory Property:

$$\boldsymbol{u}_k = \boldsymbol{A}_k \boldsymbol{a} \tag{86}$$

Where:

- $\boldsymbol{u}_k$: Displacement at node k.
- $\boldsymbol{A}_k$: Shape function evaluated at node k.
- $\boldsymbol{a}$: Vector of nodal displacement parameters.

Nodal Displacement Vector at Boundary Node k:

$$\boldsymbol{a}_{B_k} = \boldsymbol{\Lambda}_{B_k}^T = \begin{bmatrix} u_{B1}(\Psi_k) \\ u_{B2}(\Psi_k) \end{bmatrix} \tag{87}$$

Where $\boldsymbol{a}_{B_k}$ is the nodal displacement vector at boundary node k, and $u_{B1}(\Psi_k)$, $u_{B2}(\Psi_k)$ are the displacement components in the horizontal and vertical directions at boundary node k, respectively.

The total boundary displacement vector is:

$$\boldsymbol{a}_B = \begin{bmatrix} \boldsymbol{a}_{B1} & \boldsymbol{a}_{B2} & \cdots & \boldsymbol{a}_{Bk} & \cdots & \boldsymbol{a}_{Bm} \end{bmatrix} \tag{88}$$

Where m is the number of boundary nodes and $\boldsymbol{a}_{Bk}$ is the nodal displacement vector at the k-th boundary node.

The application of a uniform displacement gradient to the boundary of the RVE is a common approach in computational homogenization, simulating the material's response under macroscopically uniform deformation. This boundary condition simplifies the global system by directly prescribing the displacements at the boundary nodes.

By substituting Eq. (85) into Eq. (77), the equilibrium equations governing the displacement

field will be given by:

$$\begin{bmatrix} \mathbf{K}_{II} & \mathbf{S}_I{}^{\mathrm{T}} \\ \mathbf{S}_I & 0 \end{bmatrix} \begin{Bmatrix} \delta \mathbf{a}_I{}^{(j)} \\ \delta \mathbf{h}^{(j)} \end{Bmatrix} = \begin{Bmatrix} -\mathbf{K}_{IB} \boldsymbol{\psi}^{\mathrm{T}} \Delta \bar{\mathbf{g}} - \mathbf{r}_{\mathbf{a}_I}{}^{(j)} \\ \left(\boldsymbol{\Theta} - \mathbf{S}_B \boldsymbol{\psi}^{\mathrm{T}} \right) \Delta \bar{\mathbf{g}} - \mathbf{r}_{\mathbf{h}}^{(j)} \end{Bmatrix}. \tag{89}$$

This system couples the displacement increments $\delta \mathbf{a}_I^{(j)}$ with the Lagrange multiplier updates $\delta \mathbf{h}^{(j)}$, ensuring compatibility of internal and boundary constraints.

Prescribed Boundary Displacements: For uniform displacement boundary conditions, the displacement increments at the boundary nodes are directly imposed as:

$$\Delta \mathbf{a}_B = \boldsymbol{\psi}^{\mathrm{T}} \Delta \bar{\mathbf{g}}, \tag{90}$$

where:

- $\Delta \bar{\mathbf{g}}$ is the macroscopic strain increment,
- $\boldsymbol{\psi}^{\mathrm{T}}$ is the operator mapping the macroscopic strain increment to the boundary displacements,
- $\Delta \mathbf{a}_B$ represents the total displacement increment at the boundary nodes.

By directly prescribing $\Delta \mathbf{a}_B$, the boundary displacements are no longer unknowns, simplifying the system of equations.

Internal Node Displacements: Since $\mathbf{S}_I = 0$, the system in Eq. (89) simplifies, and the equilibrium equations for the interior nodes reduce to:

$$\mathbf{K}_{II} \delta \mathbf{a}_I^{(j)} = -\mathbf{K}_{IB} \boldsymbol{\psi}^{\mathrm{T}} \Delta \bar{\mathbf{g}} - \mathbf{r}_{\mathbf{a}_I}^{(j)}, \tag{91}$$

where:

- $\delta \mathbf{a}_I^{(j)}$ is the incremental displacement correction for the interior nodes,
- $\mathbf{K}_{II}$ and $\mathbf{K}_{IB}$ are the partitioned stiffness matrix components,

- $\mathbf{r}_{\mathbf{a}_I}^{(j)}$ is the residual at the interior nodes.

The displacement increment at the interior nodes is decomposed into two components:

$$\delta\mathbf{a}_I^{(j)} = \delta\mathbf{a}_{I,r}^{(j)} + \delta\mathbf{a}_{I,p}^{(j)}, \tag{92}$$

where:

- $\delta\mathbf{a}_{I,r}^{(j)} = -\mathbf{K}_{II}^{-1}\mathbf{r}_{\mathbf{a}_I}^{(j)}$: residual correction, addressing the imbalance at iteration (j),
- $\delta\mathbf{a}_{I,p}^{(j)} = -\mathbf{K}_{II}^{-1}\mathbf{K}_{IB}\boldsymbol{\psi}^{\mathrm{T}}\Delta\bar{\mathbf{g}}$: constraint correction, enforcing the prescribed boundary displacements.

Residual Simplifications: Since $\mathbf{S}_I = 0$, the second row of Eq. (89) is identically satisfied, eliminating the need for updating the Lagrange multiplier field $\mathbf{h}$. This simplification further streamlines the solution process.

Iterative Updates: The total displacement increments at the interior nodes are updated iteratively as:

$$\Delta\mathbf{a}_I = \Delta\mathbf{a}_{I,r} + \Delta\mathbf{a}_{I,p}. \tag{93}$$

These updates continue until the residuals at the interior nodes satisfy the convergence criterion:

$$\|\mathbf{r}_{\mathbf{a}_I}^{(j)}\| \leq \epsilon. \tag{94}$$

By directly prescribing the boundary node displacements via Eq. (90), the computational complexity is reduced by removing the Lagrange multiplier updates. This approach ensures numerical efficiency while maintaining the accuracy of the solution.

3.7.4 Traction Boundary Condition

The objective is to implement uniform traction boundary conditions on a RVE under the assumption of uniform stress. However, a challenge arises because the point-wise boundary displacements

cannot be directly prescribed, as micro-scale displacement fluctuations at the boundary are generally non-zero, expressed as $\boldsymbol{u}'(\psi) \neq 0$. To maintain uniform boundary stress, the goal is to impose the same value for the boundary stress (traction) at every boundary node.

To impose uniform traction, we express the Lagrange multiplier vector $\boldsymbol{h}$ in terms of a reduced set of unknowns:

$$\boldsymbol{h} = \boldsymbol{H}^T \boldsymbol{r} \tag{95}$$

Where:

- $\boldsymbol{h}$: Vector of Lagrange multiplier parameters associated with the boundary nodes.
- $\boldsymbol{H}$: A mapping matrix that distributes the unknowns uniformly across the boundary nodes.
- $\boldsymbol{r}$: A vector containing two unknowns, one for each spatial direction (e.g., x and y).

$$\boldsymbol{r} = \begin{bmatrix} r_1 \\ r_2 \end{bmatrix} \tag{96}$$

Where:

- r_1: Unknown representing the uniform traction in the x-direction.
- r_2: Unknown representing the uniform traction in the y-direction.

$$\boldsymbol{H} = \begin{bmatrix} 1 & 0 & 1 & 0 & \cdots & -1 & 0 & -1 & 0 \\ 0 & 1 & 0 & 1 & \cdots & 0 & -1 & 0 & -1 \end{bmatrix} \tag{97}$$

Each column in the matrix corresponds to a degree of freedom (DOF) at a boundary node, representing either the x or y displacement component, with positive and negative signs indicating nodes that are mirrored on opposite boundaries of the RVE. The purpose of the matrix $\boldsymbol{H}$ is to ensure that uniform traction is applied across all boundary nodes while maintaining equilibrium, ensuring that the net force aligns with the macroscopic stress.

The application of uniform traction boundary conditions enables the simulation of material behaviour under prescribed boundary forces, providing a realistic representation of external loading

on the Representative Volume Element (RVE). This approach directly enforces boundary tractions, allowing the internal displacements and Lagrange multipliers to be solved iteratively.

By substituting Eq. (95) into Eq. (66) and using Eqs. (76) and (77), the global system of equations in the Newton-Raphson framework will be expressed as:

$$\begin{bmatrix} \mathbf{K}_{II} & \mathbf{K}_{IB} & \mathbf{0} \\ \mathbf{K}_{IB}^{\mathrm{T}} & \mathbf{K}_{BB} & \mathbf{S}_B^{\mathrm{T}}\mathbf{H}^{\mathrm{T}} \\ \mathbf{0} & \mathbf{H}\mathbf{S}_B & \mathbf{0} \end{bmatrix} \begin{Bmatrix} \delta\mathbf{a}_I^{(j)} \\ \delta\mathbf{a}_B^{(j)} \\ \delta\mathbf{q}^{(j)} \end{Bmatrix} = \begin{Bmatrix} -\mathbf{r}_{\mathbf{a}_I}^{(j)} \\ -\mathbf{r}_{\mathbf{a}_B}^{(j)} \\ \mathbf{H}\boldsymbol{\Theta}\Delta\bar{\mathbf{g}} - \mathbf{r}_{\mathbf{h}}^{(j)} \end{Bmatrix}, \tag{98}$$

where:

- $\mathbf{K}_{(\cdot)(\cdot)}$ are the components of the stiffness matrix partitioned into internal (I) and boundary (B) nodes,
- $\mathbf{S}_B$ enforces boundary constraints through Lagrange multipliers,
- $\mathbf{H}$ maps the Lagrange multipliers to the boundary tractions,
- $\delta\mathbf{q}^{(j)}$ is the auxiliary variable used to enforce the traction boundary conditions,
- $\mathbf{r}_{\mathbf{a}_I}^{(j)}$ and $\mathbf{r}_{\mathbf{a}_B}^{(j)}$ are the residuals at the interior and boundary nodes, respectively.

Auxiliary Variable $\delta\mathbf{q}^{(j)}$: The auxiliary variable $\delta\mathbf{q}^{(j)}$ is introduced to enforce the traction boundary conditions. It is computed iteratively as:

$$\delta\mathbf{q}^{(j)} = -\left[\mathbf{H}\mathbf{S}_B\mathbf{K}_{BB}^{-1}\mathbf{S}_B^{\mathrm{T}}\mathbf{H}^{\mathrm{T}}\right]^{-1}\left[\mathbf{H}\boldsymbol{\Theta}\Delta\bar{\mathbf{g}} - \mathbf{r}_{\mathbf{h}}^{(j)} - \mathbf{H}\mathbf{S}_B\delta\mathbf{a}_{B,r}^{(j)}\right], \tag{99}$$

where:

- $\delta\mathbf{a}_{B,r}^{(j)}$ is the residual-based correction for boundary displacements, computed as part of the displacement decomposition.

Iterative Steps: The solution procedure under traction boundary conditions follows a systematic sequence:

(1) Compute the residual-based displacement corrections:

$$\begin{Bmatrix} \delta\mathbf{a}_{I,r}^{(j)} \\ \delta\mathbf{a}_{B,r}^{(j)} \end{Bmatrix} = - \begin{bmatrix} \mathbf{K}_{II} & \mathbf{K}_{IB} \\ \mathbf{K}_{IB}^{\mathrm{T}} & \mathbf{K}_{BB} \end{bmatrix}^{-1} \begin{Bmatrix} \mathbf{r}_{\mathbf{a}_I}^{(j)} \\ \mathbf{r}_{\mathbf{a}_B}^{(j)} \end{Bmatrix}. \tag{100}$$

(2) Solve for the auxiliary variable $\delta\mathbf{q}^{(j)}$ using Eq. (99).

(3) Compute the constraint correction for boundary displacements:

$$\delta\mathbf{a}_p^{(j)} = -\mathbf{K}^{-1}\mathbf{S}_B^{\mathrm{T}}\mathbf{H}^{\mathrm{T}}\delta\mathbf{q}^{(j)}. \tag{101}$$

(4) Update the total displacement increment:

$$\Delta\mathbf{a}^{(j)} = \Delta\mathbf{a}^{(j-1)} + \delta\mathbf{a}^{(j)}, \quad \delta\mathbf{a}^{(j)} = \delta\mathbf{a}_r^{(j)} + \delta\mathbf{a}_p^{(j)}. \tag{102}$$

(5) Recompute the residuals $\mathbf{r}_{\mathbf{a}}^{(j+1)}$ and $\mathbf{r}_{\mathbf{h}}^{(j+1)}$, and verify convergence.

Convergence Criteria: The iterative process is terminated when the residual norms satisfy the prescribed tolerances:

$$\|\mathbf{r}_{\mathbf{a}}^{(j)}\| \leq \epsilon, \quad \|\mathbf{r}_{\mathbf{h}}^{(j)}\| \leq \epsilon. \tag{103}$$

The traction boundary condition allows for the direct enforcement of uniform boundary tractions while iteratively solving for the corresponding nodal displacements. The inclusion of the auxiliary variable $\delta\mathbf{q}^{(j)}$ ensures the accurate imposition of traction constraints, while the decomposition of displacements simplifies the solution procedure. This approach provides a robust framework for simulating the response of RVEs under prescribed traction boundary conditions.

3.7.5 Periodic Boundary Condition

In computational homogenization using Representative Volume Elements (RVEs), periodic boundary conditions are crucial for accurately representing materials with periodic microstructures. The primary objective is to derive the algebraic equations governing the RVE under these conditions,

with a focus on the key equations, particularly the integral involving Lagrange multipliers and the periodicity constraints. One key assumption is that micro-scale displacement fluctuations at the boundary are non-zero, expressed as:

$$\boldsymbol{u}'(\psi) \neq 0 \tag{104}$$

where $\boldsymbol{u}'(\psi)$ represents the micro-scale displacement fluctuation at a boundary point ψ. Due to the periodic nature of the boundary, these fluctuations are identical at corresponding points on opposite boundaries, which is given by:

$$\boldsymbol{u}'(\psi^+) = \boldsymbol{u}'(\psi^-) \tag{105}$$

where ψ^+ and ψ^- denote corresponding points on opposite boundaries of the RVE. Consequently, the difference in micro-scale fluctuations between these corresponding boundary points is zero, as shown by:

$$\boldsymbol{u}'(\psi^+) - \boldsymbol{u}'(\psi^-) = 0 \tag{106}$$

The total displacement at a boundary point is given by:

$$\boldsymbol{u}(\psi) = \bar{\boldsymbol{u}}(\bar{y}) + (\psi - \bar{y})^T \bar{\mathbf{g}} + \boldsymbol{u}'(\psi) \tag{107}$$

Assuming that the RVE center is at the origin ($\bar{y} = 0$) and the average displacement at the center is zero ($\bar{\boldsymbol{u}}(\bar{y}) = 0$), this simplifies to:

$$\boldsymbol{u}(\psi) = \psi^T \bar{\mathbf{g}} + \boldsymbol{u}'(\psi) \tag{108}$$

The displacement difference across the boundary is expressed as:

$$\boldsymbol{u}(\psi^+) - \boldsymbol{u}(\psi^-) = (\psi^+)^T \bar{\mathbf{g}} + \boldsymbol{u}'(\psi^+) - \left[(\psi^-)^T \bar{\mathbf{g}} + \boldsymbol{u}'(\psi^-)\right] \tag{109}$$

$$= (\psi^+ - \psi^-)^T \bar{\mathbf{g}} + \left(\boldsymbol{u}'(\psi^+) - \boldsymbol{u}'(\psi^-)\right) \tag{110}$$

Since the micro-scale fluctuation difference is zero ($\boldsymbol{u}'(\psi^+) - \boldsymbol{u}'(\psi^-) = 0$), this reduces to:

$$\boldsymbol{u}(\psi^+) - \boldsymbol{u}(\psi^-) = (\psi^+ - \psi^-)^T \bar{\mathbf{g}} \tag{111}$$

This expresses the periodic displacement condition:

$$\mathbf{u}\left(\boldsymbol{\psi}_k^+\right) - \mathbf{u}\left(\boldsymbol{\psi}_k^-\right) = \left(\boldsymbol{\psi}_k^+ - \boldsymbol{\psi}_k^-\right)^{\mathrm{T}} \bar{\mathbf{g}}, \tag{112}$$

where k refers to the node number on the boundary. The tractions (Lagrange multipliers) on the boundary are anti-periodic, as shown by:

$$\boldsymbol{\lambda}^+ = -\boldsymbol{\lambda}^- \tag{113}$$

where $\boldsymbol{\lambda}^+$ and $\boldsymbol{\lambda}^-$ are the tractions at points ψ^+ and ψ^-, respectively. To reduce the number of degrees of freedom and enforce anti-periodicity, we express $\boldsymbol{h}$ as:

$$\boldsymbol{h} = \boldsymbol{P}^T \boldsymbol{w} \tag{114}$$

where $\boldsymbol{h}$ is the vector of Lagrange multiplier parameters at boundary nodes, $\boldsymbol{P}$ is a mapping matrix, and $\boldsymbol{w}$ is the vector of reduced Lagrange multiplier unknowns. The matrix $\boldsymbol{P}$ has the form:

$$\boldsymbol{P} = \begin{bmatrix} 1 & 0 & \cdots & 0 & -1 & 0 & \cdots & 0 \\ 0 & 1 & \cdots & 0 & 0 & -1 & \cdots & 0 \\ \vdots & \vdots & \ddots & \vdots & \vdots & \vdots & \ddots & \vdots \\ 0 & 0 & \cdots & 1 & 0 & 0 & \cdots & -1 \end{bmatrix} \tag{115}$$

where each row has only two non-zero entries, $+1$ and -1, corresponding to nodes that are images of each other on opposite boundaries.

The application of periodic boundary conditions ensures continuity of displacements and tractions across opposing boundaries of the Representative Volume Element (RVE). This approach is essential for simulating materials with periodic microstructures, as it enforces both displacement compatibility and stress equilibrium, providing a realistic representation of the material's response under periodic loading.

Physical Significance: Periodic boundary conditions establish a seamless transfer of displacements and tractions between opposite boundaries of the RVE. This is achieved by ensuring:

- **Displacement Compatibility:** The relative displacements between corresponding points on opposing boundaries are consistent with the macroscopic deformation.
- **Traction Continuity:** The tractions on opposing boundaries remain balanced, maintaining equilibrium across the RVE.

By substituting Eqs. (112) and (114) into Eq. (66) and using Eqs. (76) and (77), the global system of equations in the Newton-Raphson framework is expressed as:

$$\begin{bmatrix} \mathbf{K}_{II} & \mathbf{K}_{IB} & \mathbf{0} \\ \mathbf{K}_{IB}^{\mathrm{T}} & \mathbf{K}_{BB} & \mathbf{S}_B^{\mathrm{T}}\mathbf{P}^{\mathrm{T}} \\ \mathbf{0} & \mathbf{P}\mathbf{S}_B & \mathbf{0} \end{bmatrix} \begin{Bmatrix} \delta\mathbf{a}_I^{(j)} \\ \delta\mathbf{a}_B^{(j)} \\ \delta\mathbf{w}^{(j)} \end{Bmatrix} = \begin{Bmatrix} -\mathbf{r}_{\mathbf{a}_I}^{(j)} \\ -\mathbf{r}_{\mathbf{a}_B}^{(j)} \\ \mathbf{P}\boldsymbol{\Theta}\Delta\bar{\mathbf{g}} - \mathbf{r}_{\mathbf{h}}^{(j)} \end{Bmatrix}, \tag{116}$$

where:

- $\mathbf{P}$ is the periodicity constraint matrix, enforcing displacement compatibility between opposing boundaries,
- $\delta\mathbf{w}^{(j)}$ is the auxiliary variable associated with the periodicity constraints,
- $\mathbf{r}_{\mathbf{a}_I}^{(j)}$ and $\mathbf{r}_{\mathbf{a}_B}^{(j)}$ are the residuals at the interior and boundary nodes, respectively.

Periodic Displacement Compatibility: The displacement compatibility condition for periodic boundaries is given by:

$$\Delta\mathbf{u}(\mathbf{x}^+) - \Delta\mathbf{u}(\mathbf{x}^-) = \mathbf{P}\Delta\mathbf{a}_B, \tag{117}$$

where:

- $\mathbf{x}^+$ and $\mathbf{x}^-$ represent corresponding points on opposing boundaries,
- $\mathbf{P}$ maps the nodal displacements at the boundary to enforce periodicity.

Iterative Solution Procedure: The solution under periodic boundary conditions proceeds iteratively with the following steps:

(1) Compute the residual-based displacement corrections:

$$\begin{Bmatrix} \delta\mathbf{a}_{I,r}^{(j)} \\ \delta\mathbf{a}_{B,r}^{(j)} \end{Bmatrix} = - \begin{bmatrix} \mathbf{K}_{II} & \mathbf{K}_{IB} \\ \mathbf{K}_{IB}^{\mathrm{T}} & \mathbf{K}_{BB} \end{bmatrix}^{-1} \begin{Bmatrix} \mathbf{r}_{\mathbf{a}_I}^{(j)} \\ \mathbf{r}_{\mathbf{a}_B}^{(j)} \end{Bmatrix}. \tag{118}$$

(2) Solve for the auxiliary variable $\delta\mathbf{w}^{(j)}$:

$$\delta\mathbf{w}^{(j)} = - \left[\mathbf{P}\mathbf{S}_B\mathbf{K}_{BB}^{-1}\mathbf{S}_B^{\mathrm{T}}\mathbf{P}^{\mathrm{T}}\right]^{-1} \left[\mathbf{P}\boldsymbol{\Theta}\Delta\bar{\mathbf{g}} - \mathbf{r}_{\mathbf{h}}^{(j)} - \mathbf{P}\mathbf{S}_B\delta\mathbf{a}_{B,r}^{(j)}\right]. \tag{119}$$

(3) Compute the constraint correction for boundary displacements:

$$\delta\mathbf{a}_p^{(j)} = -\mathbf{K}^{-1}\mathbf{S}_B^{\mathrm{T}}\mathbf{P}^{\mathrm{T}}\delta\mathbf{w}^{(j)}. \tag{120}$$

(4) Update the total displacement increment:

$$\Delta\mathbf{a}^{(j)} = \Delta\mathbf{a}^{(j-1)} + \delta\mathbf{a}^{(j)}, \quad \delta\mathbf{a}^{(j)} = \delta\mathbf{a}_r^{(j)} + \delta\mathbf{a}_p^{(j)}. \tag{121}$$

(5) Recompute the residuals $\mathbf{r}_{\mathbf{a}}^{(j+1)}$ and $\mathbf{r}_{\mathbf{h}}^{(j+1)}$, and verify convergence.

Convergence Criteria: The iterative process continues until the residuals satisfy the convergence criteria:

$$\|\mathbf{r}_{\mathbf{a}}^{(j)}\| \leq \epsilon, \quad \|\mathbf{r}_{\mathbf{h}}^{(j)}\| \leq \epsilon, \tag{122}$$

where ϵ is the prescribed tolerance for convergence.

Periodic boundary conditions enforce displacement and traction continuity across opposing boundaries of the RVE. The auxiliary variable $\delta\mathbf{w}^{(j)}$ ensures the accurate imposition of periodicity constraints, while the iterative procedure guarantees convergence. This approach provides a robust framework for simulating the response of materials with periodic microstructures under

macroscopic loading.

3.7.6 Effect of Boundary Conditions on Homogenization Results

Boundary conditions significantly influence the results of the homogenization process:

- **Displacement Boundary Conditions**: Tend to over-constrain the RVE, possibly leading to stiffer effective properties due to restricted micro-fluctuations.
- **Traction Boundary Conditions**: Allow for boundary displacements to adjust, which may result in softer effective properties due to localized deformations.
- **Periodic Boundary Conditions**: Provide a balance by minimizing artificial boundary effects, often yielding effective properties that are more representative of the infinite medium.

Choosing appropriate boundary conditions depends on:

- The nature of the material and its microstructure.
- The scale separation between the RVE and the macroscopic structure.
- The specific loading conditions and constraints in the application.

By implementing displacement, traction, and periodic boundary conditions appropriately, we can ensure that the RVE response accurately reflects the macroscopic behaviour of heterogeneous materials. Each boundary condition type has its implications on the homogenization results, and careful consideration is required to select the most suitable one for a given problem. This section highlights the mathematical formulations and implementations of these boundary conditions, emphasizing their effects on the effective material properties obtained from computational homogenization.

3.7.7 Summary of Boundary Condition Implementations

The implementation of boundary conditions significantly influences the RVE's response and the homogenized material properties. Table 3.1 summarizes the key aspects of each boundary condition type.

Table 3.1: Summary of Boundary Condition Implementations

Boundary Condition	Displacement Fluctuations	Tractions	Applicability
Displacement BC	$\tilde{\mathbf{u}} = \mathbf{0}$ on S_{RVE}	N/A	Constrained boundaries
Traction BC	$\tilde{\mathbf{u}} \neq \mathbf{0}$ on S_{RVE}	Uniform	Free boundaries
Periodic BC	$\tilde{\mathbf{u}}^+ = \tilde{\mathbf{u}}^-$	$\boldsymbol{\lambda}^+ = -\boldsymbol{\lambda}^-$	Periodic materials

3.8 Traction Update Procedure at Integration Points of the Matrix-Inclusion Interfaces

3.8.1 Introduction to Traction Update Procedure

The accurate modelling of interfacial behaviour in matrix-inclusion systems is fundamental to computational mechanics, particularly when addressing heterogeneous materials under complex loading conditions. Interfaces between the matrix and inclusion exhibit distinct mechanical behaviours that significantly influence the overall response of the material system. Capturing these behaviours requires a robust computational framework capable of addressing the intricate interplay between displacement jumps, traction-separation laws, and evolving damage mechanisms.

Traction update procedures at integration points are a pivotal component in simulating the interaction at matrix-inclusion interfaces. These procedures enforce the constitutive relationships governing interface mechanics while maintaining consistency with thermodynamic principles, as established in [53], [54]. The cohesive zone model (CZM) provides a versatile framework for representing the nonlinear relationship between traction and displacement discontinuities, governed by strain energy potentials and damage evolution laws [53], [54]. This relationship evolves iteratively during simulations to reflect the changing damage state.

A comprehensive traction update procedure integrates fundamental concepts, including the internal strain energy potential, complementary energy potential, and constrained optimization frameworks [54]. The internal strain energy potential captures the stored energy at the interface due to displacement jumps and damage evolution, as described in Eq. (123). The complementary energy potential, introduced through a Legendre transformation, reformulates the problem to provide a robust mathematical foundation for nonlinear behaviour, as shown in Eq. (126). Additionally, constrained optimization techniques, such as the Kuhn-Tucker optimality conditions, ensure that

damage evolution is thermodynamically admissible and consistent with the damage control function [14].

The numerical implementation of the traction update procedure involves iterative algorithms, such as the closest-point projection method, to project trial traction states onto the admissible damage surface [21], [55]. These algorithms address the nonlinearities introduced by damage evolution, ensuring convergence within prescribed tolerances. The compliance matrix, $\mathbf{\Phi_d}$, plays a central role in this process, dynamically evolving with the damage state to govern the relationship between tractions and displacement jumps [54]. Its accurate representation is critical for maintaining numerical stability and physical realism.

In summary, the traction update procedure provides a systematic approach to capturing the nonlinear behaviour of matrix-inclusion interfaces. By integrating rigorous theoretical foundations, thermodynamic principles, and robust numerical strategies, this procedure enables precise simulation of interfacial mechanics. The subsequent subsections explore these key components in detail, elucidating the thermodynamic, mathematical, and computational principles underpinning their formulation and implementation.

3.8.2 Thermodynamic Considerations and Complementary Energy Framework for Interface Damage

The evolution of damage at matrix-inclusion interfaces is governed by thermodynamic principles and an optimization framework that together ensure energy conservation, dissipation consistency, and numerical stability. Following [53] and [54], the traction update problem in cohesive zone models (CZMs) is formulated as a constrained optimization problem analogous to plasticity. Stress states yielding a positive damage control function are inadmissible, while negative values correspond to the elastic domain. Damage initiates and evolves thermodynamically when the damage control function reaches zero.

Thermodynamic Foundations

The internal strain energy potential Ψ, representing stored energy due to displacement jumps $[\![\mathbf{u}]\!]$ and damage variable κ_d, is defined as:

$$\Psi([\![\mathbf{u}]\!], \kappa_d) = \frac{1}{2}[\![\mathbf{u}]\!]^{\mathrm{T}} {\mathbf{\Phi_d}}^{-1} [\![\mathbf{u}]\!] + \frac{1}{2} H_d \kappa_d^2, \tag{123}$$

where $\mathbf{\Phi_d}$ is the compliance matrix reflecting the current damage state, and H_d is the hardening modulus. The traction vector $\mathbf{t}$ is derived as:

$$\mathbf{t} = \frac{\partial \Psi}{\partial [\![\mathbf{u}]\!]}. \tag{124}$$

To transition to tractions as primary variables, the complementary energy potential χ_d is introduced via Legendre transformation:

$$\chi_d(\mathbf{t}, \kappa_d) = \mathbf{t}^{\mathrm{T}} [\![\mathbf{u}]\!] - \Psi([\![\mathbf{u}]\!], \kappa_d). \tag{125}$$

Substituting Eqs. (124), and (123) into Eq. (125) yields:

$$\chi_d(\mathbf{t}, \kappa_d) = \frac{1}{2}\mathbf{t}^{\mathrm{T}} \mathbf{\Phi_d} \mathbf{t} - \frac{1}{2} H_d \kappa_d^2. \tag{126}$$

The displacement jump is then obtained as:

$$[\![\mathbf{u}]\!] = \frac{\partial \chi_d}{\partial \mathbf{t}} = \mathbf{\Phi_d} \mathbf{t}. \tag{127}$$

Damage Dissipation and Optimization

The second law of thermodynamics enforces non-negativity of the damage dissipation rate:

$$d\Omega_d = \frac{1}{2}\mathbf{t}^{\mathrm{T}} d\mathbf{\Phi_d} \mathbf{t} - H_d \kappa_d d\kappa_d \geq 0. \tag{128}$$

A damage control function F_d constrains the traction state:

$$F_d(\mathbf{t}, \kappa_d) = \|\mathbf{t}\| - \left(t_{\text{lim}} - \int H_d d\kappa_d \right) \leq 0, \tag{129}$$

where t_{lim} is the traction limit. The Kuhn-Tucker conditions ensure consistency:

$$d\Lambda_d \geq 0, \quad F_d \leq 0, \quad d\Lambda_d F_d = 0, \tag{130}$$

with $d\Lambda_d$ as the Lagrange multiplier.

To enforce these constraints, the Lagrangian functional is defined:

$$dL = d\Omega_d - d\Lambda_d F_d. \tag{131}$$

Variations of dL with respect to $\mathbf{t}$ and κ_d yield the governing equations:

$$d\mathbf{\Phi_d t} = d\Lambda_d \mathbf{m}_d, \tag{132}$$

$$d\Lambda_d = d\kappa_d. \tag{133}$$

Framework Integration

This unified framework rigorously links thermodynamics with optimization principles. The strain energy potential and complementary energy formulation establish a bidirectional relationship between tractions and displacement jumps. The dissipation inequality and damage control function ensure thermodynamic admissibility, while the Lagrangian approach provides numerical stability. By satisfying the Kuhn-Tucker conditions, the model prevents damage evolution in the elastic domain ($F_d < 0$) and enforces progression only at the admissible boundary ($F_d = 0$).

The integration of these components enables accurate simulation of matrix-inclusion interface behaviour under evolving damage, balancing physical realism with computational robustness. The derivations form the cornerstone of the traction update procedure, essential for predicting interface debonding and composite failure.

3.8.3 Consistency and Kuhn-Tucker Conditions

The consistency condition and Kuhn-Tucker optimality framework are fundamental to enforcing the admissibility of damage evolution in matrix-inclusion interface behaviour. These conditions ensure that the tractions remain on the boundary of the admissible domain defined by the damage control function, thereby preventing violations of physical or numerical constraints. Following the works of [53] and [54], the evolution of damage is governed by the damage control function F_d, which is expressed as:

$$F_d(\mathbf{t}, \kappa_d) = \|\mathbf{t}\| - \left(t_{\text{lim}} - \int H_d d\kappa_d\right) \leq 0, \tag{134}$$

During damage evolution, the consistency condition requires that the value of the damage control function remains zero. The incremental form of this condition is expressed as:

$$dF_d = \frac{\partial F_d}{\partial \mathbf{t}}^{\mathrm{T}} d\mathbf{t} + \frac{\partial F_d}{\partial \kappa_d} d\kappa_d = 0, \tag{135}$$

where $\frac{\partial F_d}{\partial \mathbf{t}}$ is the gradient of the damage control function with respect to the traction vector, and $\frac{\partial F_d}{\partial \kappa_d}$ represents the sensitivity of the damage surface to the hardening variable κ_d. This condition ensures that the tractions remain on the damage surface throughout the damage evolution process. The first term in Eq. (135) ensures that the traction state is consistent with the damage surface, while the second term governs the evolution of the damage variable.

The proportionality factor $d\Lambda_d$ plays a critical role in this framework, dictating the rate of damage progression. It is updated iteratively during the simulation and is always non-negative, ensuring the irreversibility of damage evolution. When $F_d < 0$, $d\Lambda_d = 0$, indicating that no damage increment occurs in the elastic domain.

The consistency condition is integral to the numerical implementation of the traction update procedure, particularly in iterative algorithms such as the closest-point projection method. By maintaining $dF_d = 0$ during damage evolution, the consistency condition ensures convergence and numerical stability. This iterative process involves projecting the trial traction vector onto the admissible damage surface, ensuring that the updated traction state adheres to the thermodynamic principles and the damage control function.

In summary, the consistency condition and Kuhn-Tucker framework provide a rigorous mathematical foundation for enforcing the admissibility of damage evolution. By ensuring that the tractions remain on the damage surface and that damage progression is thermodynamically consistent, these principles enable the accurate simulation of matrix-inclusion interface behaviour under complex loading conditions.

3.8.4 Numerical Algorithm for Traction Update and Compliance Evolution

The numerical implementation of the traction update procedure and compliance evolution forms the cornerstone for modelling matrix-inclusion interface behaviour under damage evolution. This algorithm ensures thermodynamic consistency while maintaining numerical stability through closest-point projection of trial tractions onto the admissible damage surface. The coupled framework integrates traction updates with dynamic compliance matrix adjustments to reflect evolving interface stiffness.

Traction Update Procedure

The procedure begins with the trial traction vector computed from the displacement jump at global iteration (j):

$$\mathbf{t}^{\text{trial}} = {\boldsymbol{\Phi}_{\mathbf{d}_{\text{tr}}}}^{-1} [\![\mathbf{u}]\!]^{(j)}, \tag{136}$$

where $\boldsymbol{\Phi}_{\mathbf{d}_{\text{tr}}}$ denotes the compliance matrix from the previous iteration. The displacement jump update at global iteration (j) follows:

$$[\![\mathbf{u}]\!]^{(j)} = [\![\mathbf{u}]\!]^{(j-1)} + \Delta[\![\mathbf{u}]\!]^{(j)}. \tag{137}$$

The damage control function $F_d(\mathbf{t}^{\text{trial}}, \kappa_d)$ determines admissibility: if $F_d \leq 0$, the trial traction is accepted. Otherwise, a local iterative correction projects $\mathbf{t}^{\text{trial}}$ onto the damage surface through:

$$\mathbf{t}^{(k)} = \mathbf{t}^{(k-1)} - \delta \boldsymbol{t}^{(k)}, \tag{138}$$

with the traction correction increment:

$$\delta \boldsymbol{t}^{(k)} = \delta \Lambda_d^{(k)} {\boldsymbol{\Phi}_{\mathbf{d}_{\text{tr}}}}^{-1} \mathbf{m}_d^{(k)}. \tag{139}$$

The flow direction vector $\mathbf{m}_d$ for non-associative laws derives from:

$$\mathbf{m}_d = \frac{\partial G_d}{\partial \mathbf{t}}, \tag{140}$$

where G_d represents the damage potential surface. This generalization accommodates complex interface behaviours documented in [20], [21], [55].

The proportionality factor $\delta \Lambda_d^{(k)}$ follows from linearisation of the damage consistency condition:

$$\delta \Lambda_d^{(k)} = \frac{F_d^{(k)} - \mathbf{n}_d^{(k)\mathrm{T}} \mathbf{R}_d^{(k)} \boldsymbol{\Phi}_{\mathbf{d}_{\text{tr}}} \mathbf{r}_d^{(k)}}{\mathbf{n}_d^{(k)\mathrm{T}} \mathbf{R}_d^{(k)} \mathbf{m}_d^{(k)} + H_d}, \tag{141}$$

where the residual vector components are:

$$\mathbf{r}_d^{(k)} = \mathbf{t}^{(k)} - \mathbf{t}^{\text{trial}} + \Delta \mathbf{t}^{(k)}, \tag{142}$$

$$\Delta \mathbf{t}^{(k)} = \Delta \Lambda_d^{(k)} {\boldsymbol{\Phi}_{\mathbf{d}_{\text{tr}}}}^{-1} \mathbf{T} \mathbf{m}_d^{(k)}. \tag{143}$$

Convergence requires simultaneous satisfaction of:

$$|F_d^{(k)}| \leq \epsilon_{\text{tol}} \quad \text{and} \quad \|\mathbf{r}_d^{(k)}\| \leq \epsilon_{\text{tol}}, \tag{144}$$

with the hardening variable updating post-convergence as:

$$\kappa_d^{(k)} = \kappa_d^{(k-1)} + \delta \Lambda_d^{(k)}. \tag{145}$$

Compliance Matrix Formulation and Damage Coupling

The compliance matrix $\mathbf{\Phi_d}$ mediates traction-displacement jump relationships and evolves with damage. For anisotropic damage, following [54]:

$$\mathbf{\Phi_d}^{-1} = (\mathbf{I} - \mathbf{P}_d)\mathbf{T}, \quad \mathbf{T} = \begin{bmatrix} k_s & 0 \\ 0 & k_n \end{bmatrix}, \tag{146}$$

where $\mathbf{P}_d$ captures directional stiffness reduction:

$$\mathbf{P}_d = \frac{\mathbf{\Phi_{d_{tr}}}^{-1}\mathbf{m_d}\mathbf{n_d}^{\mathrm{T}}}{\mathbf{n_d}^{\mathrm{T}}\mathbf{\Phi_{d_{tr}}}^{-1}\mathbf{m_d} + \|\mathbf{t}\|/\delta\Lambda_d^{(k)}}. \tag{147}$$

Algorithmic Tangential Stiffness and Consistency

Post-convergence, the compliance matrix updates globally as:

$$\mathbf{\Phi_d} = \mathbf{\Phi_{d_{tr}}} + \delta\Lambda_d^{(k)} \frac{\mathbf{m_d}\mathbf{n_d}^{\mathrm{T}}}{\|\mathbf{t}\|}, \tag{148}$$

while the algorithmic tangent stiffness matrix ensures consistent linearisation:

$$\bar{\mathbf{C}}_\mathbf{d} = \mathbf{R_d}\left[\mathbf{I} - \frac{\mathbf{m_d}\mathbf{n_d}^{\mathrm{T}}\mathbf{R_d}}{\mathbf{n_d}^{\mathrm{T}}\mathbf{R_d}\mathbf{m_d} + H_d}\right], \quad \mathbf{R_d} = (\mathbf{\Phi_d}\mathbf{Q_d})^{-1}. \tag{149}$$

Here, $\mathbf{Q_d} = \mathbf{I} + \Delta\Lambda_d\mathbf{\Phi_d}^{-1}\mathbf{m_{d,t}}$ accounts for damage gradient effects. This operator reduces to the elastic compliance relation $\mathbf{t} = \mathbf{\Phi_d}^{-1}[\![\mathbf{u}]\!]$ when $\mathbf{Q_d} = \mathbf{I}$, maintaining consistency between incremental and total traction-displacement relationships.

Physical Admissibility and Unloading

Thermodynamic consistency requires $\mathbf{\Phi_d}$ updates to satisfy $\|F_d^{(k)}\| \leq \epsilon_{\text{tol}}$ and $\|\mathbf{r}_d^{(k)}\| \leq \epsilon_{\text{tol}}$. During unloading ($\delta\Lambda_d = 0$), $\mathbf{\Phi_d}$ remains constant, and $\bar{\mathbf{C}}_\mathbf{d} \equiv \mathbf{\Phi_d}^{-1}$, preventing spurious energy dissipation. This distinguishes damage from plasticity, with reversible compliance changes upon unloading.

The coupled algorithm provides a unified framework for modelling interface degradation, accommodating both anisotropic and isotropic damage evolution through consistent matrix updates. Numerical stability arises from the closest-point projection's contractive properties, while thermodynamic admissibility follows from enforcing $F_d \leq 0$ and associative compliance evolution [21], [55].

3.8.5 Traction-Separation Laws, Damage Surfaces, and Algorithmic Tangent Stiffness

Traction-separation laws establish the constitutive relationship between interface tractions and displacement jumps, capturing nonlinear behaviour during damage evolution. When integrated with damage surfaces and the algorithmic tangent stiffness matrix, they form a complete framework for modelling anisotropic/orthotropic interface behaviour while ensuring numerical stability.

Damage Surface Formulations

The primary damage surface govern interface failure:

$$F_d(\boldsymbol{t}, \kappa_d) = \begin{cases} t_s^2 - t_{s_{max}}^2 \leq 0 & \text{if } t_n \leq 0 \\ \frac{t_s^2}{t_{s_{max}}^2} + \frac{t_n^2}{t_{n_{max}}^2} - 1 \leq 0 & \text{if } t_n > 0 \end{cases} \tag{150}$$

where $t_s = \mathbf{s}^{\mathrm{T}}\mathbf{t}$ and $t_n = \mathbf{n}^{\mathrm{T}}\mathbf{t}$ are tangential/normal tractions, $t_{n_{\max}}$ is the maximum normal traction. Eq. (150) enables, with $G_d \equiv F_d$, for associative flow [55].

Algorithmic Tangent Stiffness Derivation

The tangent stiffness matrix $\bar{\mathbf{C}}_{\mathbf{d}}$ links traction and displacement increments:

$$\Delta\mathbf{t} = \bar{\mathbf{C}}_{\mathbf{d}}\Delta[\![\mathbf{u}]\!], \tag{151}$$

derived through consistent linearisation of the traction update of Eq. (149).

Numerical Implementation Aspects

Key implementation features ensure robustness:

- **Stability:** Convergence requires:

$$|F_d| \leq \text{tol}, \quad \|\mathbf{r}_d\| \leq \text{tol}, \tag{152}$$

  with residual $\mathbf{r}_d = \mathbf{t} - \mathbf{t}^{\text{trial}} + \Delta\mathbf{t}$.

- **Unloading Consistency:** When $d\Lambda_d = 0$,

$$\bar{\mathbf{C}}_\mathbf{d} = {\mathbf{\Phi}_\mathbf{d}}^{-1}, \tag{153}$$

  preventing permanent deformations.

- **Compliance Coupling:** $\bar{\mathbf{C}}_\mathbf{d}$ updates synchronously with $\mathbf{\Phi_d}$ to maintain physical consistency during damage evolution.

Computational Framework Synergy

The unified damage framework provides:

- **Physical Accuracy:** Mohr-Coulomb captures anisotropic friction effects, while the elliptical surface efficiently models orthotropic interactions.

- **Numerical Efficiency:** $\bar{\mathbf{C}}_\mathbf{d}$ enables quadratic convergence in Newton-Raphson iterations through exact linearisation.

- **Model Flexibility:** Modular implementation allows switching between damage surfaces without altering core algorithms.

This integrated approach, validated in [54], [55], successfully handles complex loading scenarios in matrix-inclusion systems while maintaining computational tractability.

3.9 Computation of Effective Material Properties

The computation of effective material properties from micro-scale simulations is a fundamental aspect of computational homogenization. This section explains the process of determining the homogenized constitutive relations by averaging the stress and strain fields over the Representative Volume Element (RVE) and identifies specific elastic constants. Additionally, the impact of micro-scale fluctuations on macro-scale properties is discussed.

3.9.1 Averaging Techniques for Stress and Strain

The effective (homogenized) material properties are obtained by averaging the local stress and strain fields over a specified domain within the RVE, often referred to as the Window of Interest (WOI). This averaging process is based on the assumption that the WOI is representative of the material's microstructure.

Averaging the Local Stress Field

The average stress tensor $\widehat{\boldsymbol{\sigma}}$ over the WOI Y_W is defined as:

$$\widehat{\boldsymbol{\sigma}} = \frac{1}{|Y_W|} \int_{Y_W} \boldsymbol{\sigma} \, dY, \tag{154}$$

where:

- $\boldsymbol{\sigma}$ is the local stress tensor at each point within the WOI, obtained from the constitutive relation.
- $|Y_W|$ is the volume (or area in 2D) of the WOI as shown in Figure 3.2, given by:

$$|Y_W| = \int_{Y_W} dY. \tag{155}$$

This integral effectively sums the local stress contributions over the WOI and normalizes them by the WOI's volume, providing an average stress that reflects the overall response of the microstructure within that region.

Averaging the Local Strain Field

Similarly, the average strain tensor $\hat{\boldsymbol{\epsilon}}$ over the WOI is calculated as:

$$\hat{\boldsymbol{\epsilon}} = \frac{1}{|Y_W|} \int_{Y_W} \boldsymbol{\epsilon} \, dY = \frac{1}{|Y_W|} \int_{Y_W} \frac{\partial \mathbf{u}}{\partial \mathbf{y}} \, dY, \tag{156}$$

where:

- $\boldsymbol{\epsilon}$ is the local strain tensor, obtained from the gradient of the displacement field $\mathbf{u}$ within the RVE.
- $\frac{\partial \mathbf{u}}{\partial \mathbf{y}}$ represents the displacement gradient with respect to the spatial coordinates $\mathbf{y}$.

The averaging of the strain field accounts for the deformation behaviour of the material's microstructure and provides an effective strain measure over the WOI.

Definition of the Window of Interest (WOI)

The WOI is a subdomain within the RVE, defined to focus on a specific region of interest, possibly to capture localized effects or to exclude boundary influences. Figure 3.2 illustrates the WOI within the RVE.

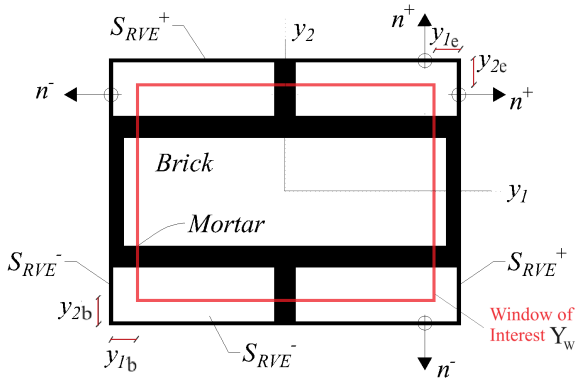

Figure 3.2: Schematic representation of the Window of Interest (WOI) within the RVE. Margins from the bottom-left corner are y_{1b} and y_{2b}, and from the top-right corner are y_{1e} and y_{2e}.

The margins of the WOI are defined by distances from the RVE boundaries:

- y_{1b} and y_{2b}: Distances from the bottom-left corner along the y_1 and y_2 axes, respectively.

- y_{1e} and y_{2e}: Distances from the top-right corner along the y_1 and y_2 axes, respectively.

By selecting an appropriate WOI, the averaging process can be tailored to specific regions, enhancing the accuracy of the effective property calculations.

3.9.2 Determination of Homogenized Constitutive Relations

The relationship between the averaged stress and strain tensors defines the effective (homogenized) constitutive behaviour of the material within the WOI.

Effective Constitutive Relationship

The homogenized stress-strain relationship is expressed as:

$$\widehat{\boldsymbol{\sigma}} = \widehat{\mathbf{D}}\,\widehat{\boldsymbol{\epsilon}}, \tag{157}$$

where $\widehat{\mathbf{D}}$ is the effective stiffness tensor (constitutive matrix) representing the material's response.

Calculating the Local Stress Tensor

The local stress tensor $\boldsymbol{\sigma}$ at each point within the RVE is obtained from the constitutive relation:

$$\boldsymbol{\sigma} = \mathbf{D}\,\boldsymbol{\epsilon}, \tag{158}$$

where $\mathbf{D}$ is the material stiffness matrix at the micro-scale, and $\boldsymbol{\epsilon}$ is the local strain tensor computed from the displacement field.

3.9.3 Identification of Elastic Constants

To extract specific elastic constants from the effective stiffness tensor, we apply particular loading scenarios that simplify the calculations.

Applying Specific Displacement Gradients

We consider three independent loading cases corresponding to uniaxial and shear deformations:

- **Case 1:** Apply a displacement gradient $\mathbf{g}^1$ corresponding to uniaxial strain in the y_1-direction.

$$\mathbf{g}^1 = \begin{bmatrix} 1 \\ 0 \\ 0 \end{bmatrix} \tag{159}$$

- **Case 2:** Apply a displacement gradient $\mathbf{g}^2$ corresponding to uniaxial strain in the y_2-direction.

$$\mathbf{g}^2 = \begin{bmatrix} 0 \\ 1 \\ 0 \end{bmatrix} \tag{160}$$

- **Case 3:** Apply a displacement gradient $\mathbf{g}^3$ corresponding to pure shear strain.

$$\mathbf{g}^3 = \begin{bmatrix} 0 \\ 0 \\ 1 \end{bmatrix} \tag{161}$$

Extracting Elastic Constants

Using the averaged values, we can express the components of the effective stiffness tensor $\widehat{\mathbf{D}}$ in matrix form:

$$\begin{bmatrix} \widehat{\sigma}_{11}^1 & \widehat{\sigma}_{11}^2 & \widehat{\sigma}_{11}^3 \\ \widehat{\sigma}_{22}^1 & \widehat{\sigma}_{22}^2 & \widehat{\sigma}_{22}^3 \\ \widehat{\sigma}_{12}^1 & \widehat{\sigma}_{12}^2 & \widehat{\sigma}_{12}^3 \end{bmatrix} = \begin{bmatrix} \widehat{D}_{1111} & \widehat{D}_{1122} & \widehat{D}_{1112} \\ \widehat{D}_{1122} & \widehat{D}_{2222} & \widehat{D}_{2212} \\ \widehat{D}_{1112} & \widehat{D}_{2212} & \widehat{D}_{1212} \end{bmatrix} \begin{bmatrix} \widehat{\epsilon}_{11}^1 & \widehat{\epsilon}_{11}^2 & \widehat{\epsilon}_{11}^3 \\ \widehat{\epsilon}_{22}^1 & \widehat{\epsilon}_{22}^2 & \widehat{\epsilon}_{22}^3 \\ \widehat{\gamma}_{12}^1 & \widehat{\gamma}_{12}^2 & \widehat{\gamma}_{12}^3 \end{bmatrix} \tag{162}$$

In this equation, $\widehat{\gamma}_{12} = 2\widehat{\epsilon}_{12}$, according to Voigt's notation for shear strain. By solving this system for each loading case, we can identify the individual components of $\widehat{\mathbf{D}}$, thereby extracting specific elastic constants such as Young's modulus, Poisson's ratio, and shear modulus. When the

window of interest covers the entire RVE ($Y_W = V_{RVE}$), the average strain tensor for each loading case equals the applied displacement gradient:

$$\widehat{\boldsymbol{\epsilon}}^i = \mathbf{g}^i, \quad i = 1, 2, 3 \tag{163}$$

This simplifies the determination of the effective stiffness matrix components, as the off-diagonal strain terms become negligible. Thus, we can determine the components of $\widehat{\mathbf{D}}$ column by column.

To extract elastic moduli for comparison purposes, we assume the material behaves as a plane-stress orthotropic material. Under this assumption, the effective stiffness matrix $\widehat{\mathbf{D}}$ takes the following form:

$$\widehat{\mathbf{D}} = \begin{bmatrix} \widehat{Q}_{11} & \widehat{Q}_{12} & 0 \\ \widehat{Q}_{21} & \widehat{Q}_{22} & 0 \\ 0 & 0 & \widehat{G} \end{bmatrix} \tag{164}$$

where $\widehat{Q}_{11}$, $\widehat{Q}_{22}$ are the effective stiffness components in the y_1 and y_2 directions, respectively, and $\widehat{G}$ is the effective shear modulus. The elastic moduli and Poisson's ratios can be extracted from the following relationships:

$$\widehat{Q}_{11} = \frac{\widehat{E}_1}{1 - \widehat{\nu}_{12}\widehat{\nu}_{21}} \tag{165}$$

$$\widehat{Q}_{12} = \frac{\widehat{\nu}_{12}\widehat{E}_2}{1 - \widehat{\nu}_{12}\widehat{\nu}_{21}} = \widehat{Q}_{21} = \frac{\widehat{\nu}_{21}\widehat{E}_1}{1 - \widehat{\nu}_{12}\widehat{\nu}_{21}} \tag{166}$$

$$\widehat{Q}_{22} = \frac{\widehat{E}_2}{1 - \widehat{\nu}_{12}\widehat{\nu}_{21}} \tag{167}$$

Here, $\widehat{E}_1$, $\widehat{E}_2$ are the Young's moduli in the y_1 and y_2 directions, respectively, and $\widehat{\nu}_{12}$ and $\widehat{\nu}_{21}$ are the Poisson ratios. In total, there are five material constants to be identified in Eq. (164), with four of them being independent due to the symmetry condition in Eq. (166). Due to material symmetry in orthotropic materials:

$$\widehat{Q}_{12} = \widehat{Q}_{21} \tag{168}$$

There are five material constants in total: $\widehat{E}_1$, $\widehat{E}_2$, $\widehat{\nu}_{12}$, $\widehat{\nu}_{21}$, and $\widehat{G}$. However, considering the symmetry condition ($\widehat{Q}_{12} = \widehat{Q}_{21}$), there are only four independent constants to determine.

In Loading Case 1 ($\mathbf{g}_1$), the dominant strain is $\widehat{\epsilon}^1_{11}$, while the negligible strains are $\widehat{\epsilon}^1_{22} \approx 0$ and $\widehat{\gamma}^1_{12} \approx 0$. The effective stress components are given by the following relations:

$$\widehat{\sigma}^1_{11} = \widehat{Q}_{11}\widehat{\epsilon}^1_{11} \tag{169}$$

$$\widehat{\sigma}^1_{22} = \widehat{Q}_{12}\widehat{\epsilon}^1_{11} \tag{170}$$

From these expressions, we can solve for $\widehat{Q}_{11}$ and $\widehat{Q}_{12}$. Similarly, in Loading Case 2 ($\mathbf{g}_2$), the dominant strain is $\widehat{\epsilon}^2_{22}$, with negligible strains $\widehat{\epsilon}^2_{11} \approx 0$ and $\widehat{\gamma}^2_{12} \approx 0$. The effective stress components are:

$$\widehat{\sigma}^2_{22} = \widehat{Q}_{22}\widehat{\epsilon}^2_{22} \tag{171}$$

$$\widehat{\sigma}^2_{11} = \widehat{Q}_{21}\widehat{\epsilon}^2_{22} \tag{172}$$

From these, we can solve for $\widehat{Q}_{22}$ and $\widehat{Q}_{21}$. Finally, in Loading Case 3 ($\mathbf{g}_3$), the dominant strain is $\widehat{\gamma}^3_{12}$, while the negligible strains are $\widehat{\epsilon}^3_{11} \approx 0$ and $\widehat{\epsilon}^3_{22} \approx 0$. The effective stress component is:

$$\widehat{\sigma}^3_{12} = \widehat{G}\widehat{\gamma}^3_{12} \tag{173}$$

From this, we can solve for $\widehat{G}$.

Chapter 4

Validation Case Studies

In this section, we validate the developed X-FEM-based computational homogenization strategy by comparing its results with established literature values for material matrix constants, specifically E_1, ν_1, E_2, ν_2, and G, as reported in [6], [5], and [10]. The comparisons are based on approximate average constants calculated from the RVE using our approach, detailed below.

4.1 Calculation of Average Material Constants

The determination of the average material constants is based on the application of different unit displacement gradient vectors to the RVE. A crucial refinement in this process is the incorporation of the window of interest (WOI), which allows for a more precise calculation of the macro-strain within the selected domain. This computed macro-strain is then systematically integrated into the effective modulus evaluation, ensuring a more accurate representation of the material behaviour. The following sections provide a detailed explanation of each calculation method.

1. **Average Elastic Modulus** E_1

   To calculate E_1, we apply a unit displacement gradient vector $\mathbf{g} = \langle 1, 0, 0 \rangle^{\mathrm{T}}$ to the RVE. The Poisson's ratio within the region of interest is computed as:

$$\nu_1 = \frac{\widehat{\sigma}^1{}_{22}}{\widehat{\sigma}^1{}_{11}} \tag{174}$$

Using this value, we estimate the average elasticity modulus in the horizontal direction as:

$$E_1 = \frac{\widehat{\sigma}^1{}_{11}}{\widehat{\epsilon}^1{}_{11}} \left(1 - \nu_1 \nu_1\right) \tag{175}$$

This calculation adopts the assumptions $\widehat{\epsilon}^1{}_{22}/\widehat{\epsilon}^1{}_{11} \approx \widehat{\gamma}^1{}_{12}/\widehat{\epsilon}^1{}_{11} \approx 0$ and $(1 - \nu_1\nu_1) \approx (1 - \nu_{12}\nu_{21})$ for simplification.

2. **Average Elastic Modulus** E_2

   For E_2, we apply a unit displacement gradient vector $\mathbf{g} = \langle 0, 1, 0 \rangle^{\mathrm{T}}$ to the RVE. The Poisson's ratio in this orientation is calculated as:

$$\nu_2 = \frac{\widehat{\sigma}^2{}_{11}}{\widehat{\sigma}^2{}_{22}} \tag{176}$$

   The vertical elasticity modulus is then given by:

$$E_2 = \frac{\widehat{\sigma}^2{}_{22}}{\widehat{\epsilon}^2{}_{22}} \left(1 - \nu_2 \nu_2\right) \tag{177}$$

   The assumptions used here are $\widehat{\epsilon}^2{}_{11}/\widehat{\epsilon}^2{}_{22} \approx \widehat{\gamma}^2{}_{12}/\widehat{\epsilon}^2{}_{22} \approx 0$ and $(1 - \nu_2\nu_2) \approx (1 - \nu_{12}\nu_{21})$.

3. **Average Shear Modulus** G

   The average shear modulus is determined by applying the unit displacement gradient vector $\mathbf{g} = \langle 0, 0, 1 \rangle^{\mathrm{T}}$. The shear modulus G within the region of interest is calculated as:

$$G = \frac{\widehat{\sigma}^3{}_{12}}{\widehat{\gamma}^3{}_{12}} \tag{178}$$

   This calculation assumes that $\widehat{\epsilon}^3{}_{11}/\widehat{\gamma}^3{}_{12} \approx \widehat{\epsilon}^3{}_{22}/\widehat{\gamma}^3{}_{12} \approx 0$.

4.2 Boundary Conditions and Assumptions

To impose a perfect bond in all cases, we use $k = 10 \times 10^6$ N/mm^3 in Eq. (63). This value is chosen as it ensures that any increase in interface stiffness beyond this level does not impact the homogenized properties. Unless otherwise specified, periodic boundary conditions are applied to

the RVE.

4.3 Window of Interest and Margins

Due to the inability to place inclusions on the edges of the RVE, a window of interest is defined within the RVE, excluding boundary margins, as shown in Fig. 3.2. This setup ensures that the average stresses and strains are calculated only within this defined window, following Eqs. (154) and (156). For consistency across all analyses, the margins defining the window of interest, $\mathrm{Y_W}$, are set identically as $y_{1\mathrm{b}} = y_{2\mathrm{b}} = y_{1\mathrm{e}} = y_{2\mathrm{e}} = 2.5$ mm (see Fig. 3.2). This margin selection aligns with the windowed regions used in the analyses of [6], [5], and [10], facilitating direct comparisons.

4.4 Case 1: Validation Against [6] Results

In this validation case, we compare the results of the developed X-FEM-based computational homogenization approach with the values reported by [6]. The goal is to assess the accuracy of our model in capturing the effective elastic properties of a masonry RVE. The RVE is composed of brick units (96 mm × 22 mm) embedded within 10 mm thick mortar layers, forming a total dimension of 111 mm × 69 mm. The specific material properties for brick and mortar are detailed in Table 4.1.

Mechanical Properties	Brick	Lime Mortar
Elasticity Modulus E_1 (MPa)	1545.35	309.12
Poisson's Ratio ν_1	0.117	0.10

Table 4.1: Material Properties of the Masonry Constituents [6]

(a) (b)

Figure 4.1: RVE dimensions and finite element mesh for the validation study

To validate the model, the homogenized elastic constants E_1 and G were calculated under different boundary conditions: displacement, periodic, and traction. This comparison focuses on the periodic boundary conditions, as they most closely represent the average response of the RVE and are thus ideal for comparative analysis. Table 4.2 shows the results obtained from our X-FEM model, alongside the values reported in [6].

E_1 (MPa)	X-FEM Model	935.34
	Reference Model [6]	887.47
	Experimental Values [6]	807.62
G (MPa)	X-FEM Model	299.23
	Reference Model [6]	474.80

Table 4.2: Comparison of Homogenized Elastic Moduli under Periodic Boundary Conditions

The values in Table 4.2 show a strong alignment between our X-FEM model and the reference and experimental values for E_1, confirming that our model accurately captures the elastic modulus in the horizontal direction. Specifically, the elasticity moduli obtained based on the displacement and traction boundary conditions are $E_1 = 954.56$ MPa and $E_1 = 916.12$ MPa, respectively, providing upper and lower bounds to $E_1 = 935.34$ MPa reported in Table 4.2, which was obtained based on the periodic boundary conditions. Similarly, the shear moduli G obtained based on the displacement and traction boundary conditions are $G = 307.52$ MPa and $G = 296.56$ MPa, respectively, again providing upper and lower bounds to $G = 299.23$ MPa reported in Table 4.2, which was obtained based on the periodic boundary conditions.

However, the shear modulus G calculated by the X-FEM model (299.23 MPa) is lower than that reported in the reference model (474.80 MPa). This discrepancy may be attributed to differences in modelling assumptions, boundary conditions, and micromechanical approaches, as discussed in detail below. It should be noted that we have used the suggested elasticity and shear moduli values from the reference [6], which suggest a negative Poisson's ratio. However, alternative shear modulus calculations can be found in [6], where the lowest value for the shear modulus is $G = 352.12$ MPa and the corresponding elasticity modulus is $E = 953.53$ MPa. These values are in closer agreement with our results.

4.4.1 Conclusion on Periodic Boundary Condition Suitability

The results for E_1 indicate that our model performs well in predicting elasticity modulus under various boundary conditions, with periodic boundary conditions offering a representative average that closely matches the reference model.

To match Bati et al. (1999) as closely as possible, using periodic boundary conditions would likely yield the most comparable results. Bati et al.'s work involves a periodic microstructure, where such boundary conditions ensure the RVE's response aligns well with the repeating unit's characteristics. Here's why periodic boundary conditions are ideal for this comparison:

- **Consistency with Periodicity in Microstructure:** Bati et al. modelled materials with inherent periodicity. By enforcing periodic boundary conditions, displacement fields on opposite boundaries are matched, mimicking the infinite repeat of the microstructure and minimizing artificial boundary effects.

- **Balanced Micro-Scale Fluctuations:** Unlike displacement or traction boundary conditions, periodic boundary conditions account for both micro- and macro-scale interactions effectively, which is essential for capturing accurate effective properties that match those from periodic microstructures.

- **Accurate Stiffness Representation:** Periodic boundary conditions provide a realistic representation of material stiffness without over- or under-constraining the system. This balance often leads to effective properties that closely match experimental or published values, such as those by Bati et al.

In summary, periodic boundary conditions are selected for validation because they provide a balanced response, minimize artificial boundary effects, and are more representative of the RVE's periodic microstructure, which is essential for capturing the true macroscopic behaviour of masonry materials as studied in [6].

4.4.2 The Influence of the RVE Size on the Homogenization

Understanding the impact of RVE size on the homogenized properties is crucial for ensuring the reliability of computational models in representing masonry materials. To investigate this, we analysed three different RVE sizes: 111×69 mm, 217×133 mm, and 323×197 mm, while maintaining a uniform mesh size of 3×3 mm. The configurations of these RVEs are illustrated in Figure 4.2.

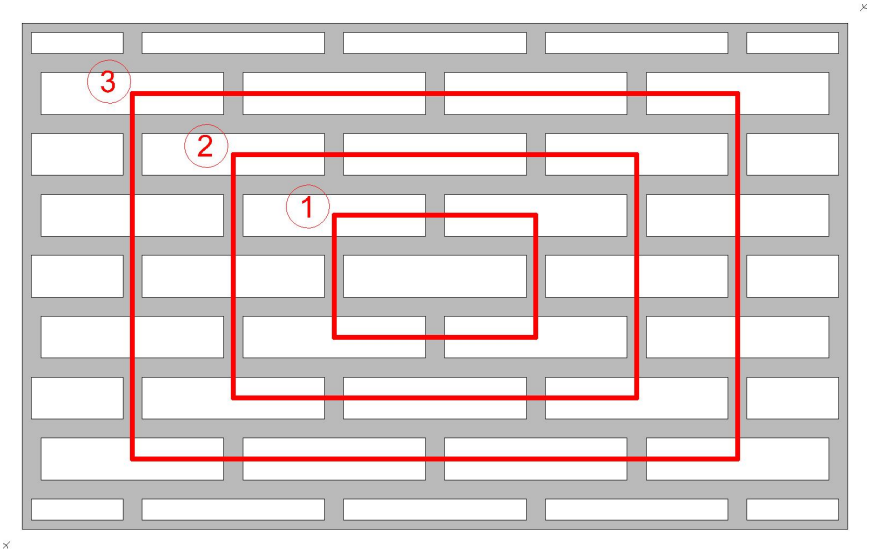

Figure 4.2: Configurations of the three RVE models with varying dimensions.

For each RVE size, the deformation gradient $\mathbf{g} = \langle 1, 0, 0 \rangle^{\mathrm{T}}$ was applied to compute the homogenized elasticity modulus E_1. The corresponding deformed shapes are shown in Figure 4.3, highlighting the response of the RVE models under the imposed boundary conditions.

The homogenized elasticity modulus E_1 and associated accuracy metrics for each RVE size are presented in Table 4.3. The results reveal a slight decrease in E_1 with increasing RVE size, indicating the influence of heterogeneities captured within larger RVEs.

Case	RVE Dimensions (mm × mm)	Number of Elements	Mesh Size (mm × mm)	E_1 (MPa)	Accuracy (%)
1	111×69	37×23	3×3	935.34	105.39
2	217×133	72×44	3×3	925.58	104.29
3	323×197	108×66	3×3	912.97	102.39

Table 4.3: Effect of RVE size on homogenized elasticity modulus E_1.

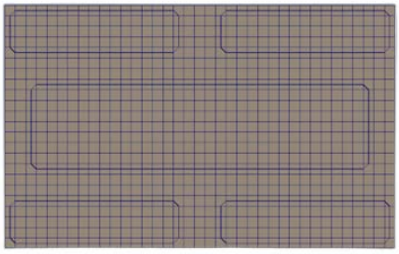

(a) RVE size: $111 \times 69\,\text{mm}$.

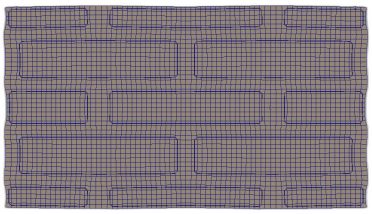

(b) RVE size: $217 \times 133\,\text{mm}$.

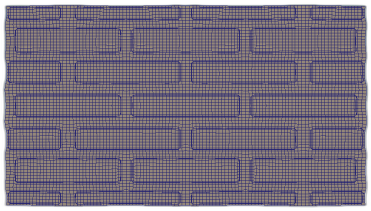

(c) RVE size: $323 \times 197\,\text{mm}$.

Figure 4.3: Deformed shapes of the three RVE models under $\mathbf{g} = \langle 1, 0, 0 \rangle^{\mathrm{T}}$.

Discussion

The observed trend, where E_1 decreases slightly with increasing RVE size, suggests that larger RVEs encompass more heterogeneities within the masonry microstructure. This leads to a reduction in the averaged stiffness values. The smallest RVE ($111 \times 69\,\text{mm}$) exhibits a slightly higher E_1, likely due to the limited representation of material heterogeneities within its smaller domain.

These findings emphasize the importance of selecting an RVE size that adequately represents the material's microstructure for accurate homogenization. While smaller RVEs may provide computational efficiency, larger RVEs are more representative of the actual masonry material, capturing its inherent variability and leading to more reliable predictions of macroscopic properties.

4.4.3 Factors Influencing Discrepancies with [6]

The difference between our results and those obtained by Bati et al. (1999) can likely be attributed to several factors related to modelling assumptions, material representations, and methodological choices:

- **modelling Assumptions and Simplifications:** Bati et al. used a micromechanical model

originally intended for long-fiber composites, approximating the brick shape as elliptic cylinders within a mortar matrix. This shape approximation, combined with Eshelby's solution and the Mori-Tanaka extension, was used to model the strain and stress within an inhomogeneous, two-phase system (brick and mortar). Differences in shape approximations or boundary conditions could lead to discrepancies, especially in the shear modulus (G), which is sensitive to stress distribution and interface assumptions.

- **Shape and Orientation Effects:** Bati et al.'s model assumes bricks as elliptic cylinders to apply Eshelby's tensor solutions, which work for ellipsoidal inclusions of specific orientations and aspect ratios. Any difference in shape representation, such as modelling bricks as rectangular elements, could introduce differences.

- **Experimental Variability:** Bati et al. validated their model using uniaxial compression tests on small masonry panels with lime and cement mortars. Inherent heterogeneity in masonry and potential variances in boundary conditions during testing could lead to slight deviations between model predictions and experimental results. Differences in testing methods, scale, or material quality could also affect values for properties like E_1 and G.

- **Phase Volume Ratios and Material Properties:** Bati et al. calculated macroscopic elastic constants based on the mechanical properties of bricks and mortar as well as phase volume ratios.

- **Micromechanical Model Approach:** Bati et al. employed Eshelby's solution and Mori-Tanaka theory to account for high inclusion concentrations typical of masonry.

In summary, the discrepancies between our results and those in [6] likely arise from variations in shape approximations, micromechanical modelling approaches, and testing methods.

4.5 Case 2: Influence of Mortar Properties on Masonry Homogenization

This case study investigates the role of mortar thickness and elasticity modulus on the homogenized properties of masonry, as analysed in [5]. The primary goal is to evaluate how variations in these parameters influence the elastic behaviour of the masonry structure. The brick properties, dimensions, and mortar Poisson's ratio used in this study are summarized in Table 4.4.

4.5.1 Variation in Mortar Thickness and Elasticity Modulus

To explore the impact of mortar thickness, five alternative RVE configurations were created by varying the mortar thickness from 5 mm to 25 mm, as illustrated in Fig. 4.4. Additionally, the elasticity modulus of the mortar (E_m) was varied between 1000 MPa and 10,000 MPa, generating a range of brick-to-mortar elasticity ratios, E_b/E_m, as follows: 11, 4.4, 2.2, 1.47, and 1.1. This parametric setup enabled the analysis of a comprehensive range of material configurations.

For each RVE configuration, the homogenized elasticity modulus (E_1) was calculated under a unit displacement gradient vector, $\mathbf{g} = \langle 1, 0, 0 \rangle^{\mathrm{T}}$. The results, compared with those reported in [5], are presented in Fig. 4.5.

Table 4.4: Material Properties and Dimensions of the RVE

Elasticity Modulus of Brick (E_b)	11,000	MPa
Poisson's Ratio of Brick	0.25	
Poisson's Ratio of Mortar	0.20	
Brick Height	75	mm
Brick Width	225	mm

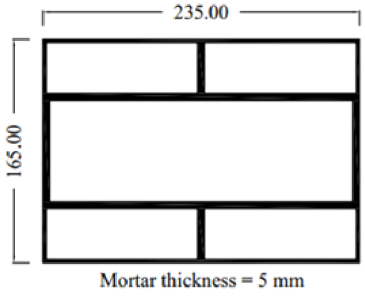

(a) RVE 1: Mortar thickness 5 mm.

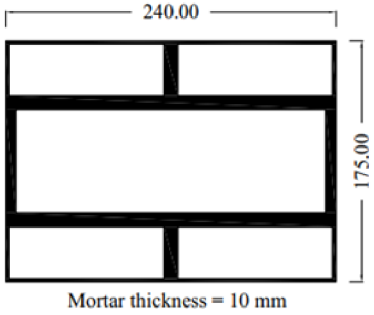

(b) RVE 2: Mortar thickness 10 mm.

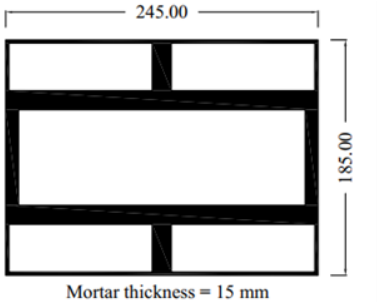

(c) RVE 3: Mortar thickness 15 mm.

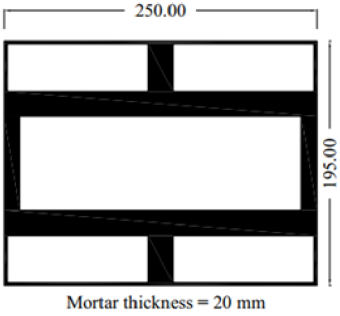

(d) RVE 4: Mortar thickness 20 mm.

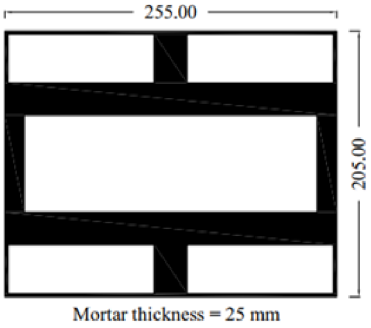

(e) RVE 5: Mortar thickness 25 mm.

Figure 4.4: Dimensions of the RVE Models with varying mortar thickness.

4.5.2 Results and Observations

The results in Fig. 4.5 indicate that the homogenized elasticity modulus (E_1) shows stronger agreement with the reference study [5] for configurations where $E_b/E_m = 1.1$ and the mortar thickness is minimized (5 mm). In contrast, cases with higher elasticity ratios ($E_b/E_m = 11$) and larger mortar thickness (25 mm) exhibit greater deviation. Despite these variations, the overall agreement between the X-FEM framework and the reference results is excellent, validating the proposed methodology's robustness.

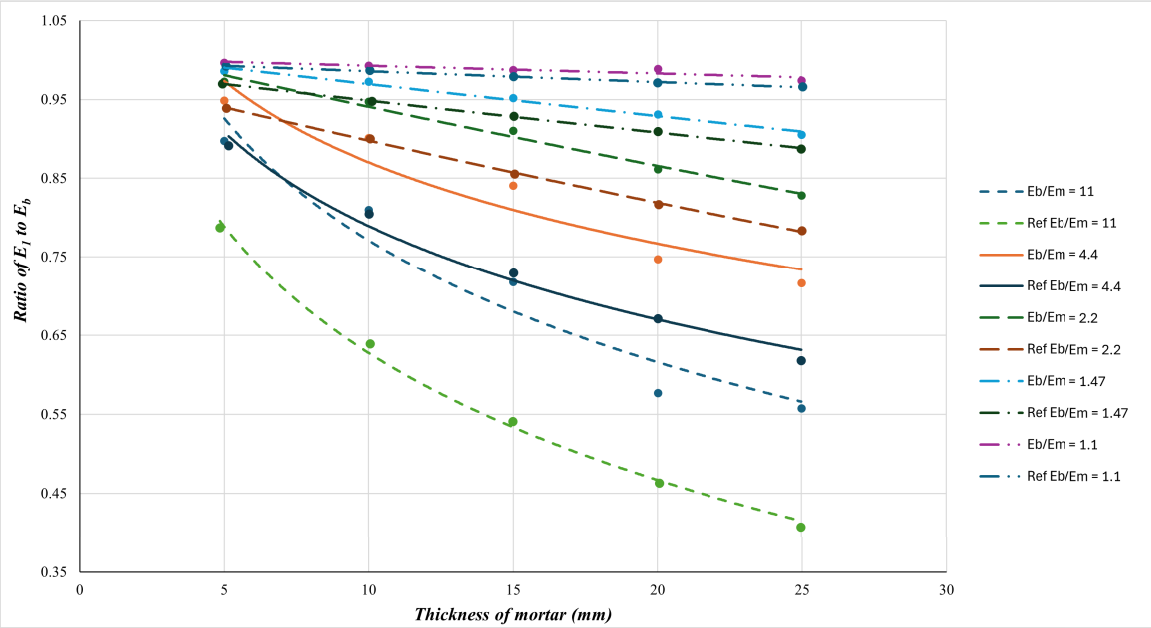

Figure 4.5: Ratio of Homogenized Modulus to Brick Modulus vs. Mortar Properties.

4.5.3 Parametric Study on Interface Stiffness

To further investigate the influence of interface stiffness on the homogenized elasticity modulus (E_1), parametric studies were conducted for the configuration where $E_b/E_m = 11$. Three mortar thickness values were considered, and the interface stiffness coefficient (k) was varied. Figure 4.6 illustrates that at lower interface stiffness values, the homogenized properties are significantly reduced due to imperfect bonding between the mortar and bricks. As k increases, the homogenized modulus stabilizes, reaching a plateau beyond which further increases in stiffness have negligible influence.

This stabilization behaviour highlights the framework's capacity to effectively capture bonding effects and provides practical insights into optimizing interface properties in masonry materials.

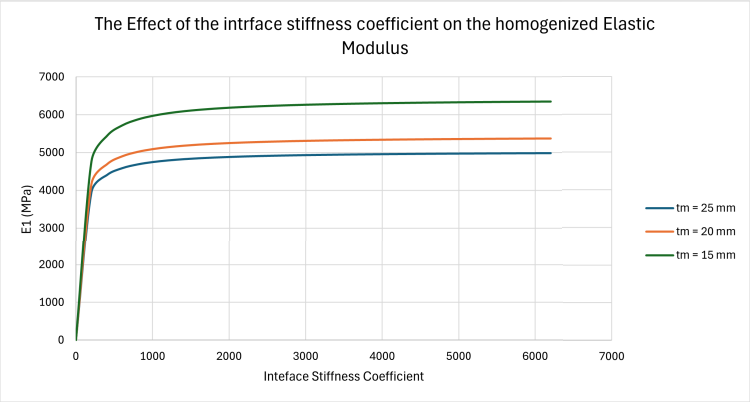

Figure 4.6: Average elasticity modulus E_1 vs. interface stiffness coefficient k.

4.6 Case 3: Evaluating the Influence of Boundary Conditions

In this case study, we explore the impact of different RVE boundary conditions on the homogenized elastic properties of masonry. Our objective is to validate the developed X-FEM-based computational homogenization technique by comparing our results with those reported by Luciano et al. in [10].

4.6.1 Model Configuration and Parameters

To ensure a meaningful comparison, we constructed an RVE that mirrors the one used in Luciano's study. The RVE consists of mortar serving as the matrix material and bricks as inclusions. The detailed properties and dimensions of the materials are provided in Table 4.5. The RVE dimensions are illustrated in Figure 4.7, and a regular finite element mesh of 49×37 elements was utilized for the analysis.

Table 4.5: Properties and Dimensions of the RVE Model

Macro Width X	245	mm
Macro Width Y	185	mm
Brick Width	225	mm
Brick Height	75	mm
Mortar Thickness	15	mm
E_{Brick}	15000	MPa
ν_{Brick}	0.25	
E_{Mortar}	1000	MPa
ν_{Mortar}	0.3	

Figure 4.7: RVE Dimensions and Mesh

To enhance the accuracy of our homogenization process, we applied the area of interest method, incorporating a 2.5 mm offset to define the region of interest within the RVE. The homogenized elasticity modulus was calculated under the displacement gradient $\mathbf{g} = \langle 1, 0, 0 \rangle^{\mathrm{T}}$.

4.6.2 Results and Comparative Analysis

The computed homogenized elasticity moduli for different boundary conditions are presented in Table 4.6. Our results show very good agreement with those obtained by Luciano et al., particularly under displacement and periodic boundary conditions.

Table 4.6: Homogenized Elasticity Moduli for Alternative RVE Boundary Conditions

Boundary Condition	Elasticity Modulus E_1 (MPa)	
	X-FEM Model	Reference [10]
Periodic Boundary Conditions	10032.53	8942
Displacement Boundary Conditions	10261.04	10029
Traction Boundary Conditions	9863.43	-

Our findings corroborate the observations made in the literature, notably by Hashin [56], that displacement and traction boundary conditions provide upper and lower bounds, respectively, for solutions based on periodic boundary conditions. The X-FEM-based results presented in Table 4.6 align with this theory, reinforcing the validity of our computational approach.

4.6.3 Investigating the Influence of Interface Damage

To further assess the robustness of our model, we explored the effect of interface damage between the mortar and the bricks on the overall stiffness of the masonry. By systematically varying

the location and extent of interface damage, we aimed to understand how such imperfections influence the homogenized elastic properties.

We introduced interface damage using two alternative approaches:

(A) **Cracks Through the Elements (CTE)**

In this approach, damage is represented as lines of discontinuity within the mortar beds. To model open cracks, we utilized the XFEM by assigning an interface stiffness $k = 0$ in Eq. (63) specifically at the damage locations. Figure 4.8 shows the crack patterns introduced, drawn as red lines within the mesh.

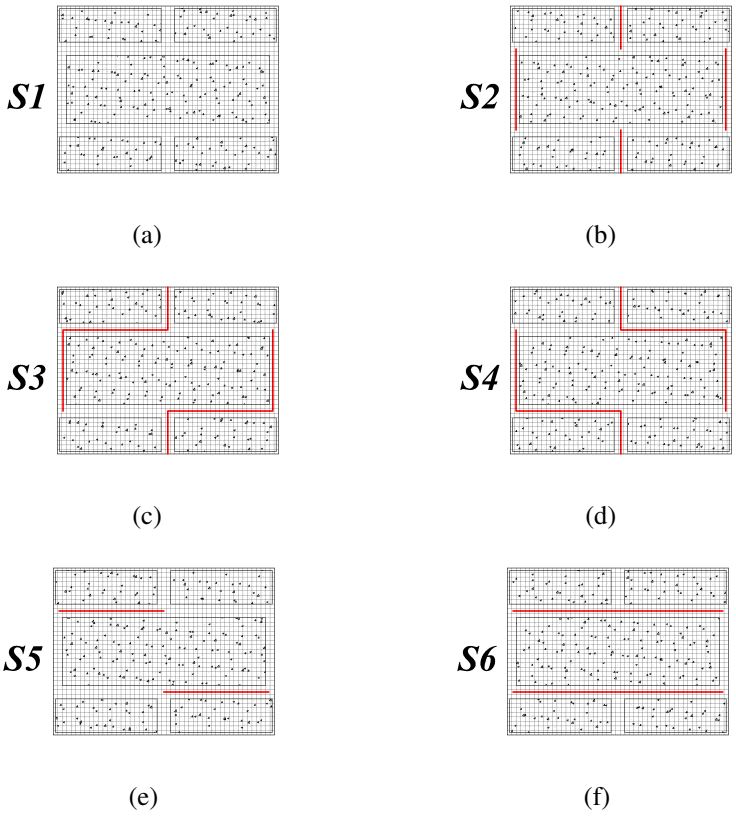

(g) (h)

Figure 4.8: Crack Patterns Introduced Using the XFEM Method

For each damage case depicted in Figure 4.8, we obtained the deformed shapes of the RVE under the deformation gradient $\mathbf{g} = \langle 1, 0, 0 \rangle^{\mathrm{T}}$, as shown in Figure 4.9.

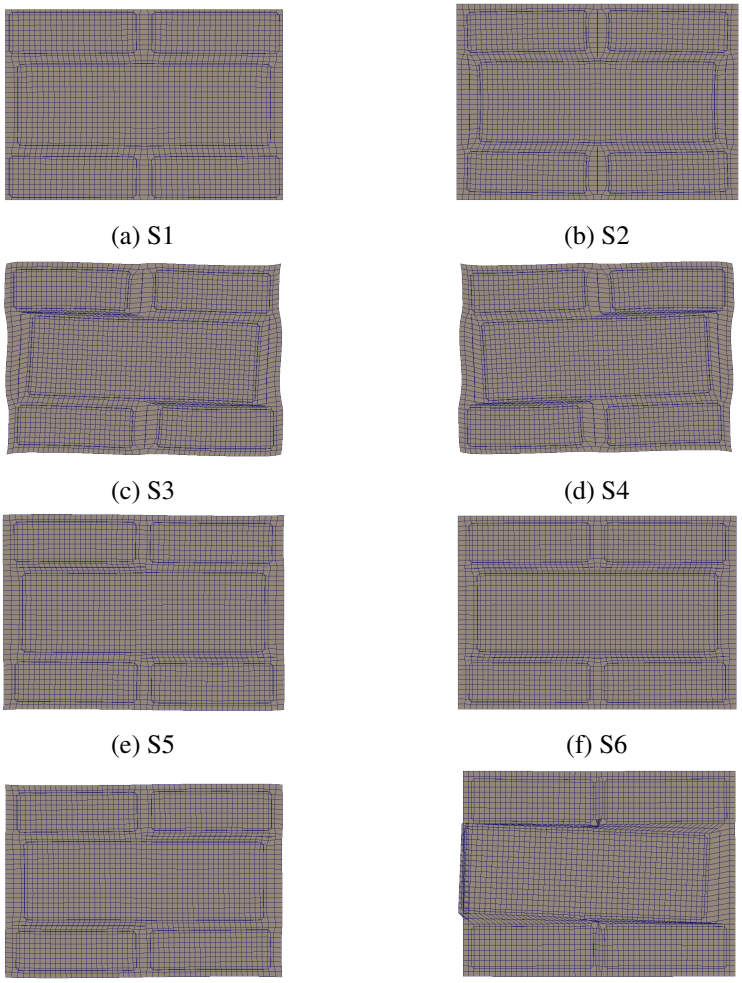

(a) S1 (b) S2

(c) S3 (d) S4

(e) S5 (f) S6

(g) S7 (h) S8

Figure 4.9: Deformed Shapes of the RVE Using the CTE Method

(B) **Zero Stiffness Elements (ZSE)**

In the ZSE approach, damage is introduced by assigning zero stiffness to mortar elements along the damage path. The zero stiffness elements are highlighted in red in Figure 4.10.

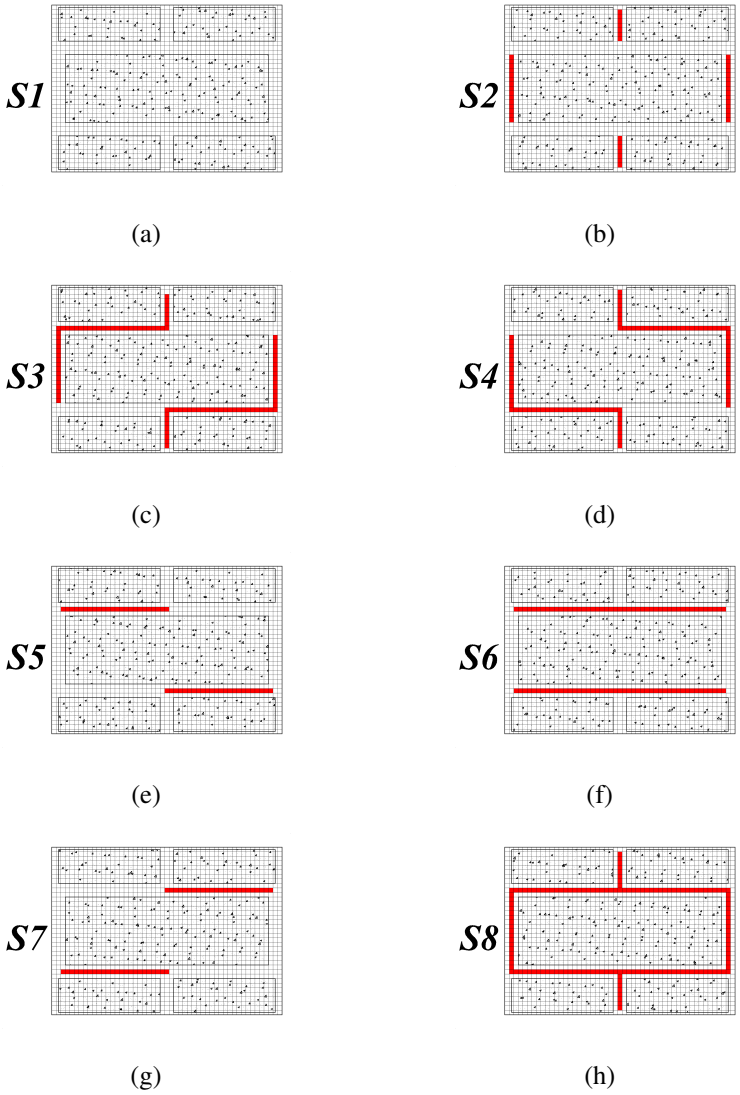

Figure 4.10: Damage Patterns for Masonry RVEs Using Zero Stiffness Elements

Similar to the CTE method, we obtained the deformed shapes under the same deformation gradient, presented in Figure 4.11.

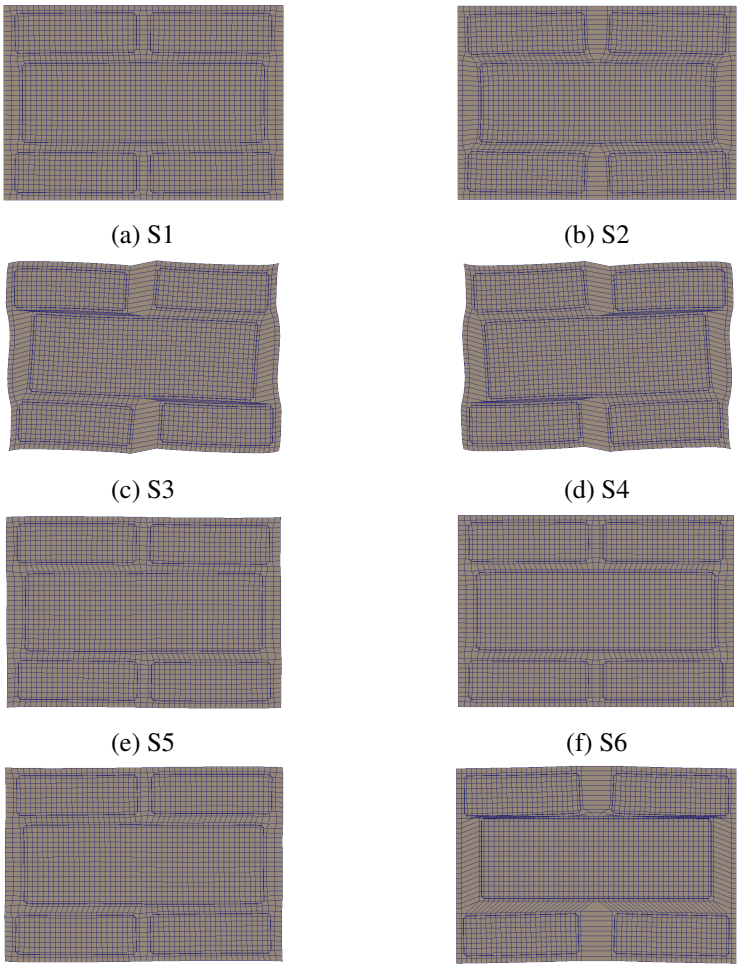

(a) S1 (b) S2

(c) S3 (d) S4

(e) S5 (f) S6

(g) S7 (h) S8

Figure 4.11: Deformed Shapes of the RVE Using the ZSE Method

4.6.4 Comparative Results and Discussion

Table 4.8 presents the elasticity moduli corresponding to different damage scenarios for both CTE and ZSE methods, alongside the reference results from Luciano et al. The comparison indicates that our model accurately captures the influence of interface damage on the homogenized moduli.

By comparing our results with the reference data, it becomes evident that both damage modelling techniques effectively simulate the reduction in stiffness due to interface damage. The slight discrepancies can be attributed to differences in modelling nuances and numerical implementations.

Table 4.7: Elasticity Moduli Corresponding to Different Damage Scenarios

Elasticity Moduli		S1	S2	S3	S4	S5	S6	S7	S8
E_1 (MPa)	Reference [10]	8942.00	2761.00	1203.00	1203.00	8398.00	7967.00	8398.00	0.00
	CTE	10032.53	2907.69	1486.45	1486.45	7721.54	7578.45	7721.54	2392.48
	ZSE	10032.53	2495.81	1341.90	1341.90	7629.76	7418.38	7629.76	0.00
E_2 (MPa)	Reference [10]	5595.00	5329.00	381.00	381.00	1343.00	0.00	1343.00	0.00
	CTE	5881.90	5230.46	216.09	216.09	1155.35	17.77	1155.35	-1257.37
	ZSE	5881.90	5136.12	-18.13	-18.13	1079.98	-14.10	1079.98	28.11

This comprehensive analysis demonstrates that the developed X-FEM-based computational homogenization technique is capable of accurately predicting the influence of boundary conditions and interface damage on the homogenized elastic properties of masonry. The close agreement with established results not only validates our approach but also underscores its potential applicability in the analysis and design of masonry structures subject to various damage scenarios.

4.7 Case 4: Validation of the Interface Cohesive Zone Model

To evaluate the performance of the Cohesive Zone Model (CZM) within the developed X-FEM-based framework, a validation study is conducted using the methodology outlined in Section 3.8. The results are compared against the extension and shear tests presented in [21], which characterize interface failure mechanisms. Model parameters are calibrated to align with those in [21], where a cohesive element was placed between two standard membrane finite elements, each measuring 10×10 mm. In contrast, the X-FEM model employs a single bulk element with a width of 20 mm and a height of 10 mm, incorporating a vertical cohesive interface at the mid-span. The left boundary is fully constrained, while the right boundary remains free to displace in both horizontal and vertical directions. The material properties assigned to the cohesive zone are summarized in Table 4.8. To minimize bulk deformations relative to interface separation, a high modulus of elasticity, $E = 1 \times 10^{10}$ MPa, is used for the bulk material.

4.7.1 Tension Test

A uniform tensile load is incrementally applied at the right boundary through two equal nodal forces, as illustrated in Fig. 4.12. The displacement at the tip increases up to $u = 0.2$ mm, ensuring that bulk deformations remain minimal relative to interface separation. Due to the high cohesive

Table 4.8: Material Properties for the Cohesive Zone Model

Property	Value	Unit
Tangential Stiffness	20.0	GPa
Normal Stiffness	20.0	GPa
Shear Strength	2.4	MPa
Tensile Strength	2.4	MPa
Softening Modulus	0.01	MPa

stiffness, the stress-displacement curve initially exhibits a steep elastic response until the damage threshold is reached. Elastic deformations are negligible compared to the overall separation.

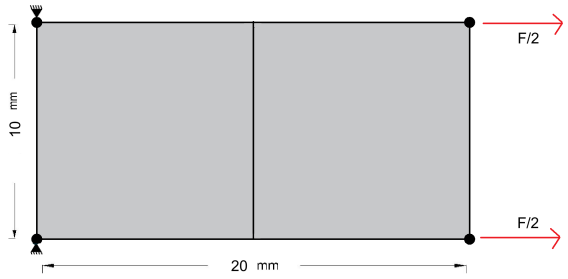

Figure 4.12: Extension test on a single element with an interface.

The stress-displacement response obtained from the X-FEM model is compared with the results from [21] in Fig. 4.13, demonstrating agreement in capturing interface failure characteristics. The results indicate that as the elastic cohesive stiffness is relatively high, the normal stress-displacement curve exhibits an initially steep elastic response until the damage threshold is reached, after which the interface begins to degrade.

4.7.2 Shear Test

The shear test follows the same material and geometric setup, with the applied load direction shifted to vertical (Fig. 4.14). The right boundary undergoes a displacement of $u = 0.2$ mm, with negligible end rotations, indicating that bulk deformations are minimal and vertical slip occurs primarily due to cohesive interface separation. The resulting stress-displacement behaviour, shown in Fig. 4.15, highlights the nonlinear degradation of stress transfer, attributed to the softening response of the cohesive zone. This behaviour aligns with the results of [21], where similar nonlinear characteristics were observed.

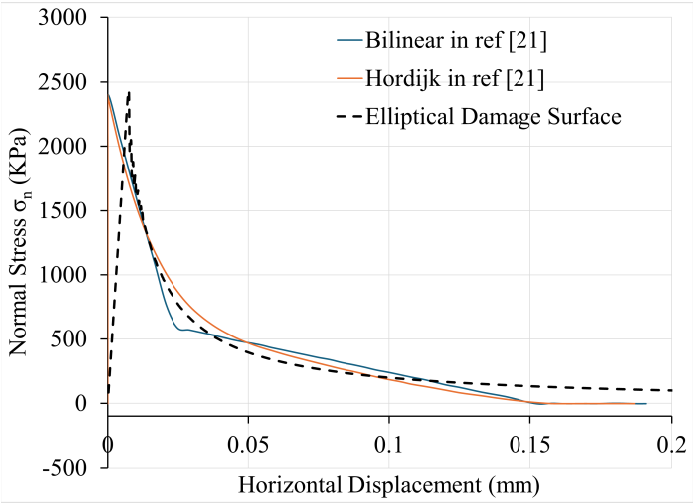

Figure 4.13: Comparison of stress-displacement curves for the extension test [21].

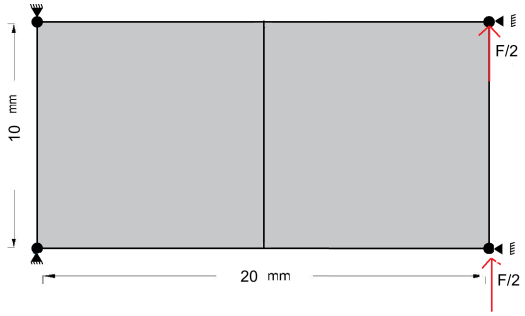

Figure 4.14: Shear test on a single element with an interface.

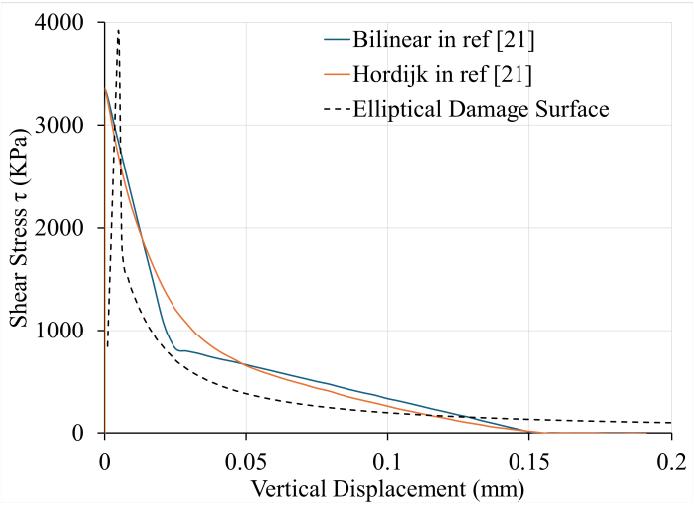

Figure 4.15: Comparison of stress-displacement curves for the shear test [21].

4.8 Case 5: Nonlinear Masonry Wall Analysis and Validation Against [9]

To fully leverage the capabilities of the proposed modelling framework, we employ an advanced approach to predict the structural behaviour of masonry walls by integrating a refined RVE-based homogenization scheme. This methodology captures the intricate geometrical and mechanical characteristics of masonry constituents, enabling the derivation of macro-scale stress-strain responses. The developed computational scheme ensures efficient computation by utilizing an RVE significantly smaller than the full-scale masonry wall. The obtained homogenized stress-strain curves are subsequently approximated using bilinear fits for tensile, compressive, and shear load conditions. These material models are then incorporated into structural-level simulations, facilitating the analysis of the masonry shear wall configuration illustrated in Fig. 4.16.

The structural wall is subjected to combined axial and lateral loading. A uniformly distributed pre-stress of $q = 68kN/m$ is applied to introduce a constant compressive load, while lateral forces are incrementally increased. The wall, modelled as a cantilever, has a thickness of 35 mm, a width of 298 mm, and a height of 238 mm. Finite element discretization is carried out using four-node quadrilateral membrane elements with a 25 $\times$ 25 mesh resolution. The mortar joints are modelled with a thickness of 10 mm, while the relevant material parameters for bricks, mortar, and their interface properties are summarized in Table 4.9. The adopted RVE dimensions are set at 155 mm $\times$ 35 mm, ensuring an accurate representation of masonry heterogeneity within a localized domain.

The cohesive zone properties assigned to the model are based on the parameter set provided in Table 4.9, replacing the values previously used in Table 4.8 to specifically account for the brick-mortar interface characteristics. Under compressive loading, the material is assumed to remain elastic, maintaining the initial stiffness observed in tension. The RVE analysis is conducted under the three alternative boundary conditions discussed in Section 3.7, with the bilinear approximation of the stress-strain response presented in Fig. 4.17. Homogenized material behaviour is subsequently validated using a single-element representation, as depicted in Fig. 4.18. The material parameters governing the bilinear constitutive model utilized in the structural-level analysis are documented in Table 4.10.

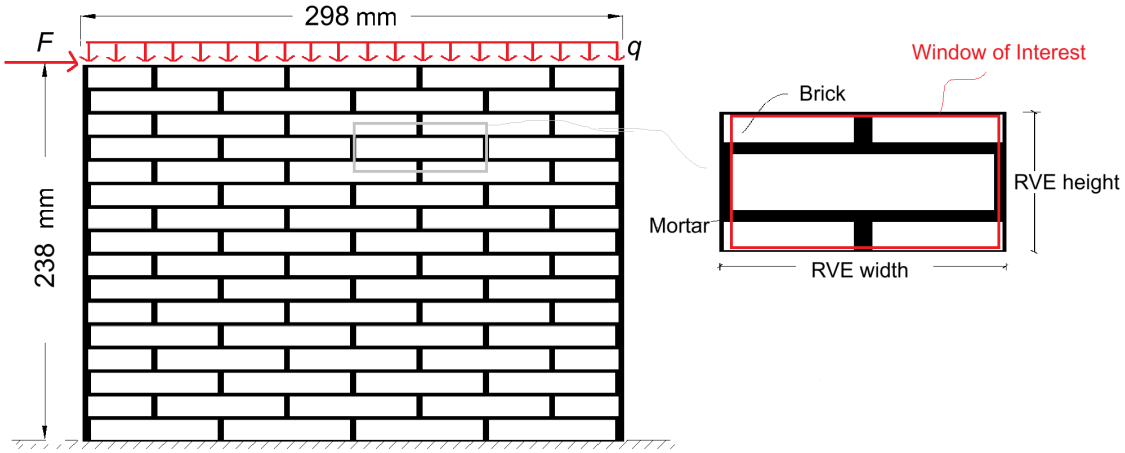

Figure 4.16: Geometric configuration, loading conditions, and selected RVE for the masonry shear wall analysis

Table 4.9: Material properties of bricks, mortar, and brick-mortar interfaces

Component	Parameter	Value	Units
Brick	Length	72.5	mm
	Height	12.5	mm
	Width	35.0	mm
	Elasticity modulus	4080	MPa
	Poisson's ratio	0.15	–
Mortar	Head joint thickness	2.5	mm
	Bed joint thickness	2.5	mm
	Elasticity modulus	3500	MPa
	Poisson's ratio	0.20	–
Brick-Mortar Interface	Tangential stiffness	20.0	GPa
	Normal stiffness	20.0	GPa
	Shear strength	0.25	MPa
	Tensile strength	0.18	MPa
	Softening Modulus	0.1	MPa

The bilinear model is parametrized based on the effective stress measure defined as $\sigma_{eff} = \sqrt{(\sigma_x^2 + \sigma_y^2 + \tau^2)}$. During structural-level simulations, the updated plane-stress elasticity matrix $\widehat{\mathbf{D}}_{up}$ is employed to compute stress increments as $\Delta\widehat{\boldsymbol{\sigma}} = \widehat{\mathbf{D}}_{up}\Delta\widehat{\epsilon}$, where:

$$\widehat{\mathbf{D}}_{up} = \frac{\widehat{E}_{up}}{1-\widehat{\nu}_{up}^2}\begin{bmatrix} 1 & \widehat{\nu}_{up} & 0 \\ \widehat{\nu}_{up} & 1 & 0 \\ 0 & 0 & \frac{1-\widehat{\nu}_{up}}{2} \end{bmatrix}. \tag{179}$$

Here, $\widehat{E}_{up}$ and $\widehat{\nu}_{up}$ are adaptively selected from Table 4.10, corresponding to the prevailing stress state. Unbalanced forces arising from stiffness changes are iteratively corrected. Further details on

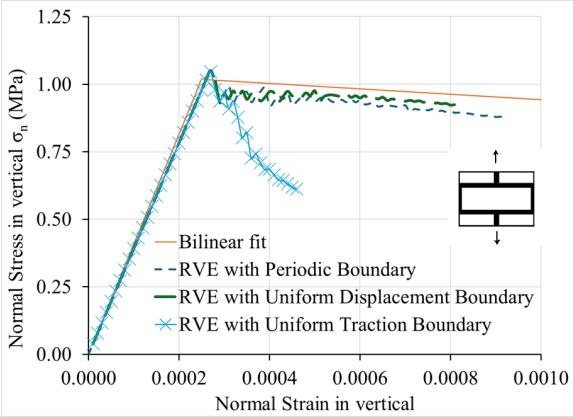

(a) Tensile response from RVE simulation

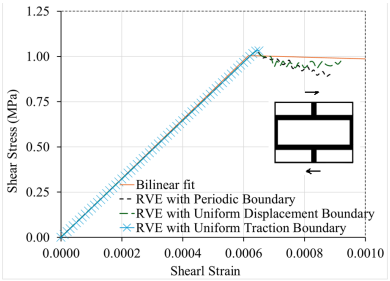

(b) Shear response from RVE simulation

Figure 4.17: Bilinear curve fits to homogenized RVE stress-strain data

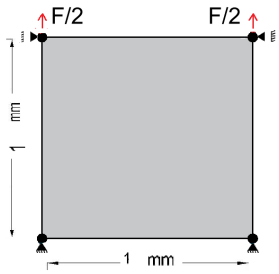

(a) Tensile test

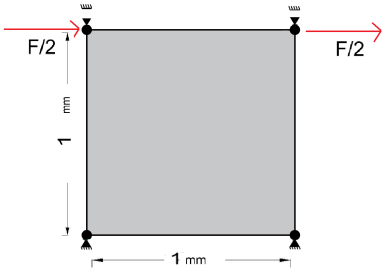

(b) Shear test

Figure 4.18: Single element verification using homogenized bilinear material properties

incremental solution techniques can be found in classical finite element references such as [54]. The structural-level force-displacement responses, shown in Fig. 4.19, closely follow experimental observations.

The numerical results show good agreement with [9], although exhibiting a slightly reduced load-bearing capacity due to premature crack localization and reduced ductility.

Table 4.10: Bilinear Material Model Parameters

Parameter	Value	Unit
Initial Elasticity Modulus (Compression)	3912.83	MPa
Second Elasticity Modulus (Compression)	3912.83	MPa
Third Elasticity Modulus (Compression)	3912.83	MPa
Initial Poisson Ratio (Compression)	0.20	-
Second Poisson Ratio (Compression)	0.10	-
Third Poisson Ratio (Compression)	0.05	-
First Threshold Effective Stress (Compression)	-8.00	MPa
Second Threshold Effective Stress (Compression)	-25.00	MPa
Initial Elasticity Modulus (Tension)	3912.83	MPa
Second Elasticity Modulus (Tension)	10.00	MPa
Third Elasticity Modulus (Tension)	5.00	MPa
Initial Poisson Ratio (Tension)	0.20	-
Second Poisson Ratio (Tension)	0.10	-
Third Poisson Ratio (Tension)	0.05	-
First Threshold Effective Stress (Tension)	1.00	MPa
Second Threshold Effective Stress (Tension)	0.70	MPa

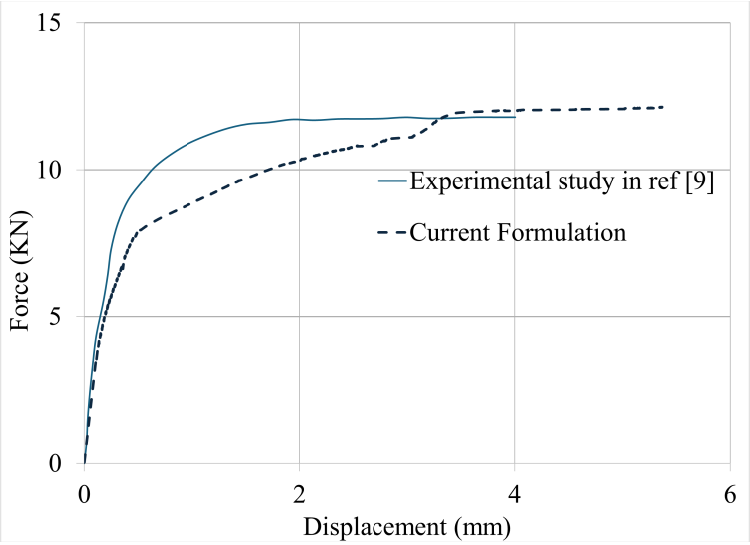

Figure 4.19: Load-deflection curve

Chapter 5

Conclusion

This thesis has presented a comprehensive investigation into the application of an X-FEM-based computational homogenization framework for masonry materials. The research was motivated by the need for an accurate and computationally efficient method to capture the macroscopic behavior of heterogeneous masonry structures. Through detailed methodological development and validation against established literature, the proposed framework demonstrated its capability in accurately predicting the effective elastic properties of masonry.

5.1 Summary of Contributions

The main contributions of this work are summarized as follows:

1. **Development of an X-FEM-based Computational Homogenization Framework:** A robust methodology was formulated to compute the effective elastic properties of masonry materials. The framework incorporated advanced numerical techniques to handle discontinuities at the interfaces between bricks and mortar while ensuring computational efficiency.

2. **Comprehensive Validation Studies:** The developed approach was validated against results from established studies, including [6], [5], and [10]. These comparisons confirmed the accuracy of the proposed methodology in capturing elastic constants such as E_1, E_2, ν_1, ν_2, and G, under varying boundary conditions. Furthermore, additional validation was conducted using

a Cohesive Zone Model (CZM) in Case 4, which demonstrated the accuracy of the framework in modeling interface failure mechanisms. The nonlinear response of masonry walls was also investigated in Case 5, where the homogenized stress-strain relations were validated against results from [9].

3. **Parametric Studies on RVE Characteristics:** The influence of RVE size, mortar thickness, and interface stiffness on the homogenized properties was systematically analyzed. These studies provided critical insights into the role of microstructural parameters in determining the effective mechanical behavior of masonry.

4. **Evaluation of Damage Scenarios:** Interface damage was modeled using the Cracks Through the Elements (CTE) and Zero Stiffness Elements (ZSE) approaches. The results demonstrated the framework's ability to accurately capture the impact of interface imperfections on the homogenized elastic properties. Additional studies on cohesive interfaces in Case 4 further validated the traction-separation behavior of the masonry joints, reinforcing the framework's predictive capabilities for interface failure.

5. **Nonlinear Structural Analysis:** The framework was extended to predict the nonlinear response of masonry walls in Case 5 by integrating homogenized stress-strain relations into macro-scale finite element simulations. The force-displacement curves obtained from the structural simulations exhibited close agreement with reference results, validating the accuracy of the proposed homogenization approach for large-scale masonry structures.

5.2 Key Findings

The key findings of this research are:

- **Periodic Boundary Conditions:** Among the boundary conditions studied, periodic boundary conditions were shown to provide the most representative average response for homogenization, aligning closely with the periodicity of the masonry microstructure.

- **Impact of RVE Size:** Larger RVEs captured more heterogeneities, leading to a slight reduction in homogenized stiffness values. This finding highlights the trade-off between computational efficiency and representativeness in RVE selection.

- **Interface Stiffness and Damage:** The parametric studies on interface stiffness revealed a stabilization of homogenized properties beyond a certain stiffness threshold. Moreover, the damage analysis confirmed the sensitivity of the homogenized properties to interface imperfections, emphasizing the importance of accurately modeling such effects in masonry structures. The cohesive zone validation in Case 4 provided further confirmation of the framework's ability to capture interface failure under both normal and shear loading conditions.

- **Nonlinear Behavior of Masonry:** The inclusion of nonlinear masonry wall simulations in Case 5 demonstrated that the homogenized constitutive model successfully predicted the structural response of masonry under combined axial and lateral loads. The observed force-displacement curves closely matched those from [9], affirming the validity of the multiscale modeling approach.

- **Comparison with Literature:** The proposed framework showed excellent agreement with established models and experimental data, validating its robustness and accuracy for masonry homogenization.

5.3 Concluding Remarks

This thesis has demonstrated the potential of the X-FEM-based computational homogenization framework as a powerful tool for analyzing masonry materials. By bridging the gap between microstructural details and macroscopic behavior, the proposed methodology offers a promising avenue for the design and analysis of masonry structures. The findings and insights gained from this research provide a solid foundation for future studies aimed at advancing the understanding and modeling of heterogeneous materials.

Bibliography

[1] C. Calderini, S. Cattari, and S. Lagomarsino, "In-plane strength of unreinforced masonry piers," *Earthquake engineering & structural dynamics*, vol. 38, no. 2, pp. 243–267, 2009.

[2] K. Beyer, "Peak and residual strengths of brick masonry spandrels," *Engineering Structures*, vol. 41, pp. 533–547, 2012.

[3] F Messali and J. Rots, "In-plane drift capacity at near collapse of rocking unreinforced calcium silicate and clay masonry piers," *Engineering Structures*, vol. 164, pp. 183–194, 2018.

[4] O. Elmeligy, N. Aly, and K. Galal, "Sensitivity analysis of the numerical simulations of partially grouted reinforced masonry shear walls," *Engineering Structures*, vol. 245, p. 112 876, 2021.

[5] G. Pande, J. Liang, and J Middleton, "Equivalent elastic moduli for brick masonry," *Computers and Geotechnics*, vol. 8, no. 3, pp. 243–265, 1989.

[6] S. B. Bati, G. Ranocchiai, G Ranocchiai, and L Rovero, "A micromechanical model for linear homogenization of brick masonry," *Materials and Structures*, vol. 32, pp. 22–30, 1999.

[7] A. Anthoine, "Derivation of the in-plane elastic characteristics of masonry through homogenization theory," *International journal of solids and structures*, vol. 32, no. 2, pp. 137–163, 1995.

[8] S Pietruszczak and X Niu, "A mathematical description of macroscopic behaviour of brick masonry," *International journal of solids and structures*, vol. 29, no. 5, pp. 531–546, 1992.

[9] A. Drougkas, V. Sarhosis, A. D'Alessandro, and F. Ubertini, "Homogenisation of masonry structures subjected to seismic loads through matrix/inclusion micromechanics," in *Structures*, Elsevier, vol. 38, 2022, pp. 375–384.

[10] R. Luciano and E. Sacco, "Homogenization technique and damage model for old masonry material," *International Journal of Solids and Structures*, vol. 34, no. 24, pp. 3191–3208, 1997.

[11] J. Guedes and N. Kikuchi, "Preprocessing and postprocessing for materials based on the homogenization method with adaptive finite element methods," *Computer methods in applied mechanics and engineering*, vol. 83, no. 2, pp. 143–198, 1990.

[12] J. Fish and A. Wagiman, "Multiscale finite element method for a periodic and nonperiodic heterogeneous medium," *ASME Applied Mechanics Division-publications-AMD*, vol. 157, pp. 95–95, 1993.

[13] J. M. Melenk and I. Babuška, "The partition of unity finite element method: Basic theory and applications," *Computer methods in applied mechanics and engineering*, vol. 139, no. 1-4, pp. 289–314, 1996.

[14] K. Park and G. H. Paulino, "Cohesive zone models: A critical review of traction-separation relationships across fracture surfaces," *Applied Mechanics Reviews*, vol. 64, no. 6, p. 060 802, 2011.

[15] C. K. Desai, S. Basu, and V. Parameswaran, "Determination of traction separation law for interfacial failure in adhesive joints at different loading rates," *The Journal of Adhesion*, vol. 92, no. 10, pp. 819–839, 2016.

[16] A. J. Levy and K. Hardikar, "The inclusion pair interaction problem with non-linear interface," *Journal of the Mechanics and Physics of Solids*, vol. 47, no. 7, pp. 1477–1508, 1999.

[17] S. K. Samanta and G. Bhattacharyya, "Modes of detachment at the inclusion–matrix interface," *Journal of Structural Geology*, vol. 25, no. 7, pp. 1107–1120, 2003.

[18] C. Wu, S. Gowrishankar, R. Huang, and K. M. Liechti, "On determining mixed-mode traction–separation relations for interfaces," *International Journal of Fracture*, vol. 202, pp. 1–19, 2016.

[19] E. Rahbar, A. Permanoon, and A. H. Akhaveissy, "Numerical evaluation of masonry-infill frames: Analysis of lateral strength and failure modes on meso scale," in *Structures*, Elsevier, vol. 52, 2023, pp. 779–793.

[20] X. Miao, D. Ling, A. Pan, and H. Wang, "A plastic-damage cohesive zone model for shear rupture band in geomaterials under mixed-mode and cyclic loading," *Computers and Geotechnics*, vol. 177, p. 106 829, 2025.

[21] R. Durand and F. H. B. T. da Silva, "A coulomb-based model to simulate concrete cracking using cohesive elements," *International Journal of Fracture*, vol. 220, no. 1, pp. 17–43, 2019.

[22] F. Töller, S. Löhnert, and P. Wriggers, "Bulk material models in cohesive zone elements for simulation of joining zones," *Finite Elements in Analysis and Design*, vol. 164, pp. 42–54, 2019.

[23] T. Belytschko and T. Black, "Elastic crack growth in finite elements with minimal remeshing," *International journal for numerical methods in engineering*, vol. 45, no. 5, pp. 601–620, 1999.

[24] N. Moës, J. Dolbow, and T. Belytschko, "A finite element method for crack growth without remeshing," *International journal for numerical methods in engineering*, vol. 46, no. 1, pp. 131–150, 1999.

[25] N. Sukumar, D. L. Chopp, N. Moës, and T. Belytschko, "Modeling holes and inclusions by level sets in the extended finite-element method," *Computer methods in applied mechanics and engineering*, vol. 190, no. 46-47, pp. 6183–6200, 2001.

[26] C. Miehe and A. Koch, "Computational micro-to-macro transitions of discretized microstructures undergoing small strains," *Archive of Applied Mechanics*, vol. 72, pp. 300–317, 2002.

[27] M Stroeven, H Askes, and L. Sluys, "Numerical determination of representative volumes for granular materials," *Computer methods in applied mechanics and engineering*, vol. 193, no. 30-32, pp. 3221–3238, 2004.

[28] V. Kouznetsova, W. Brekelmans, and F. Baaijens, "An approach to micro-macro modeling of heterogeneous materials," *Computational mechanics*, vol. 27, no. 1, pp. 37–48, 2001.

[29] G. R. Fernandes, M. J. M. Silva, J. F. Vieira, and J. J. Pituba, "A 2d rve formulation by the boundary element method considering phase debonding," *Engineering Analysis with Boundary Elements*, vol. 104, pp. 259–276, 2019.

[30] C. Zhou, K. Li, and X. Pang, "Effect of crack density and connectivity on the permeability of microcracked solids," *Mechanics of Materials*, vol. 43, no. 12, pp. 969–978, 2011.

[31] G. Zi and T. Belytschko, "New crack-tip elements for xfem and applications to cohesive cracks," *International Journal for Numerical Methods in Engineering*, vol. 57, no. 15, pp. 2221–2240, 2003.

[32] J.-H. Song, P. M. Areias, and T. Belytschko, "A method for dynamic crack and shear band propagation with phantom nodes," *International Journal for Numerical Methods in Engineering*, vol. 67, no. 6, pp. 868–893, 2006.

[33] P. Laborde, J. Pommier, Y. Renard, and M. Salaun, "High-order extended finite element method for cracked domains," *International journal for numerical methods in engineering*, vol. 64, no. 3, pp. 354–381, 2005.

[34] N. Moës, M. Cloirec, P. Cartraud, and J.-F. Remacle, "A computational approach to handle complex microstructure geometries," *Computer methods in applied mechanics and engineering*, vol. 192, no. 28-30, pp. 3163–3177, 2003.

[35] H. R. Lotfi and P. B. Shing, "Interface model applied to fracture of masonry structures," *Journal of structural engineering*, vol. 120, no. 1, pp. 63–80, 1994.

[36] G. Giambanco, S. Rizzo, and R. Spallino, "Numerical analysis of masonry structures via interface models," *Computer methods in applied mechanics and engineering*, vol. 190, no. 49-50, pp. 6493–6511, 2001.

[37] M. M. Attard, A. Nappi, and F. Tin-Loi, "Modeling fracture in masonry," *Journal of Structural Engineering*, vol. 133, no. 10, pp. 1385–1392, 2007.

[38] A. Stavridis and P. Shing, "Finite-element modeling of nonlinear behavior of masonry-infilled rc frames," *Journal of structural engineering*, vol. 136, no. 3, pp. 285–296, 2010.

[39] T. Zahra, A. Jelvehpour, J. A. Thamboo, and M. Dhanasekar, "Interfacial transition zone modelling for characterisation of masonry under biaxial stresses," *Construction and Building Materials*, vol. 249, p. 118 735, 2020.

[40] A. M. D'Altri, V. Sarhosis, G. Milani, *et al.*, "Modeling strategies for the computational analysis of unreinforced masonry structures: Review and classification," *Archives of computational methods in engineering*, vol. 27, pp. 1153–1185, 2020.

[41] F. Liu and R. I. Borja, "A contact algorithm for frictional crack propagation with the extended finite element method," *International Journal for Numerical methods in engineering*, vol. 76, no. 10, pp. 1489–1512, 2008.

[42] T.-P. Fries and M. Baydoun, "Crack propagation with the extended finite element method and a hybrid explicit–implicit crack description," *International Journal for numerical methods in engineering*, vol. 89, no. 12, pp. 1527–1558, 2012.

[43] J. Chessa, H. Wang, and T. Belytschko, "On the construction of blending elements for local partition of unity enriched finite elements," *International Journal for Numerical Methods in Engineering*, vol. 57, no. 7, pp. 1015–1038, 2003.

[44] T. Kanit, S. Forest, I. Galliet, V. Mounoury, and D. Jeulin, "Determination of the size of the representative volume element for random composites: Statistical and numerical approach," *International Journal of solids and structures*, vol. 40, no. 13-14, pp. 3647–3679, 2003.

[45] M. G. D. Geers, V. G. Kouznetsova, and W. A. M. Brekelmans, "Computational homogenization," in *Multiscale Modelling of Plasticity and Fracture by Means of Dislocation Mechanics*, R. Pippan and P. Gumbsch, Eds. Vienna: Springer Vienna, 2010, pp. 327–394, ISBN: 978-3-7091-0283-1. DOI: 10.1007/978-3-7091-0283-1_7. [Online]. Available: https://doi.org/10.1007/978-3-7091-0283-1_7.

[46] S. J. Hollister and N. Kikuchi, "A comparison of homogenization and standard mechanics analyses for periodic porous composites," *Computational mechanics*, vol. 10, no. 2, pp. 73–95, 1992.

[47] P. Wriggers and S. Moftah, "Mesoscale models for concrete: Homogenisation and damage behaviour," *Finite elements in analysis and design*, vol. 42, no. 7, pp. 623–636, 2006.

[48] F. Larsson, K. Runesson, S. Saroukhani, and R. Vafadari, "Computational homogenization based on a weak format of micro-periodicity for rve-problems," *Computer Methods in Applied Mechanics and Engineering*, vol. 200, no. 1-4, pp. 11–26, 2011.

[49] N Sukumar and J.-H. Prévost, "Modeling quasi-static crack growth with the extended finite element method part i: Computer implementation," *International journal of solids and structures*, vol. 40, no. 26, pp. 7513–7537, 2003.

[50] J. Réthoré, A. Gravouil, and A. Combescure, "A stable numerical scheme for the finite element simulation of dynamic crack propagation with remeshing," *Computer methods in applied mechanics and engineering*, vol. 193, no. 42-44, pp. 4493–4510, 2004.

[51] M. H. Holmes, *Introduction to perturbation methods*. Springer Science & Business Media, 2012, vol. 20.

[52] T. Belytschko, W. K. Liu, B. Moran, and K. Elkhodary, *Nonlinear finite elements for continua and structures*. John wiley & sons, 2014.

[53] F. Armero and S. Oller, "A general framework for continuum damage models. i. infinitesimal plastic damage models in stress space," *International Journal of Solids and Structures*, vol. 37, no. 48-50, pp. 7409–7436, 2000.

[54] A. Ibrahimbegovic, *Nonlinear solid mechanics: theoretical formulations and finite element solution methods*. Springer Science & Business Media, 2009, vol. 160.

[55] J Alfaiate, G. Wells, and L. Sluys, "On the use of embedded discontinuity elements with crack path continuity for mode-i and mixed-mode fracture," *Engineering fracture mechanics*, vol. 69, no. 6, pp. 661–686, 2002.

[56] Z. Hashin, “Extremum principles for elastic heterogenous media with imperfect interfaces and their application to bounding of effective moduli,” *Journal of the Mechanics and Physics of Solids*, vol. 40, no. 4, pp. 767–781, 1992.